Department of Physics and Astronomy

Convergent close-coupling approach to antiproton and proton collisions with atomic and molecular targets

Sanat Avazbaev

This thesis is presented for the Degree of
Doctor of Philosophy
of
Curtin University

September 2015

Declaration

To the best of my knowledge and belief this thesis contains no material previously published by any other person except where due acknowledgment has been made.

This thesis contains no material which has been accepted for the award of any other degree or diploma in any university.

Signature 

date 26/11/2015

Contents

Summary

This thesis is devoted to the development of a semi-classical convergent close-coupling (CCC) method to study antiproton and proton collisions with atomic and molecular targets. The thesis is structured as follows. Chapter 1 presents the motivation for the study of collisions of ions with atoms and molecules. Different theoretical methods that are widely applied to these collisions are reviewed. Particular attention is given to the recent developments. Semi-classical single-centre CCC formalism and its application to antiproton-hydrogen collisions are presented in Chapter 2. In Chapter 3 single-centre CCC approach is applied to antiproton ($\bar{p}$) collisions with multi-electron systems. The wave functions of the Ne, Ar, Kr and Xe atoms have been described using a model of six p-shell electrons above an inert Hartree-Fock core with only one-electron excitations from the outer p shell allowed. Single-ionisation cross sections for the Ne, Ar, Kr and Xe atoms are calculated. Chapter 4 outlines further generalisation of the method to collisions with molecular targets. A new approach which allows analytic averaging over all possible molecular orientations is developed. We describe two-centre extension of the semi-classical approach in Chapter 5. A new numerical technique to evaluate two-centre matrix elements is given in detail. In Chapter 6 we present the preliminary results of the application of the two-centre method to the p-H(1s) scattering. Finally in Chapter 7 we make conclusions arising from this work and indicate future directions.

Main results of this work

- Semi-classical CCC method has been developed to investigate antiproton collisions with multi-electron targets.
- Single-ionisation cross sections for the Ne, Ar, Kr and Xe atoms by antiproton impact have been calculated in a wide energy range. The results are in good agreement with experiments.
- The semi-classical CCC approach has been extended to treat antiproton collisions with molecular targets. The interaction matrix elements and time-dependent expansion coefficients are expressed in a way that eventually leads to analytic averaging over all molecular orientations.
- Based on the studies of the time evolution of the electron-cloud distribution during the antiproton collisions with atomic and molecular hydrogen, it is shown that the strong suppression of the single ionisation cross section at low energies is due to the structure of the molecular target.
- Cross sections for ionisation with excitation, double ionisation and proton production in antiproton-molecular hydrogen collisions have been calculated employing a sequential two-step approximation. Good agreement with experiment for proton production has been found above 40 keV.
- The semi-classical single-centre CCC method has been generalised to the two-centre case. A new numerical technique to evaluate two-centre matrix elements is described.
- Excitation and electron capture to lowest levels as well as the total capture cross sections are found to be in good agreement with available experiments and other theoretical calculations.

List of publications

Five peer-reviewed papers have been published during the thesis period. The thesis is based on papers labelled by A and B.

A) I. B. Abdurakhmanov, A. S. Kadyrov, D. V. Fursa, S. K. Avazbaev, J. J. Bailey, and I. Bray, Antiproton-impact ionization of Ne, Ar, Kr, Xe, and H_2O. Physical Review A **91**, 022712 (2015).

B) I. B. Abdurakhmanov, A. S. Kadyrov, D. V. Fursa, S. K. Avazbaev, and I. Bray, Close-coupling approach to antiproton-impact breakup of molecular hydrogen. Physical Review A **89**, 042706 (2014).

C) D. Delande, K. Sacha, M. Plodzien, S. K. Avazbaev, J. Zakrzewski, Many-body Anderson localization in one-dimensional systems. New Journal of Physics **15**, 045021 (2013).

D) K. Nakamura, Z.A. Sobirov, D.U. Matrasulov, and S.K. Avazbaev, Bernoulli's formula and Poisson's equations for a confined quantum gas: Effects due to a moving piston. Physical Review E **86**, 061128 (2012).

E) K. Nakamura, S. K. Avazbaev, Z. A. Sobirov, D. U. Matrasulov, and T. Monnai, Ideal quantum gas in an expanding cavity: Nature of nonadiabatic force. Physical Review E **83**, 041133 (2011).

Acknowledgments

It is my greatest pleasure to start the acknowledgments by thanking my supervisor Assoc. Prof. Alisher Kadyrov for his great scientific insight, permanent support and guidance. This thesis would have been impossible without his encouragement. Also I am grateful to my co-supervisors Prof. Igor Bray, Prof. Dmitry Fursa and Dr. Ilkhom Abdurakhmanov for their advices and useful discussions. In addition, I would like to thank Prof. Andris Stelbovics for his constructive advices during my work on this thesis. I am grateful to them for everything I have learnt throughout my PhD years.

The friendly atmosphere of the theoretical physics group at Curtin has made it an enjoyable place to work. My thanks goes to Ravshan, Andrey, Chris, Mark, Jeremy, Paul, Jackson and others for their help and friendship.

I acknowledge Curtin University and the Centre of Excellence for Antimatter-Matter Studies for the financial support. Also, I thank the administrative staff of the Applied Physics Department, especially Melat Habtemariam, for their assistance.

Last but not the least, my gratitude goes to my family. I thank Saodat, Kamola and Ulugbek for their motivation and compassion.

Chapter 1

Introduction

1.1 Why are collisions of antiprotons and protons with atoms and molecules important?

Understanding collisions of atoms and molecules with heavy charged particles is important from both pure fundamental and practical points of view. Upcoming accelerator facility FAIR (Facility for Antiproton and Ion Research) [1] along with the international collaborations FLAIR (Facility for Low-energy Antiproton and Ion Research) [2] will provide highly intense antiproton beams. This will enable atomic physicists to perform detailed study of ionisation processes with antiprotons in kinematically complete experiments. In particular, design of FLAIR requires the precise knowledge of the collision mechanism between antiproton and molecular hydrogen, since H_2 is expected to be one of the dominant residual-gas molecules. These experimental efforts complement ongoing investigations at CERN. ELENA (Extra Low Energy Antiproton), a small ring at CERN Antiproton Decelerator [3], is expected to substantially increase the number of trappable antiprotons. The first antiproton scattering experiments with ELENA are planned for 2017. In addition, understanding of antiproton interactions with atoms and molecules is important to the ALPHA Collaboration

at CERN that attempts to test the invariance with respect to charge conjugation, parity transformation, and time reversal (CPT invariance) by forming and trapping antihydrogen and studying the gravitational behaviour of antimatter [4].

One of the potential applications of the collisions involving charged particles is hadron therapy [5]. The advantage of hadron therapy over the X-ray radiation therapy lies in the unique physical and radiobiological properties of these particles; they can penetrate the tissues with little diffusion and deposit the maximum energy just before stopping. This allows a precise definition of the specific region to be irradiated. With the use of hadrons the tumour can be irradiated while the damage to healthy tissues is substantially reduced. Improvements in accelerator technology, along with advances in medical imaging and computing, have made proton therapy a viable option for routine medical applications. In the beginning of the 1990s the first proton facilities in clinical settings were established in the USA. As of April 1, 2015, 49 proton beam therapy facilities are fully functioning around the world, while 29 facilities are under construction [6]. As for carbon-ion therapy, there are eight operating centres and four under construction [6]. At the end of 2013, 105,000 patients had been treated with proton beams [7], and approximately 13,000 patients had received carbon-ion therapy [6].

As an alternative to protons and carbon ions, antiprotons can also be used to deliver radiation to the body in a controlled way and may have additional advantages [8, 9]. This is supported by the fact that antiprotons annihilate and produce a variety of low and high-energy particles. The low energy particles emit biologically effective high linear energy transfer radiation in the immediate vicinity of the annihilation point. That is why the study of the biological effectiveness of the antiproton stopping peak enhancement by the densely ionising

annihilation products is one of primary tasks of FLAIR at GSI [10] and ACE collaboration at CERN [11].

1.2 Overview of existing theoretical approaches to collisions of antiprotons and protons with atoms and molecules

Within the last two decades the theoretical description of collisions involving charged ions has advanced considerably. The design and construction of decent experimental facilities as well as the progress in computational technology have intensified this development.

All theoretical approaches used to investigate the collisions of ions with atoms and molecules may be classified into three categories. They are classical methods, first-order quantum-mechanical perturbation techniques and nonperturbative methods. The most successful treatments are nonperturbative methods which are based on the solution of the time-dependent Schrödinger equation (TDSE) within lattice based or close-coupling schemes. The TDSE is obtained from the exact stationary Schrödinger equation under semi-classical approximation [12, 13]. In this approximation, the nuclear motion is assumed to be along a straight-line trajectory. The validity of this assumption is justified at collision energies above 1 keV. In this section the most commonly used methods will be briefly reviewed.

1.2.1 Classical trajectory Monte-Carlo method

In the classical trajectory Monte-Carlo (CTMC) method both the nuclear and the electronic motions are treated classically. The method was introduced by Abrines and Percival [14] and Olson and Salop [15]. It consists of three steps:

(i) initialisation of the projectile-target configuration; (ii) calculation of the classical trajectories; and (iii) a final-state test for reaction. In the first step the impact parameter, the orientation and momentum of the active electron are randomly selected by the Monte-Carlo technique. In the second step the Hamiltonian equations of motion are numerically solved from some large initial projectile-target separation, through the collision, and continuing to some large final separation. After integration of the coupled equations, the relative energies between the particles are determined and the reactions taking place are established. The main advantage of this method is that it can describe dynamic effects occurring during the collision and give a fully kinematic picture of the scattering.

There exist a large number of works which treat the electronic motion classically, irrespective of the quantum nature and the value of the de Broglie wavelength. Schultz [16] reported single-ionisation and charge transfer cross sections in collisions of electrons, positrons, protons, and antiprotons with atomic hydrogen and helium in the velocity interval of 0.5-7.0 a.u. The study of the effects in the projectile mass and sign change can be performed due to the fact that the CTMC method treats all of the projectiles (e, $\bar{e}$, p and $\bar{p}$) within the same theoretical framework. It was shown that at high velocities the single-ionisation cross section for each of these singly charged particles becomes equal. However, the differences in the single-charge-transfer impact persist to very large velocities.

CTMC method has been applied to describe an interesting feature of ion-atom ionisation cross sections: the electron capture to the continuum (ECC) cusp observed in H^++He collision [17]. The cusp appears in the spectra of the emitted electrons in the forward direction when the velocity of the electron matches that of the projectile. By classical calculations Illescas, Pons and Riera [18] studied the character of the ECC electrons. Later, Shah *et al.* [19]

performed detailed measurements and calculations for electron velocity distributions emitted at 0° for collisions of H^+ incident ions on H_2 and He. Their calculations confirmed that the cusp is a peak and not a divergence smoothed by convolution over a small angle of acceptance in the experiment. Sarkadi *et al.* [20] have presented their measurements and CTMC calculations for collisions of 20 keV protons with He atoms. However, neither their experimental data nor their CTMC results support the findings of Shah *et al.* [19].

Recently Cariatore and Otranto [21] have developed many-electron-multicentre CTMC (mmCTMC) approach. The method is tested in the framework of charge-exchange processes between bare projectiles with charges $q = +3$ to $+10$ and CO molecules for which 8-active electrons are considered. They use three models to describe the target molecule: mmCTMC, single-centre and independent atoms models. The results of these three models used in their work have been compared to recent experimental data (on total charge-exchange cross sections, hardness ratios, and state-selective charge-exchange cross sections) from Jet Propulsion Laboratory. It is noted the mmCTMC results are in better agreement than those from one-electron models with the data in the whole q-range considered.

The most recent development in the CTMC method was performed by Cariatore, Otranto and Olson [22]. They introduce a CTMC methodology that provides a more accurate momentum and radial distributions representation for $H(1s)$ and $H^*(n = 2)$. In order to evaluate the proposed model and check its performance against the other theoretical approaches electron-capture reactions for C^{6+}, N^{7+} and O^{8+} projectiles have been investigated at impact energies in the range 10-150 keV/amu. For $H(1s)$ electron-capture results provided by the method are found to be in much better agreement with atomic-orbital-close-coupling calculations than other CTMC formulations.

1.2.2 Continuum distorted wave method

Continuum-distorted-wave-eikonal-initial-state (CDW-EIS) is one of the commonly used approximations for describing atomic ionisation by ion impact at medium and high energies [8, 23–25]. Interest in the method has been intensified due to the fully differential cross-sections (FDCS) obtained in cold-target recoil-ion momentum spectroscopy (COLTRIMS) experiments [26–28]. Being introduced by Crothers and McCann [23], the method accounts for the long-range nature of the Coulomb potential and includes the distortion of the target states in both the initial and final channels. It allows to calculate the scattering amplitudes in a closed analytic form and its extension to the multielectron targets is straightforward in the frozen core approximation. The approach has been reviewed by Fainstein *et al.* [29].

The original CDW-EIS approach [23] considers the projectile trajectory classically and does not include the projectile-ion interaction. Later, the method was refined to include the nucleus-nucleus (NN) interaction by Rodriguez *et al.* [30], Sanchez *et al.* [31], Voitkiv *et al.* [32–35] and Ciappina *et al.* [36]. The role of the NN interaction effects in ionisation dynamics by ion impact is of great interest. Although extensive experiments have not been conducted yet, various differential cross sections have been calculated by several groups [32–35, 37–39]. Voitkiv and Ullrich [32] studied the FDCS for ionisation of hydrogen atoms by antiproton and proton impact at intermediate to high-impact energies. By calculating the FDCS, it has been found that there exist substantial charge sign effects and these effects are pronounced in the FDCS. Later, Voitkiv *et al.* [33] considered the single ionisation of hydrogen and helium targets by bare ions in the perturbative regime. Their studies based on the first, second, Glauber as well as CDW-EIS approximations, revealed that the higher order ef-

fects can considerably influence the electron emission even in the collision plane. This is in contrast to the expectation that first order approximations in the projectile-target interactions should yield good results. Moreover, it was found that the deviations from the first-order results would become significant when the electron emission was analysed in the plane perpendicular to the momentum transfer.

Recently, Chowdhury *et al.* [40] extended the works of Madison *et al.* [41] to treat molecular targets calculating triply and double differential cross sections for single ionisation of H_2 by 75-keV proton impact. However, their results are about 4.5 times lower than experiment for all the measured ejected electron energies. Gulyás *et al.* [42] presented FDCS and double differential cross-sections (DDCS) for single ionisation of Li in collisions with H^+ and O^{8+} ions within the framework of the independent-electron model. In the case of the proton impact the authors have found that the inclusion of the NN interaction is not important. While in the case of O^{8+} ions this interaction is crucial. Also, their calculations reproduce the satellite peak structure observed in the FDCS for the Li($2s$) measurements [43].

Galassi *et al.* [44] reported doubly, singly and total ionisation cross sections for proton impacting on DNA (deoxyribonucleic acid) and RNA (ribonucleic acid) components based on the CDW-EIS approaches. It is necessary to state that extensive experimental data have not been reported for proton scattering on these biologically important targets. Comparison of the calculated cross sections with available experimental data shows an overall good agreement. However, there are large discrepancies between the theoretical and experimental double differential cross sections for uracil.

1.2.3 Lattice-based technique

A direct approach to the solution of the time-dependent Schrödinger equation is the discretization of the operators and the wave function on a (position or momentum) lattice. One of the strengths of the method is its straightforward applicability to many different types of problems in atomic physics. However, this technique is computationally demanding. That is why only substantial advances in computer technology have allowed the possibility of carrying out lattice-based calculations of reasonable convergence.

In [45, 46] the lattice TDSE (LTDSE) approach was applied to calculate excitation and ionisation cross-sections in collisions of antiprotons with atomic hydrogen and He^+. In their approach discretization is performed on a Cartesian lattice. The reflection effects of the evolving electronic wave functions from the boundaries of the lattice-box are eliminated by introducing imaginary potentials. The computed excitation (up to $3d$) and ionisation cross sections were found to be in good agreement with the available theoretical treatments.

Extending the method to p+H collisions, Kolakowska *et al.* [47] have computed excitation and charge transfer cross sections for up to $3d$ states from the ground state for collisions of protons with hydrogen using a staggered leapfrog propagator and a Fourier collocation method with a split-operator propagator for time evolution. Their results have been found to be in reasonable agreement with experimental data [48, 49] and other calculations, such as the two-centre atomic orbital close-coupling method of Kuang and Lin [50] and the continuum distorted-wave calculations of Belkić *et al.* [51]. Further developments of the approach by Schultz *et al.* [52] and Pindzola *et al.* [53] proved the power of the technique to treat ion-atom collisions.

Relatively recently, Pindzola and Schultz [54] have formulated a cylindrical

coordinate time-dependent lattice method to study the one electron process of excitation in p+H collisions. Comparing excitation probabilities and cross sections (at 40 keV incident energy) from their previous Cartesian coordinate 3D lattice method and a newly formulated cylindrical coordinate coupled 2D lattice method, the authors obtained reasonable agreement.

Another type of lattice method has been proposed by Sidky and Lin [55]. It is based on the solution of the time-dependent Schrödinger operator on a two-centre momentum space. In this method the problems related to the reflection of the propagated wave function at the boundaries do not happen because momentum-space wave functions go to zero at large momenta. However, the actual calculations are performed after transformation to coordinate representation in order to avoid difficulties in evaluating the convolution integral terms of the Schrödinger equation in momentum space.

To sum up, the facts that lattice techniques are applicable at any impact energy and the time-dependence of the wave function is computed explicitly can be regarded as advantages of the method. But large computer memory resources required for the fine discretization of the space leads to practical limitations.

1.2.4 Close-coupling methods

The close-coupling (CC) method is a widely used theoretical approach to treat collision processes in a fully non-perturbative quantum-mechanical framework. It has been very well described in the literature and general reviews can be found in [56–58]. The method takes into account strong couplings between different possible channels. In general, CC methods are based on expansion of total wave functions of collision systems in complete basis sets, so that the time-dependent Schrödinger equation is replaced by a system of differential equations for the

expansion coefficients. The complete sets can be Slater or Gaussian orbitals, Sturmian- or Laguerre-based functions, B-splines etc. Below we give a brief summary of atomic orbital CC (AOCC) treatments. In the next chapters various CC treatments will be discussed in detail.

In the one-centre CC approaches the time-dependent electronic wave function is approximated in terms of target-based functions. These functions are obtained by diagonalisation of the target Hamiltonian. The method is particularly suitable for antiproton scattering. It has been used to study collision processes in antiproton scattering on atomic [59–63] and molecular [64–66] targets. In the case of proton scattering on atomic targets, single centre CC methods have been shown to provide reliable results for the electron loss. However, an enormously large number of basis functions is needed to account for the two-centre effects of the collision. For example, Ford *et al.* [67] obtained total electron loss cross-sections for proton-hydrogen collisions with 1040 functions. The disadvantage of the single-centre expansion is that one can only extract combined capture and ionisation cross sections, not individual ones.

In the two-centre CC methods the total wave function is expanded over both target and projectile based basis functions with plane-wave translational factors (PWETF) attached [12, 56]. The augmentation of the basis functions with PWETF was proposed by Bates and McCarroll in their pioneering works [68, 69]. McCarroll [70] was the first to apply the method in a two-state approximation (with $1s$ state retained on each nucleus) for the p+H system. This attempt gave good results for capture to the ground state. There were a number of two-centre CC calculations including more eigenstates. A comprehensive work was done by Wilets and Gallaher [71], in which $1s$, $2s$, $2p_0$ and $2p_1$ states were included on both centres. At a few impact energies calculations were also performed including n=3 states. The main significance of this work is an effective usage of

projectile-target nucleus symmetry properties of the proton-hydrogen collision system. Unfortunately, the calculations of Wilets and Gallaher [71] are known to be quite inaccurate due to numerical problems [72, 73]. Cheshire, Gallaher and Taylor [72], while trying an expansion in pseudosates, performed $1s$, $2s$, $2p_0$ and $2p_1$ calculations. The only difference in the calculations was that Cheshire *et al.* used a differential equation method of Cheshire [74] to treat two-centre integrals, whereas two-dimensional numerical integration was used by Wilets and Gallaher [71]. Comparison of the results from these two calculations revealed some severe differences.

As known in the actual implementation of the CC description with two-centre expansions, the main computational expense is paid for the evaluation of the exchange matrix elements [12, 56]. In this context, McCarroll [70] showed that the integration over two dimensions can be carried out analytically in prolate spheroidal coordinates, so that two-centre matrix elements are expressed as one-dimensional integrals. The last integration is evaluated by a Gauss-Laguerre quadrature rule. Extending the method of McCarroll (which was originally for $s - s$ transitions), Fennema [75] gave specific expressions for the integrals involving $1s$, $2s$, $2p$ states. Later on, Rapp and Dinwiddie [76] complemented the tables of Fennema with expressions involving transitions to $n = 3$ eigenstates.

The first two-centre pseudostate-expansion CC approaches were due to Gallaher and Wilets [77], Cheshire [72], and Shakeshaft [78]. Gallaher and Wilets [77] reported transfer and excitation cross sections to the $2s$ and $2p$ states by their eight-state (on each centre) calculations. Also, notably good agreement was found with the experiments of Helbig and Everhart [79]. Cheshire *et al.* [72] made seven state (four hydrogenic states and three pseudostates) calculations. Pseudostates were designed to simulate the molecular features at small separations. Comparing their results with those by Gallaher and Wilets [77], the

authors observed discrepancies (particularly at low energies). For example, at 4 keV their $2p$ excitation cross section was found to be twice larger than the reported values by Gallaher and Wilets. Numerical problems associated with the integration of the coupled equations and asymptotic projection of the amplitudes were shown to be the sources for these discrepancies. Shakeshaft made a significant contribution to the development of coupled channel methods [78, 80–82]. He reported thirty-five scaled-Sturmian function results in [78]. Although the agreement with experiment was not satisfactory, the calculations of Shakeshaft were the largest and probably the most accurate at that time.

The rapid development in the computing technology made it possible to perform large basis-set calculations. However, large basis calculations of Slim and Ermolaev [83] produced oscillatory structures in the excitation cross sections which were not observed experimentally [84–86]. Kuang and Lin [50] attributed the existence of such oscillations to the simultaneous use of pseudocontinuum states on both centres. Hence, they proposed to use an asymmetric (BBC) close-coupling scheme with pseudocontinuum states either on the target (BBC-T) or on the projectile (BBC-P). In their BBC-T calculations excitation cross-sections were stable and well-behaved, but capture cross-sections remained unstable. While BBC-P type expansion produced the opposite picture: capture cross sections were stable, while excitation cross sections became unstable. Thus, using BBC-type expansions, it was not possible to make both excitation and capture cross-sections stable.

The most complete study of proton-hydrogen collision processes by the two-centre close-coupling approach was performed by Toshima [87–89]. Toshima [88] demonstrated that the spurious oscillations observed in the excitation and capture channels are due to the strong coupling effect between bound and pseudocontinuum states belonging to different centres. As evidence, it was shown that

as the density of pseudocontinuum states increased the structures became less prominent. In [89] the author investigated in detail the convergence of ionisation cross sections by performing all three types of calculations. For all three type of expansions consistent ionisation cross sections were obtained. However, the convergence of the asymmetric calculations was shown to be much slower than that of the symmetric one.

The most recent investigation of capture, excitation and ionisation in the system collisions is due to Winter [90]. Extending Shakeshaft's Sturmian calculations by including large number of pseudostates, the author compares electron transfer and excitation cross sections with the results from other theoretical approaches and experimental observations. For ionisation channel, the results of Winter are in agreement with those by Toshima.

The triple-centre model was proposed by Anderson *et al.* [91] and Antal *et al.* [92]. It was investigated extensively by Lin *et al.* [93], Winter and Lin [94] for the symmetric collision system p+H. In this model atomic wave functions of the united atom He^+ are placed at the centre between the two nuclei. The available calculations for ionisation in collisions of p with H [95, 96] and He^+ [97] show that triple-centre method results in reliable ionisation cross sections at energies as low as several keV and agree better with the experimental data.

An interesting development of the close-coupling approach has been proposed by Kroneisen *et al.* [98] and Kirchner *et al.* [99]. Since the CC formalism is based on the variational principle [100, 101], it is generally believed that increasing the number of basis functions should lead to better results. Although in calculations the number of basis functions become rather large, this number is finite. This means that a finite model space is used while propagating an initial wave function and all the couplings to the complementary part of Hilbert space

is neglected. The authors proposed an approach, named basis generator method (BGM), that provides a basis adapting dynamically to the collision process in order to follow the propagation and to cover the one-dimensional subspace by the solution of the TDSE. As a first test of the method antiproton collisions with hydrogen atoms and helium ion are studied [98]. Excitation and ionisation cross-sections obtained by much smaller BGM basis functions (57, 54 states for H and He^+, respectively) agree well with other calculations. Two-centre implementation of the method has been reported in [102, 103].

Despite the overall success of semi-classical close-coupling approaches, the results of various calculations for the seemingly simplest proton-hydrogen system differ. This is especially true for the ionisation channel. At the ionisation peak the disagreement between the best known theory [89] and the experiment [104, 105] is almost 30%. This suggests that new approaches to the problem need to be developed. In this thesis a new time-dependent two-centre convergent close-coupling method will be introduced. Detailed description of the method will be given in Chapter 5.

1.3 Chapter summary

In this Chapter a short discussion on the importance of ion collisions with atomic/molecular targets and overview of the methods used to study collision processes in these systems at intermediate impact energies have been given. Particular attention has been given to recent developments of each theoretical treatment. As stated earlier, all the theoretical tools have their own limitations.

There is another class of coupled channel methods that has not been reviewed here. This is a convergent close-coupling (CCC) method successfully used for studying collisions of photons and electrons with hydrogen, helium, alkali and

alkali earth atoms [106–112]. The approach has been extended to the case of positron [113–118] and antiproton [119, 120] collisions with atoms and molecules This method successfully describes the main features of ionisation processes, including total and differential cross sections. However, the extension of the method for ion-atom collisions involving charge exchange processes has not been published yet.

As noted earlier, the purpose of the thesis is to develop a semi-classical CCC formalism. The basic outline of the single centre method (in Chapter 2) will be followed by its extension to the antiproton collisions with multi electron and molecular targets in Chapters 3 and 4, respectively. In Chapter 5 two-centre extension of the semi-classical CCC method will be given. Chapter 6 presents preliminary results of the application of the two-centre technique to proton-hydrogen collisions.

Atomic units are used throughout the thesis unless otherwise specified.

Chapter 2

Single-centre time-dependent convergent close-coupling method

2.1 Introduction

The semi-classical close-coupling (CC) approach is one of the methods used to study collisions of antiprotons with atomic and molecular targets. General reviews on the CC method can be found in [56, 57]. In the CC formalism the electronic wave function is expanded around the target nucleus using a suitable basis: Hall *et al.* [121] used Slater orbitals, Igarashi *et al.* [122] Laguerre-based functions, Toshima [123] Gaussian-type orbitals, Winter [124] Sturmian functions, Sahoo *et al.* [125] and Lühr and Saenz [126] B-splines.

All of the methods mentioned above rely on a single-centre expansion except for Toshima and Winter, who have performed both one-centre and two-centre calculations for ionisation of atomic hydrogen by antiproton impact. They have concluded that only at energies below 1 keV the two-centre effect on the total ionisation cross section is pronounced, with convergence in the two-centre calculations being reached with much lower orbital angular momentum states.

All semi-classical approaches assume the relative motion of the antiproton and the target as free motion with a constant velocity along a straight line. The validity of these semi-classical approaches was confirmed earlier at intermediate incident energies [127–130]. Bates [127] established the equivalence between the fully quantal wave and impact parameter approaches by considering the electron capture process. Mittleman [128], Wilets and Wallace [129], McCarroll and Salin [130] later investigated the effect of the deviation from the rectilinear relative motion of the heavy particles. Overall, it was concluded that the correction due to this effect was unimportant in calculating integrated cross sections. The CC approach of McGovern *et al.* [131], based on the straight line approximation, allows not only calculation of the total cross sections but also extraction of the fully differential cross sections for ionisation. These authors have further developed their formalism and gave a new approximation which allows the differential analysis of ionisation over a range of ejected electron energies in a single calculation [132].

In this chapter we will present the basic formalism of the single-centre time-dependent convergent close-coupling (CCC) approach for antiproton collisions with atomic hydrogen. Following the standard close-coupling scheme [12, 56], the total scattering wave function will be expanded in terms of target functions. For the target description we will follow the ideas of the original CCC method (based on Lippmann-Schwinger-type equations) which has demonstrated great success in dealing with light projectiles in examples of collisions of electrons [133] and positrons [134] with hydrogen and positrons with helium [115, 135]. Recently, the convergent close-coupling approach has been developed for collisions of antiprotons with light atoms (H and He) [119, 120, 136]. This approach is a fully quantum-mechanical time-independent method based on the Schrödinger equation for the total scattering wave function and leads to a system of integral

equations for the transition amplitudes.

The central ingredients in the close-coupling approach are the interaction matrix elements. These matrix elements are obtained by expressing the interaction potential between the projectile and the target in a basis of the electronic states of the target. For simplicity, in this chapter we describe how this interaction matrix element is calculated for antiproton-hydrogen collisions.

2.2 Method

Ion-atom collisions can be classified according to the impact energy (or, equivalently, according to the impact velocity) of the ions. When the collision energy is very low, ion-atom scattering is treated by the partial-wave expansion methods. However, as the relative velocity of the projectile v becomes comparable to v_0 (the atomic unit of velocity), the number of partial waves required to get convergence increases drastically. At collision energies of several hundred eV, the following conditions are satisfied [57]:

- the de Broglie wavelength of the relative motion of the heavy particles (nuclei) is small compared with atomic dimensions;
- the relative momentum of the nuclei, k, satisfies the relation $k^2/2\mu \gg \Delta E$, where μ is the reduced mass of the colliding system and ΔE is the inelasticity (energy difference of relevant states) in the collision;
- scattering of the projectile occurs at small scattering angles.

Under such conditions, the nuclei can be assumed to be moving along the classical path and the electrons are under the influence of the time-dependent force due to the moving nuclei. Hence the electronic wave functions must satisfy

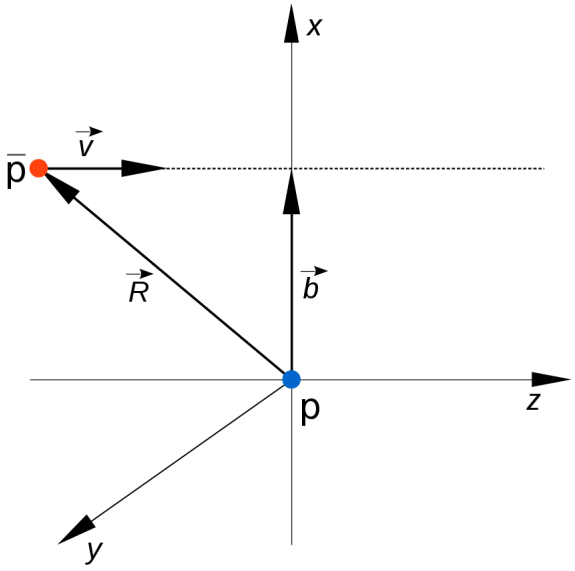

Figure 2.1: Laboratory frame coordinates for antiproton collisions with atomic hydrogen (the electron is not shown). Target centre is chosen as the origin of coordinates. The projectile moves along a straight-line. z-axis is directed along the incidence.

a time-dependent Schrödinger equation. This semi-classical approximation provides a simpler picture of the collision dynamics and eventually simplifies the computations. It should be stated that the use of the semi-classical approximation is known to provide quantitatively accurate results in the keV collision energy region [56].

We consider the collision process of an antiproton with the hydrogen atom in the ground state. The antiproton is assumed to be moving with velocity $\boldsymbol{v}$ along a straight-line trajectory (Figure 2.1). The position of the projectile is determined by

$$\boldsymbol{R}(t) = \boldsymbol{b} + \boldsymbol{v}t, \tag{2.1}$$

with $\boldsymbol{b}$ being the impact parameter.

The total three-body scattering wave function Ψ at a total energy E satisfies the Schrödinger equation

$$H\Psi = E\Psi, \tag{2.2}$$

where the Hamiltonian

$$H = T + V^{\text{tot}} \tag{2.3}$$

consists of the kinetic energy operator

$$T = -\frac{1}{2\mu}\nabla^2_{\boldsymbol{\sigma}} - \frac{1}{2}\nabla^2_{\boldsymbol{r}}, \tag{2.4}$$

and the interaction potential

$$V^{\text{tot}} = -\frac{1}{r} + \frac{1}{|\boldsymbol{R} - \boldsymbol{r}|} - \frac{1}{R}, \tag{2.5}$$

with μ being the reduced mass of the projectile-target system, $\boldsymbol{R}$ and $\boldsymbol{r}$ are the positions of the incident antiproton and the orbital electron relative to the nucleus of the hydrogen, respectively. $\boldsymbol{\sigma}$ is the position of the incident antiproton with respect to the centre of mass of the target system (Figure 2.2).

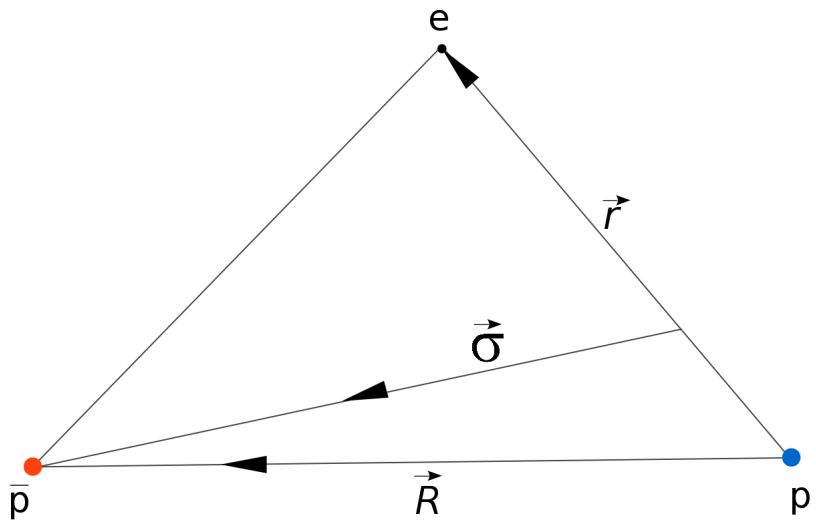

Figure 2.2: Jacobi coordinates for antiproton-hydrogen collisions.

We do the substitution

$$\Psi(\boldsymbol{r},\boldsymbol{\sigma}) = \bar{F}(\boldsymbol{\sigma})\bar{\Psi}(\boldsymbol{r},\boldsymbol{\sigma}), \tag{2.6}$$

where $\bar{F}(\boldsymbol{\sigma})$ satisfies the free-particle equation

$$\left[-\frac{1}{2\mu}\nabla^2_{\boldsymbol{\sigma}} - \frac{k_i^2}{2\mu}\right]\bar{F}(\boldsymbol{\sigma}) = 0. \tag{2.7}$$

In (2.7) $k_i^2/2\mu$ is the kinetic energy of relative motion in the channel i and

$$\frac{k_i^2}{2\mu} \equiv E - \epsilon_i, \tag{2.8}$$

with ϵ_i being the eigenenergy corresponding to channel i. Inserting (2.6) into (2.2), we find that Eq. (2.2) takes the form

$$-\frac{1}{2\mu}\bar{F}(\boldsymbol{\sigma})\nabla^2_{\boldsymbol{\sigma}}\bar{\Psi}(\boldsymbol{r},\boldsymbol{\sigma}) - \frac{1}{\mu}\nabla_{\boldsymbol{\sigma}}\bar{F}(\boldsymbol{\sigma})\nabla_{\boldsymbol{\sigma}}\bar{\Psi}(\boldsymbol{r},\boldsymbol{\sigma}) + \bar{F}(\boldsymbol{\sigma})H_e\bar{\Psi}(\boldsymbol{r},\boldsymbol{\sigma}) = 0, \tag{2.9}$$

with the electronic Hamiltonian

$$H_e = -\frac{1}{2}\nabla^2_{\boldsymbol{r}} + V^{\rm tot}. \tag{2.10}$$

If semi-classical conditions apply, the first term in (2.9) can be neglected compared with the second (see chapter 3 in [13]). Both $\bar{\Psi}$ and H_e depend on $\boldsymbol{R}$ which can in turn be expressed in terms of $\boldsymbol{b}$ and the time t by the trajectory equation (2.1). In what follows $\boldsymbol{R}$ dependence of the wave function will be shown explicitly. In this semi-classical approximation Eq. (2.2) is reduced to the time-dependent Schrödinger equation

$$i\frac{\partial\bar{\Psi}(t,\boldsymbol{r},\boldsymbol{R})}{\partial t} = H_e\bar{\Psi}(t,\boldsymbol{r},\boldsymbol{R}). \tag{2.11}$$

In obtaining Eq. (2.11), $\nabla_{\boldsymbol{\sigma}}$ is replaced by a time-derivative using the relations:

$$\frac{1}{\bar{F}(\boldsymbol{\sigma})}\left[-\frac{1}{\mu}\nabla_{\boldsymbol{\sigma}}\bar{F}(\boldsymbol{\sigma})\nabla_{\boldsymbol{\sigma}}\right] = -i\boldsymbol{v}\nabla_{\boldsymbol{\sigma}} = -i\frac{\partial}{\partial t}. \tag{2.12}$$

The electronic Hamiltonian of the antiproton and target atom scattering system can be written as

$$H_e = H_\mathrm{t} + V, \tag{2.13}$$

where H_t is the target atom Hamiltonian and V is the antiproton-target interaction potential.

The electronic scattering wave function is expanded in terms of a certain set of N target pseudostates $\{\psi_\alpha\}$ according to

$$\bar{\Psi}(t, \boldsymbol{r}, \boldsymbol{R}) = \sum_{\alpha=1}^{N} A_\alpha(t, \boldsymbol{b}) e^{-i\epsilon_\alpha t} \psi_\alpha(\boldsymbol{r}), \tag{2.14}$$

where ϵ_α is the energy of the target electronic state α,

$$H_\mathrm{t}\psi_\alpha = \epsilon_\alpha \psi_\alpha, \tag{2.15}$$

and functions $\psi(\boldsymbol{r})$ are orthogonal

$$\langle \psi_\alpha | \psi_{\alpha'} \rangle = \delta_{\alpha\alpha'}. \tag{2.16}$$

Substituting the expansion (2.14) into Eq. (2.11) one obtains

$$\begin{aligned} &i\sum_{\alpha=1}^{N} \frac{dA_\alpha(t, \boldsymbol{b})}{dt} e^{-i\epsilon_\alpha t}\psi_\alpha + i\sum_{\alpha=1}^{N} A_\alpha(t, \boldsymbol{b})(-i\epsilon_\alpha) e^{-i\epsilon_\alpha t}\psi_\alpha \\ &= \sum_{\alpha=1}^{N} A_\alpha(t, \boldsymbol{b}) e^{-i\epsilon_\alpha t} H_\mathrm{t}\psi_\alpha + V\sum_{\alpha=1}^{N} A_\alpha(t, \boldsymbol{b}) e^{-i\epsilon_\alpha t}\psi_\alpha. \end{aligned} \tag{2.17}$$

Taking into account (2.15) Eq. (2.17) can be reduced to

$$i\sum_{\alpha=1}^{N} \frac{dA_\alpha(t, \boldsymbol{b})}{dt} e^{-i\epsilon_\alpha t}\psi_\alpha = V\sum_{\alpha=1}^{N} A_\alpha(t, \boldsymbol{b}) e^{-i\epsilon_\alpha t}\psi_\alpha. \tag{2.18}$$

Multiplying Eq. (2.18) by $e^{i\epsilon_{\alpha'} t}\psi_{\alpha'}$ and integrating over $\boldsymbol{r}$ we get

$$i\frac{dA_\alpha(t, \boldsymbol{b})}{dt} = \sum_{\alpha'=1}^{N} A_{\alpha'}(t, \boldsymbol{b}) \langle \psi_\alpha | V(t, \boldsymbol{r}, \boldsymbol{b}) | \psi_{\alpha'} \rangle e^{i(\epsilon_\alpha - \epsilon_{\alpha'})t} \quad \text{with} \quad n = 1, \ldots, N, \tag{2.19}$$

where the orthogonality of functions $\psi(\boldsymbol{r})$ according to Eq. (2.16) is taken into account. The set of Eqs. (2.19) is solved with the initial conditions $A_\alpha(t = -\infty, \boldsymbol{b}) = \delta_{\alpha i}$ (as the target is initially in the ground state ψ_i).

The probability to find the system in final state f is

$$P_f(b) = |A_f(+\infty, \boldsymbol{b})|^2, \tag{2.20}$$

where $A_f(+\infty, \boldsymbol{b})$ is the (complex) transition amplitude. The coupled equations should be solved for a range of impact parameters and the partial cross section for the transition to state f is calculated by

$$\sigma_f = 2\pi \int_0^\infty db\ bP_f(b). \tag{2.21}$$

The total ionisation cross section is the sum of the partial cross sections corresponding to transitions into the positive energy pseudostates

$$\sigma_{\text{tot}}^{\text{ion}} = \sum_{f,\epsilon_f>0} \sigma_f. \tag{2.22}$$

The derived set of the coupled equations is also valid for multi-electron atoms. It can be used for molecular targets as well, provided that the Born-Oppenheimer (BO) approximation is employed. The BO approximation allows to separate the motion of the fast electrons from the slow motion of the target nuclei [12]. For molecular targets, the Schrödinger equation for the electronic part of the molecular wave function can be solved for a fixed internuclear distance.

The interaction matrix elements $\langle\psi_\alpha|V(t, \boldsymbol{r}, \boldsymbol{b})|\psi_{\alpha'}\rangle$ contain all the information about the collision. They are different for various collision systems. The calculation of these matrix elements requires the knowledge of the structure of the considered target. In this chapter we describe how these matrix elements are calculated for the antiproton-hydrogen collision system. First we describe our

approach to generating the pseudostates for the atomic hydrogen target. In the next chapters, the matrix elements for antiproton collisions with multi-electron and molecular targets will be derived.

2.3 Laguerre basis functions

For atomic hydrogen the pseudostates $\psi_\alpha(\boldsymbol{r}) \equiv \psi_{nlm}(\boldsymbol{r})$ (where n, l and m are the principal, orbital and magnetic quantum numbers of the state α, respectively) can be written as

$$\psi_{nlm}(\boldsymbol{r}) = \phi_{nl}(r) Y_{lm}(\hat{r}), \tag{2.23}$$

where

$$\phi_{nl}(r) = \sum_{k=1}^{N_l} c_{nk}^l \xi_{kl}(r), \tag{2.24}$$

and the basis functions $\xi_{kl}(r)$ are made of the orthogonal Laguerre functions

$$\xi_{kl}(r) = \sqrt{\frac{\lambda_l (k-1)!}{(2l+1+k)!}} (\lambda_l r)^{l+1} e^{-\lambda_l r/2} L_{k-1}^{2l+2}(\lambda_l r). \tag{2.25}$$

Here $L_{k-1}^{2l+2}(\lambda_l r)$ are the associated Laguerre polynomials. Expansion coefficients c_{nk}^l are found by diagonalising the target Hamiltonian

$$\langle \psi_\beta | H_\mathrm{t} | \psi_\alpha \rangle = \epsilon_\alpha \delta_{\beta\alpha}. \tag{2.26}$$

The diagonalisation procedure gives negative- and positive-energy pseudostates. As the number of pseudostates in each target symmetry increases the lowest negative-energy pseudostates converge to H eigenstates while the positive energy pseudostates represent an increasingly dense discretization of the continuum. An example of the electron energy levels for atomic hydrogen is displayed in Figure 2.3. The value of maximum orbital angular momentum in this spectrum is

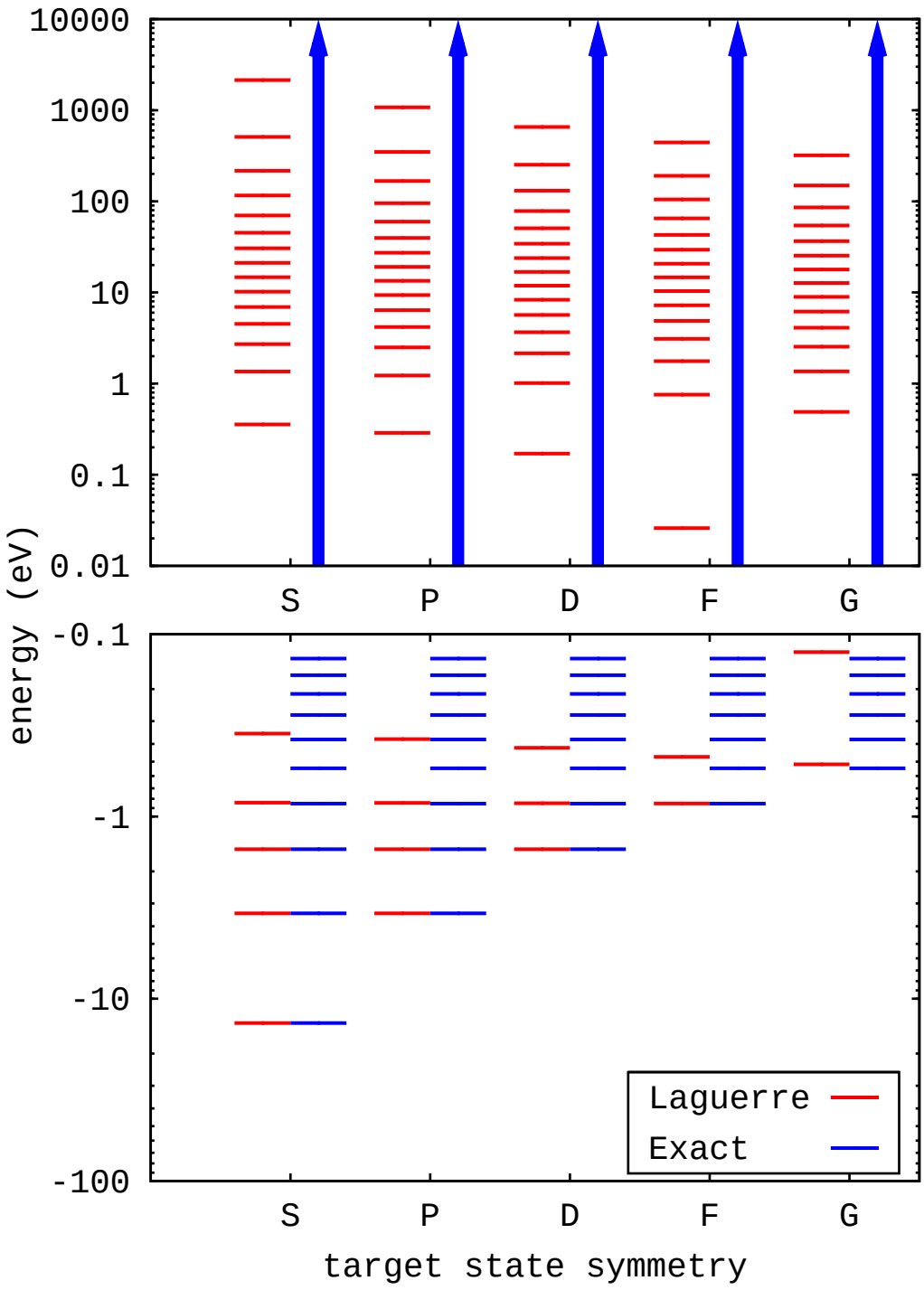

Figure 2.3: Energy levels of atomic hydrogen obtained in the orthogonal Laguerre basis. The size of the Laguerre basis is $N_l = 20 - l$ and the exponential fall-off parameter is $\lambda_l = 1$. For comparison exact eigenenergies for $n \leq 10$ are also shown.

$l_{\max}$ =4, while the number of Laguerre functions is $N_l = n_{\max} - l$ with $n_{\max} = 20$. The value of the exponential fall-off parameter is $\lambda_l = 1$.

In principle, the results of calculations do not depend on the fall-off parameter λ_l, however the rate of convergence does. Therefore, λ_l is chosen on the basis of practical convenience. The particular choice of this parameter will be considered in the next chapters.

2.4 Coupling matrix elements for antiproton-hydrogen collisions

The matrix element $V_{\alpha\alpha'}(\boldsymbol{R}) \equiv \langle\psi_\alpha|V(t,\boldsymbol{r},\boldsymbol{b})|\psi_{\alpha'}\rangle$ for antiproton-hydrogen system is given by (see Figure 2.2)

$$V_{\alpha\alpha'}(\boldsymbol{R}) = \int d\boldsymbol{r}\ \psi^*_\alpha(\boldsymbol{r}) \left(-\frac{1}{R} + \frac{1}{|\boldsymbol{R}-\boldsymbol{r}|}\right) \psi_{\alpha'}(\boldsymbol{r}). \tag{2.27}$$

The potential $1/|\boldsymbol{R}-\boldsymbol{r}|$ may be expanded using the relation [137]

$$\frac{1}{|\boldsymbol{r}_1-\boldsymbol{r}_2|} = 4\pi \sum_{\lambda\mu} \frac{\tilde{U}_\lambda(r_1,r_2)}{2\lambda+1} Y^*_{\lambda\mu}(\widehat{\boldsymbol{r}_1}) Y_{\lambda\mu}(\widehat{\boldsymbol{r}_2}), \tag{2.28}$$

where $\widehat{\boldsymbol{r}_1}$, $\widehat{\boldsymbol{r}_2}$ are the directions of two vectors $\boldsymbol{r}_1$, $\boldsymbol{r}_2$, and $\tilde{U}_\lambda(r_1,r_2)$ is given by

$$\tilde{U}_\lambda(r_1,r_2) = \begin{cases} \frac{r_1^\lambda}{r_2^{\lambda+1}}, & \text{for } r_1 \le r_2, \\ \frac{r_2^\lambda}{r_1^{\lambda+1}}, & \text{for } r_1 > r_2. \end{cases} \tag{2.29}$$

Using expansion (2.28) one can write the potential interaction as

$$-\frac{1}{R} + \frac{1}{|\boldsymbol{R}-\boldsymbol{r}|} = 4\pi \sum_{\lambda\mu} \frac{U_\lambda(R,r)}{2\lambda+1} Y^*_{\lambda\mu}(\widehat{\boldsymbol{R}}) Y_{\lambda\mu}(\widehat{\boldsymbol{r}}), \tag{2.30}$$

with

$$U_\lambda(R,r) = \begin{cases} -\frac{\delta_{\lambda 0}}{R} + \frac{R^\lambda}{r^{\lambda+1}}, & \text{for } R \le r, \\ -\frac{\delta_{\lambda 0}}{R} + \frac{r^\lambda}{R^{\lambda+1}}, & \text{for } R > r. \end{cases} \tag{2.31}$$

Consequently, Eq. (2.27) takes the form

$$V_{\alpha\alpha'}(\boldsymbol{R}) = 4\pi \sum_{\lambda\mu} \frac{Y^*_{\lambda\mu}(\widehat{\boldsymbol{R}})}{2\lambda+1} \int_0^\infty dr\ r^2 R_{n_\alpha l_\alpha}(r) U_\lambda(R,r) R_{n_{\alpha'} l_{\alpha'}}(r) \times \int d\widehat{\boldsymbol{r}}\ Y^*_{l_\alpha m_\alpha}(\widehat{\boldsymbol{r}}) Y_{\lambda\mu}(\widehat{\boldsymbol{r}}) Y_{l_{\alpha'} m_{\alpha'}}(\widehat{\boldsymbol{r}}). \quad (2.32)$$

The angular integration over the product of the three spherical harmonics is performed using the formula [137]

$$\int d\widehat{\boldsymbol{r}}\ Y^*_{LM}(\widehat{\boldsymbol{r}}) Y_{L_1M_1}(\widehat{\boldsymbol{r}}) Y_{L_2M_2}(\widehat{\boldsymbol{r}}) = \sqrt{\frac{[L_1][L_2]}{4\pi[L]}} C^{L0}_{L_10\ L_20} C^{LM}_{L_1M_1\ L_2M_2}, \quad (2.33)$$

where $C^{ef}_{ab\ cd}$ are the Clebsch-Gordan coefficients and $[L] \equiv 2L+1$. With this we can further reduce Eq. (2.32) to

$$V_{\alpha\alpha'}(\boldsymbol{R}) = \sqrt{\frac{4\pi[\ell_{\alpha'}]}{[\ell_\alpha]}} \sum_{\lambda\mu} \frac{C^{l_\alpha 0}_{\lambda 0\ l_{\alpha'} 0} C^{l_\alpha m_\alpha}_{\lambda\mu\ l_{\alpha'} m_{\alpha'}}}{\sqrt{[\lambda]}} Y^*_{\lambda\mu}(\widehat{\boldsymbol{R}}) \times \int_0^\infty dr\ r^2 \phi_{n_\alpha l_\alpha}(r) U_\lambda(R,r) \phi_{n_{\alpha'} l_{\alpha'}}(r). \quad (2.34)$$

2.5 Antiproton scattering on the hydrogen atom

We have performed calculations for antiproton scattering on the hydrogen atom in the ground state in the impact energy range from 1 keV to 1 MeV. Below we give the details of the calculations and comparison of the obtained results with available theoretical calculations.

First we discuss the calculation procedure of the radial integral in (2.34). In practice the upper limit of the radial integration is $r_{\max}$ and this integration is performed by Simpson's rule. In order to make sure that $r_{\max}$ is high enough and the radial mesh is sufficiently dense we check the orthonormality condition of the pseudostates. To accommodate radial integrations involving oscillatory pseudocontinuum functions we allow up to 2000 subdivisions of the interval

$(0, r_{\max})$. In the calculations $r_{\max}$ is set to be 150 a.u. and the deviation from the orthonormality condition is always less than 10^{-6}. The use of such a dense mesh allows us to calculate the radial integrations of the form (2.34) accurately.

The other numerical aspect is related to the integration of the coupled first order differential equations (2.19) along $Z(\equiv vt)$. For such tasks it is common to use various adaptive step-size techniques. However, we utilised a different approach for this problem. This approach is based on the propagation of the coupled equations along a predefined dense mesh in the range $(-Z_{\max}, Z_{\max})$. For the propagation method we again used Simpson's rule. The accuracy of this differential equation solver is improved by making the mesh denser. From practice it has been found that the mesh should be extremely dense around $Z = 0$. In the calculations we have 2000 mesh points in $(-Z_{\max}, Z_{\max})$ range. Also, the violation from the unitarity has never exceeded 10^{-6} for all the impact parameters considered.

Expansion methods need to be checked for convergence by increasing the size of the basis. The convergence of cross-sections has been studied with increasing Laguerre basis size. First we fix the basis parameter $n_{\max}$ at some large value and systematically increase parameter $l_{\max}$ starting from 0. Fig. 2.4 shows convergence of the total ionisation cross section (TICS) with increasing $l_{\max}$, while $n_{\max} = 20$ for each l. We observe fast convergence with $l_{\max}$. Especially at collision energies below 10 keV, where the inclusion of S, P and D states gives sufficiently good convergence. One can expect that as the emission energy increases the higher angular momentum states are necessary to get convergence. However, our calculations show that the inclusion of the pesudostates with $l_{\max} = 5$ are enough for the convergence of the total ionisation cross section for the entire range of impact energy.

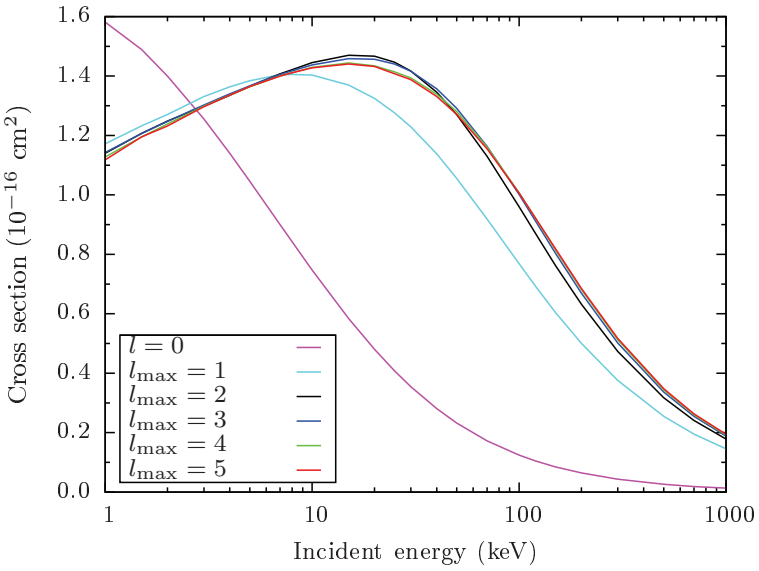

Figure 2.4: Convergence of the total ionisation cross section for $\bar{p}$+H(1s) with increasing $l_{\max}$ at $n_{\max} = 20$.

To have a more clear convergence picture, we plot TICS as a function of $l_{\max}$ at projectile energies 5, 15 and 100 keV (see Fig. 2.5). At 5, 15 and 100 keV the difference between the TICS with $l_{\max} = 4$ and $l_{\max} = 5$ are 0.18%, 0.42% and 0.26%, respectively. From these studies, one can conclude that $l_{\max} = 5$ is sufficient for the entire energy interval of our interest provided $n_{\max} = 20$. Next we check the convergence of TICS with $n_{\max}$ by setting $l_{\max} = 5$. Fig. 2.6 shows this dependence at three chosen impact energies. After $n_{\max} = 10$, we observe a monotonic increase of TICS for all considered energies. The variations in the cross section when $n_{\max}$ changes from 19 to 20 at energies 5, 15 and 100 keV are 0.15%, 0.08% and 0.76%, respectively. Thus, based on the convergence study we conclude that the basis with $n_{\max} = 20$ and $l_{\max} = 5$, which results in the 595 states, is suitable for the full-scale calculations.

In all the calculations for the antiproton scattering on the hydrogen the fall-off parameter of the Laguerre functions λ_l is 1. The convergence rate of the cross sections was found to be fastest with this value of the parameter in

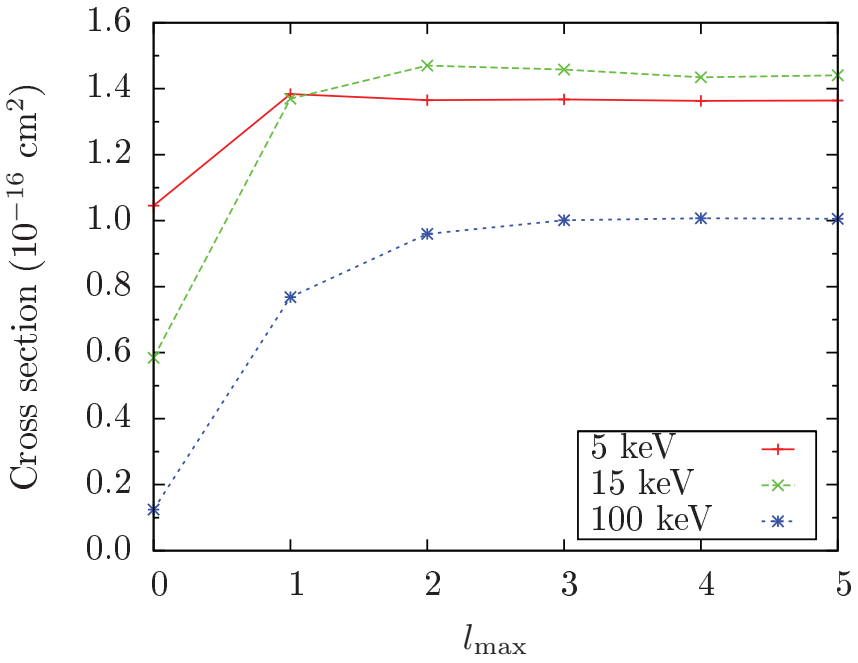

Figure 2.5: Convergence of the total ionisation cross section for the impact energies 5, 15 and 100 keV with increasing $l_{\max}$ at $n_{\max} = 20$.

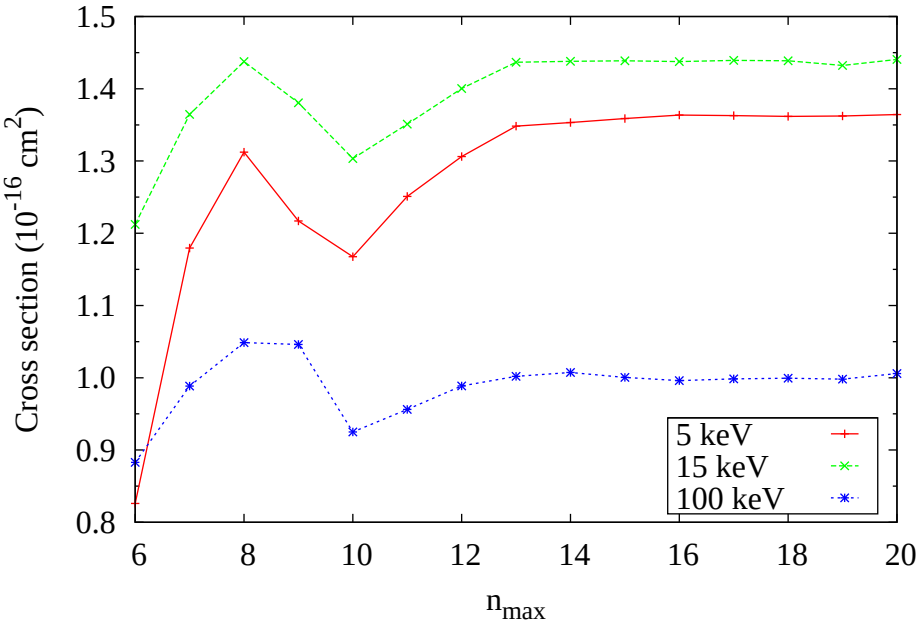

Figure 2.6: Convergence of the total ionisation cross section for the impact energies 5, 15 and 100 keV with increasing $n_{\max}$ at $l_{\max} = 5$.

the calculations of Abdurakhmanov *et al.* [119]. Another numerical parameter for the calculations is $Z_{\max}$, the maximum value of Z used to integrate the system of coupled differential equations (2.19). $Z_{\max} = 120$ a.u. has been set in the calculations. However, calculations have been performed to check the sensitivity of the results to this parameter by increasing the value of $Z_{\max}$ to 150 and 180 a.u. at several impact energies. These tests show that the variation in the cross sections is always less than 1%.

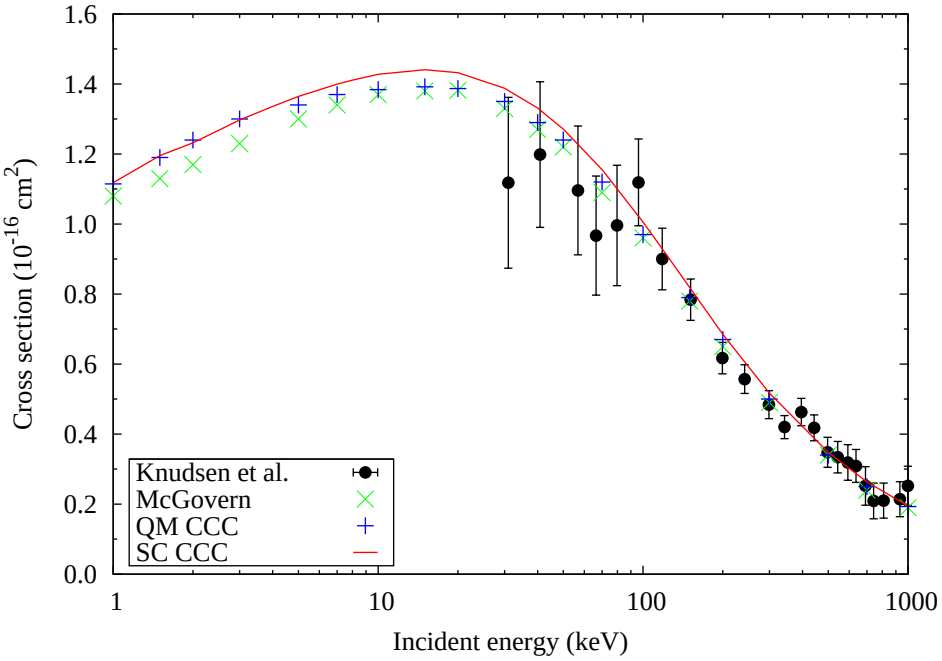

Figure 2.7: Total ionisation cross section for antiproton-hydrogen scattering. The present time-dependent semi-classical CCC calculations are denoted as SC CCC. Comparison is made with the experimental data by Knudsen *et al.* [138], and theoretical calculations by the fully quantum-mechanical CCC (QM CCC) [119] and semi-classical CC results of McGovern [131].

Having checked the results for convergence, we compare them with those from literature. In Fig. 2.7 our results for the total ionisation cross section are presented in comparison with the experimental data by Knudsen *et al.* [138] as well as fully quantum-mechanical CCC (QM CCC) of Abdurakhmanov *et al.* [119]

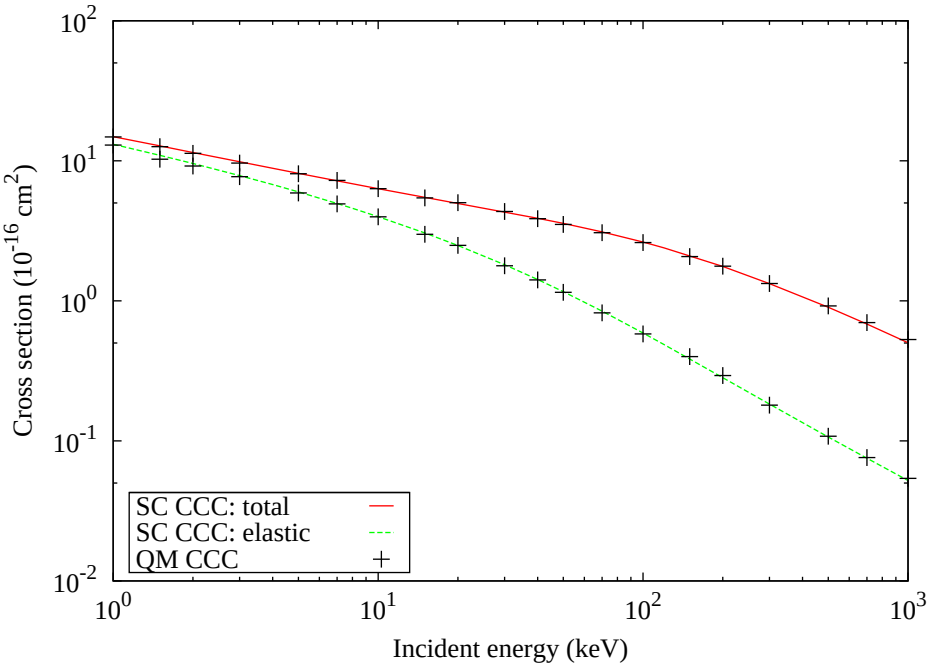

Figure 2.8: Total and elastic cross sections for antiproton-hydrogen scattering. The fully quantum-mechanical CCC calculations are due to Abdurakhmanov *et al.* [119].

and semi-classical calculations of McGovern [131]. The experimental data is normalized to the first Born cross section at high energies [139]. The results are in reasonably good agreement with the experiment. As far as the comparison with other calculations is concerned, we see that the overall agreement is good. However, there are some discrepancies possibly due to different numerical techniques used. At lower energies, the agreement of the SC CCC and QM CCC is rather good, while at about 15 keV this deviation is about 3%. The deviation of this level is observed between the cross sections by SC CCC and McGovern's calculations up to about 20 keV. The agreement among the calculations becomes much better at higher energies. Fig. 2.8 compares the total and elastic cross sections by SC CCC and QM CCC methods. Fig. 2.8 shows perfect agreement between these two approaches at all displayed energies. This agreement is supported by the impact parameter dependence of the weighted ionisation probabilities at

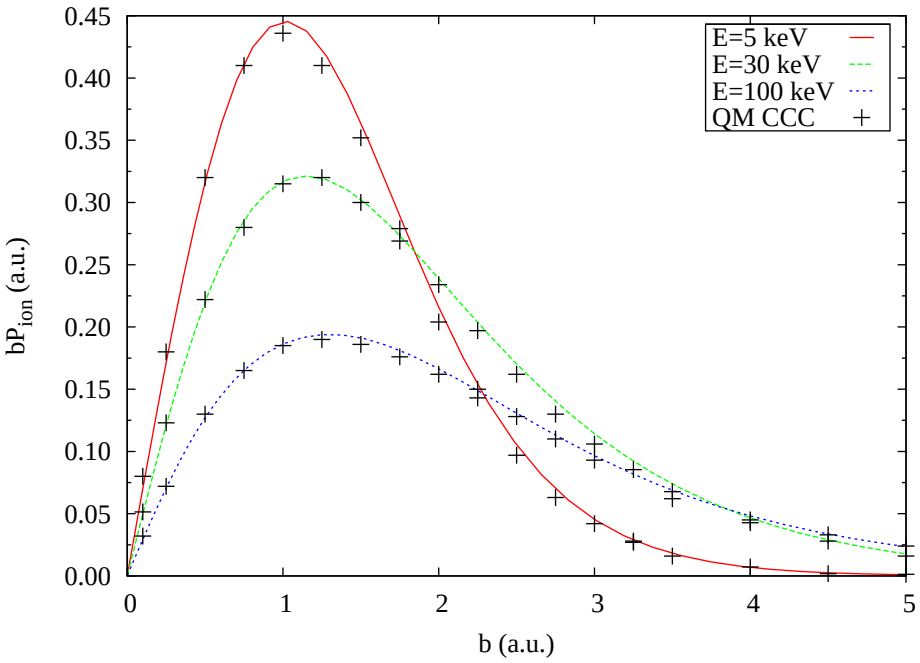

Figure 2.9: Impact parameter dependencies of the weighted ionisation probability at different impact energies are compared with those from the fully quantum-mechanical CCC [119].

selected incident energies shown in Fig. 2.9.

2.6 Chapter summary

In this chapter we have outlined our basic formalism of the single-centre convergent close-coupling approach. According to the formulation of the CCC approach target functions are expanded in terms of the Laguerre-based functions. The main idea behind CCC is to expand the total wave function using a sufficiently large orthogonal Laguerre basis in order to obtain converged amplitudes for all possible atomic excitation and ionisation processes. The target Hamiltonian is diagonalised in this basis yielding negative- and positive- energy pseudostates. With increasing basis size the negative-energy pseudostates converge to the true discrete eigenstates, while the positive-energy states provide

an increasingly dense discretization of the continuum. Convergence in the cross sections of interest is obtained by increasing the basis size.

For validation purposes the method has been applied to the antiproton scattering on the hydrogen atom in the ground state. The results of the calculations are compared with those from the fully quantum-mechanical CCC [119] and semi-classical approach of McGovern [131] in the impact energy range from 1 keV to 1 MeV. Overall reasonably good agreement validates the SC CCC method. In the next two chapters, the method will be applied to study collision processes in multi-electron atomic and molecular targets by antiproton impact. The method will be extended to two-centre case in Chapter 5.

Chapter 3

Antiproton collisions with multi-electron atoms

3.1 Introduction

Extensive experimental investigations of antiproton scattering on inert gas atoms have been performed by Andersen *et al.* [140], Paludan *et al.* [141] and Knudsen *et al.* [142]. Further experiments planned at CERN Antiproton Decelerator [143] and Facility for Antiproton and Ion Research (FAIR) [1] of GSI (Gesellschaft für Schwerionenforschung) will be able to provide accurate experimental data for the total, as well as various differential cross sections for antiproton collisions with a variety of targets.

From the theoretical aspect, a number of methods have been developed to model antiproton scattering on multi-electron atoms [8]. Kirschner *et al.* [144, 145] have investigated single- and multiple-electron processes for medium-energy antiproton collisions with noble gas targets in a semi-classical, time-dependent, independent-particle model using density-functional theory (DFT). The model was constructed using the stationary optimised potential method (OPM) of DFT, relying on an accurate description of the target ground state.

The OPM method represented the exact exchange-only limit of the exchange-correlation functional of DFT. It was shown that a proper treatment of exchange effects in this model is crucial for the prediction of accurate ionisation cross sections. The calculations for ionisation of neon and argon targets by antiprotons (and protons) were carried out with frozen target potentials. The frozen target potentials accounted for the electron exchange effects. A set of single-particle, time-dependent Schrödinger equations resulting from the semi-classical approximation to the collision problem was solved using the so-called basis generator method (BGM). The IPM-BGM approach was applied successfully to calculate the integrated cross sections for processes taking place in antiproton collisions with noble gases, including single and multiple excitation and ionisation of target electrons. In particular, the role of dynamical screening effects was analysed and a simple model for their inclusion was proposed in the case of antiproton scattering [144, 145].

Montanari and Miraglia [146] employed a perturbative continuum-distorted wave-eikonal-initial state (CDW-EIS) approximation to calculate the single and multiple ionisation for antiproton (and proton) impact on rare gas atoms in the energy range from 25 keV to 10 MeV. In their treatment the electron-electron correlations were excluded. Despite this they obtained results which seem to agree with the experiment for Ne and Ar better than the IPM-BGM results. Moreover, for the heavier Kr and Xe atoms the agreement appears to become even better.

In this chapter we present our theoretical multi-electron treatment of single-ionisation in antiproton collisions with noble gas atoms. In this context we generalise the semi-classical time-dependent convergent close-coupling method described in the previous chapter for multi-electron targets. The target structure is modelled as six p-electrons above an inert Hartree-Fock core, in the same way

as was done for positron scattering [147]. One-electron excitations from the outer p-shell are considered. The results of the calculations are compared with other theoretical calculations and the experiments.

3.2 Target structure calculations

Noble gas structure calculations are performed by the procedure described in Ref. [147]. Below the main ideas and formulae are given in order to facilitate calculations of effective potentials in the impact-parameter representation. We emphasise that when antiproton scattering from noble gases is studied in the semi-classical impact-parameter approach, the target electrons are treated fully quantum-mechanically. As the inclusion of all target electrons is not practically feasible, in what follows only $N = 6$ outermost p shell electrons of the target will be considered. The remaining electrons form an inert core [147].

The target atom Hamiltonian can be written in the form

$$H_{\rm t} = \sum_{i=1}^{N} H_i + \sum_{i<j}^{N} V_{ij}, \tag{3.1}$$

where H_i is the Hamiltonian of the inert-core+one-electron system, $N = 4l_0 + 2$ is the total number of electrons in the outer shell, V_{ij} is the Coulomb potential between the outermost p shell electrons.

We describe wave functions for the noble gases of Ne, Ar, Kr and Xe by a model of six p-electrons above an inert Hartree-Fock core. Excited states of noble gases are obtained by allowing one-electron excitations from the p shell. In what follows we consider a more general case of one-electron excitation from a closed-shell atom with the outer shell electron occupying an orbital with angular momentum l_0; with $l_0 = 1$ being the case for noble gases. This model is similar to the frozen-core model of helium and can be obtained by setting $l_0 = 0$ in the

present formulation. The helium frozen-core model has been used successfully in CCC calculations of electron [148], positron [135] and antiproton [136] scattering on He.

In order to implement this structure model (taking Ne as an example) we conduct calculations in a number of steps. First, we perform self-consistent Hartree-Fock calculations for the Ne^+ ion and obtain a set of orbitals: $1s, 2s, 2p$. We will refer to $1s$ and $2s$ orbitals as inert core orbitals and to the $2p$ orbital as the frozen-core orbital. We then produce a set of Laguerre functions (2.25). This set is used to diagonalise the quasi one-electron Hamiltonian of the Ne^{5+} ion,

$$H_i = K_i + V_i^{\rm HF}. \tag{3.2}$$

Here K_i is the kinetic energy operator and $V^{\rm HF}$ is a non-local Hartree-Fock potential that is constructed using inert core orbitals φ_c ($1s$ and $2s$ for Ne) according to

$$\begin{aligned} V^{\rm HF}\varphi(\boldsymbol{r}) &= -\frac{N}{r}\varphi(\boldsymbol{r}) + \sum_{\varphi_c}\left(\int d\boldsymbol{r}'\frac{|\varphi_c(\boldsymbol{r}')|^2}{|\boldsymbol{r}'-\boldsymbol{r}|} - \frac{1}{r}\right)\varphi(\boldsymbol{r}) \\ &\quad - \sum_{\varphi_c}\int d\boldsymbol{r}'\frac{\varphi_c(\boldsymbol{r}')\varphi(\boldsymbol{r}')}{|\boldsymbol{r}'-\boldsymbol{r}|}\varphi_c(\boldsymbol{r}). \end{aligned} \tag{3.3}$$

The result is a set $\{\varphi_\alpha\}$ of one-electron functions that satisfy

$$\langle\varphi_\alpha|H_i|\varphi_\beta\rangle = \epsilon_\alpha\delta_{\alpha,\beta}, \tag{3.4}$$

where $\delta_{\alpha,\beta}$ is Kronecker delta symbol and ϵ_α is the one-electron energy.

The $2p$ orbital in the $\{\varphi_\alpha\}$ basis differs substantially from the Hartree-Fock $2p$ orbital. In order to build a one-electron basis suitable for the description of a neutral Ne atom we replace the former orbital with the Hartree-Fock one. The basis is then orthogonalized by the Gram-Schmidt procedure. The resulting orthonormal basis is denoted $\{\phi_\alpha\}$ and satisfies

$$\langle\phi_\alpha|H_i|\phi_\beta\rangle = e_{\alpha,\beta}. \tag{3.5}$$

The coefficients $e_{\alpha,\beta}$ can be trivially obtained from the one-electron energies ϵ_α and overlap coefficients between the Hartree-Fock $2p$ orbital and the $\{\varphi_\alpha\}$ basis.

The target states $\{\Phi_n\}$ of Ne are described via the configuration-interaction (CI) expansion

$$\Phi_n = \sum_\alpha C_\alpha^n \, \tilde{\Phi}_\alpha. \tag{3.6}$$

The set of configurations $\{\tilde{\Phi}_\alpha\}$ is built by angular momentum coupling of the wave function of $2p^5$ electrons and one-electron functions from the $\{\phi_\alpha\}$ basis. We will refer to the former wave function as the frozen-core wave function $\psi_c(l_0^{4l+1})$, and to the latter one as the active electron wave function. The frozen-core wave function has angular momentum l_0 and spin 1/2, and when coupled with the active electron wave function ϕ_α leads to a configuration with spin $s = 0, 1$, orbital angular momentum l ($|l_\alpha - l_0| \leq l \leq l_\alpha + l_0$), and parity $\pi = (-1)^{l_0 + l_\alpha}$

$$|\tilde{\Phi}_\alpha\rangle = \mathcal{A} \, |l_0^{N-1} : l_0 \frac{1}{2}; l_\alpha : ls\pi\rangle, \tag{3.7}$$

where we used the fact that $N - 1 = 4l_0 + 1$. The antisymmetrisation operator $\mathcal{A}$ is given by

$$\mathcal{A} = \frac{1}{\sqrt{N}} \left(1 - \sum_{i=1}^{N-1} P_{iN} \right), \tag{3.8}$$

where P_{ij} is a permutation operator.

The coefficients C_α^n in the CI expansion Eq. (3.6) are obtained by diagonalisation of the Hamiltonian (3.1) in the basis of configurations (3.7). The target orbital angular momentum l, spin s, and parity π are conserved quantum numbers and diagonalisation of the target Hamiltonian is performed separately for each target symmetry $\{l, s, \pi\}$. The resulting set of target states satisfy

$$\langle \Phi_n | H_\mathrm{t} | \Phi_m \rangle = \delta_{n,m} \epsilon_n, \tag{3.9}$$

where ϵ_n is the target state energy. For antiproton scattering from the ground

state ($s = 0$) of a noble gas atom only target states with $s = 0$ can be excited. The size of the calculations can be increased by simply increasing the number of Laguerre functions (N_l). Low-lying states will converge to bound states of the target, while the remaining (pseudo) states will provide an increasingly accurate representation of the target atom high-lying bound states and an increasingly dense square-integrable representation of the target continuum.

3.3 Calculation of the effective potentials

In this section we describe how the matrix elements $\langle\Phi_n|V(t,\boldsymbol{r},\boldsymbol{b})|\Phi_m\rangle$ are calculated.

The projectile interaction with the target is written as

$$V = V_0 + \sum_{i=1}^{N} V_{0i}, \tag{3.10}$$

where V_0 is the interaction of the projectile with the inert core and V_{0i} with the target electrons. The potential V_0 is defined as

$$V_0(R) = -\frac{N}{R} + U_0(R), \tag{3.11}$$

where

$$U_0(R) = \sum_{\varphi_c} \left(-\frac{1}{R} + \int d\boldsymbol{r}' \frac{|\varphi_c(\boldsymbol{r}')|^2}{|\boldsymbol{r}' - \boldsymbol{R}|} \right), \tag{3.12}$$

and where φ_c are inert core orbitals. In the present work we calculated integrated cross sections which do not depend on V_0. Therefore, in the following we ignore this interaction. However, this potential will play an essential role when the method is applied to calculate differential cross sections.

As the first step we use the CI expansion (3.6) to express these matrix

elements via matrix elements for configurations $\{\tilde{\Phi}_\alpha\}$,

$$\langle\tilde{\Phi}_n|V(t,\boldsymbol{r},\boldsymbol{b})|\tilde{\Phi}_m\rangle = \sum_{\alpha\beta} C_\alpha^n C_\beta^m \langle\tilde{\Phi}_\alpha|V(t,\boldsymbol{r},\boldsymbol{b})|\tilde{\Phi}_\beta\rangle. \tag{3.13}$$

In order to perform the angular integration in (3.13) analytically we use the following multipole expansion of the potential

$$V = \sum_{i=1}^{N}\sum_{\lambda\mu} v_\lambda(R,r_i) Y^*_{\lambda\mu}(\widehat{\boldsymbol{R}}) Y_{\lambda\mu}(\widehat{\boldsymbol{r}}), \tag{3.14}$$

where

$$v_{\lambda\mu}(R,r_i) = -\frac{\min(R,r_i)^\lambda}{\max(R,r_i)^{\lambda+1}}. \tag{3.15}$$

With this and also using the properties of antisymmetric configurations (3.7) the final expression for the effective matrix elements for configurations $\{\Phi_\alpha\}$ can be written as

$$\begin{aligned}\langle\Phi_\alpha|V(t,\boldsymbol{r},\boldsymbol{b})|\Phi_\beta\rangle =& \sum_\lambda (-1)^{l_m} \frac{1}{\sqrt{2l_m+1}} Y^*_{\lambda\mu}(\widehat{\boldsymbol{R}}) C^{l_n m_n}_{l_m m_m \lambda\mu} \\ & \times (I_1(\alpha,\beta,\lambda,R) + I_2(\alpha,\beta,\lambda,R)),\end{aligned} \tag{3.16}$$

where

$$\begin{aligned}I_1(\alpha,\beta,\lambda,R) =& (-1)^{\lambda+l_0+l_\alpha+l_m}\sqrt{(2l_\beta+1)(2l_m+1)} C^{l_\alpha 0}_{l_\beta 0\lambda 0} C^{l_n m_n}_{l_m m_m \lambda\mu} \begin{Bmatrix} l_\beta & l_0 & l_m \\ l_n & \lambda & l_\alpha \end{Bmatrix} \\ & \times \int_0^\infty dr_c r_c^2 \varphi_c(r_c)\varphi_c(r_c) \int_0^\infty dr_a r_a^2 \phi_\alpha(r_a) V_\lambda(r_a,R)\phi_\beta(r_a),\end{aligned} \tag{3.17}$$

and

$$\begin{aligned}I_2(\alpha,\beta,\lambda,R) =& \delta_{l_\alpha l_\beta}\delta_{m_\alpha m_\beta}(-1)^{\lambda+l_\alpha+l_n+1}\sqrt{(2l_0+1)(2l_m+1)} C^{l_0 0}_{l_0 0\lambda 0} C^{l_n m_n}_{l_m m_m \lambda\mu} \\ & \times \begin{Bmatrix} l_0 & l_\alpha & l_m \\ l_n & \lambda & l_0 \end{Bmatrix} \int_0^\infty dr_a r_a^2 \phi_\alpha(r_a)\phi_\beta(r_a) \\ & \times \int_0^\infty dr_c r_c^2 \varphi_c(r_c) V_\lambda(r_c,R)\varphi_c(r_c),\end{aligned} \tag{3.18}$$

with $\boldsymbol{R}$, $\boldsymbol{r}_a$ and $\boldsymbol{r}_c$ being the position vectors of the incoming antiproton and the active and core electrons, respectively.

3.4 Calculations and results

3.4.1 Details of calculations

In this section we present the results of the calculations for antiproton scattering from Ne, Ar, Kr and Xe.

In general, as the targets become more complex (i.e. those with more electrons) the inclusion of the states with higher angular momentum is required to get converged results. Specifically, for Ne and Ar the maximum orbital quantum number $l_{\max}$ included were 3 and 5, respectively, while for Kr and Xe $l_{\max}$=9 was required. This resulted in the number of nl-states being 177, 226 and 377, respectively. Including magnetic quantum numbers the sizes of coupled differential equations for different targets are 803, 1276 and 3475, respectively.

One measure of the accuracy of the structure model we use in the CCC calculations is the comparison of calculated and experimentally observed ionisation energies. With aforementioned frozen-core expansions for Ne, Ar, Kr and Xe we obtain the ionisation energies of 20.57, 14.95, 13.38 and 11.73 eV which agree reasonably with the measured data of 21.56, 16.76, 14.00 and 12.13 eV, respectively.

Another measure of the target model accuracy is the calculated values of the static dipole polarizability of the target. These values proved to be somewhat larger than the experimentally observed values. This can potentially lead to an overestimation of the calculated cross sections. A simple way to deal with this problem is to introduce a model polarization potential that modifies the dipole term of the electron-electron and antiproton-electron Coulomb potentials. We refer to Ref. [147] for a more detailed discussion and note only that introduction of the model polarization potential allows us to fit calculated polarizability values

to the experimental values.

3.4.2 Results

The study of ionisation cross sections provides a strict test of the theory as it requires an accurate representation of all reaction channels and coupling between them. In Figures 3.1-3.4 we present our calculated total single-ionisation cross sections (TSICS) as a function of projectile energy ranging from 5 keV to 2 MeV.

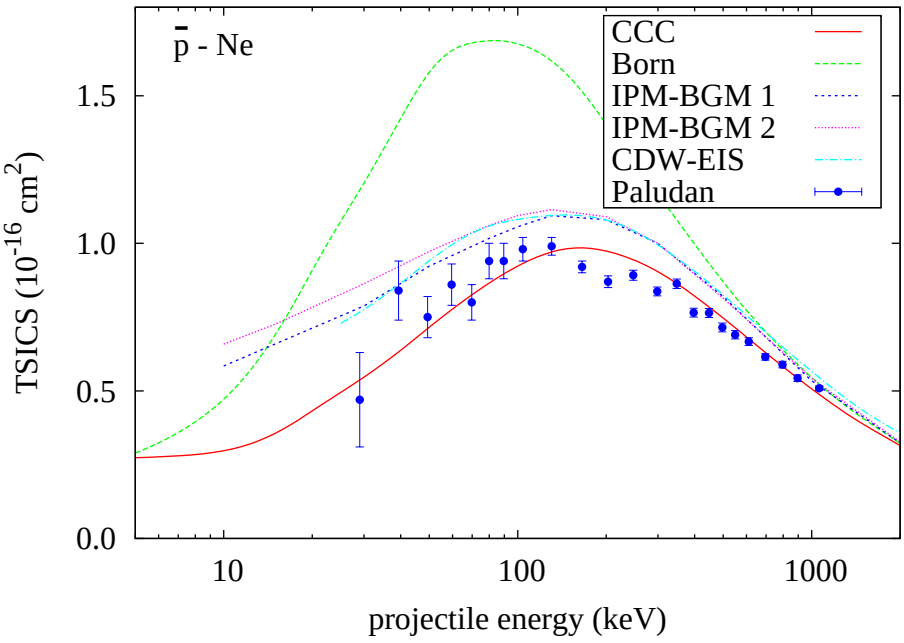

Figure 3.1: Integrated single-ionisation cross section for $\bar{p}-$Ne collisions. The present CCC and Born results are compared with the experimental measurements of Paludan *et al.* [141], independent-particle calculations of Kirchner *et al.* [144, 145] with "response" (IPM-BGM 1) and with "no response" (IPM-BGM 2), and CDW-EIS calculations of Montanari and Miraglia [146].

The CCC cross sections for antiproton-impact single-ionisation of Ne are presented in Figure 3.1 in comparison with the experiment and other calculations. As one can see the present CCC results are in excellent agreement with

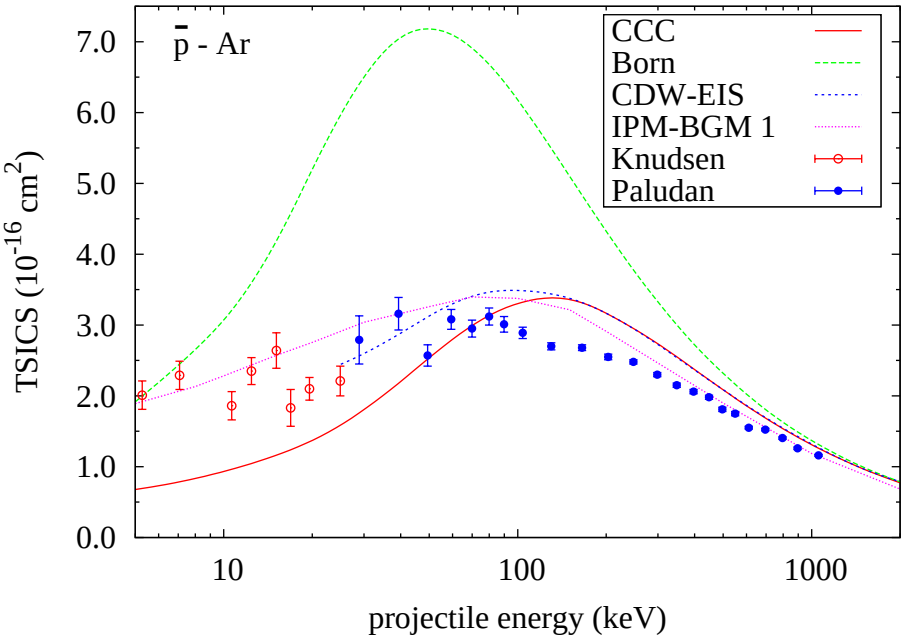

Figure 3.2: Integrated single ionisation cross section for $\bar{p}-$Ar collisions. Present CCC and Born results are compared with the experimental measurements of Paludan *et al.* [141] and Knudsen *et al.* [142]. Independent-particle calculations of Kirchner *et al.* [144, 145] with "response" (IPM-BGM 1) and CDW-EIS calculations of Montanari and Miraglia [146] are also shown.

the experiment at all energies where measurements are available. In this and the next figures we also show our first Born results to indicate the importance of the inter-channel coupling. For all considered targets we obtain the expected agreement between the Born results and the experiment at high projectile energies. Two types of independent particle model calculations of Kirchner *et al.* [144] and CDW-EIS calculations of Montanari and Miraglia [146] yield similar results which are slightly higher than the experiment. The disagreement systematically increases as the projectile energy decreases. The calculations of Kirchner *et al.* [144] where the time-dependent target screening was included slightly reduced the cross sections bringing them closer to the experimental data.

In Figure 3.2 we present our results for antiproton-impact single-ionisation

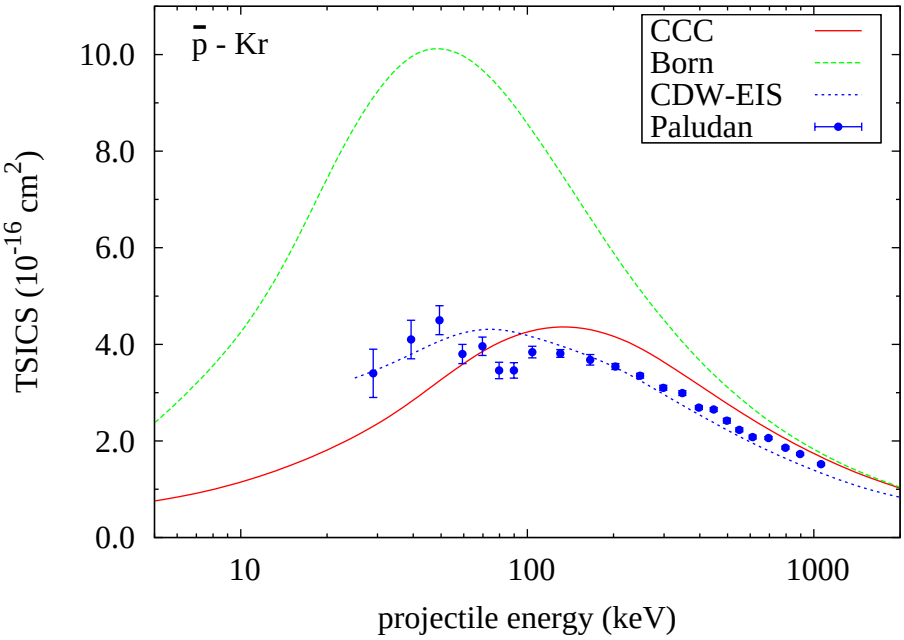

Figure 3.3: Integrated single ionisation cross section for $\bar{p}$−Kr collisions. Present CCC and Born results are compared with the experimental measurements of Paludan *et al.* [141] and CDW-EIS calculations of Montanari and Miraglia [146].

of Ar. At energies above 100 keV but below 1 MeV current results are slightly higher than the experiment and are in good agreement with CDW-EIS calculations of Montanari and Miraglia [146]. Below 50 keV they underestimate the experimental data of Paludan *et al.* [141] and Knudsen *et al.* [142]. The measurements for low-impact energies [142] match well with the previous ones by Paludan *et al.* [141] at higher energies. Independent particle model calculations of Kirchner *et al.* [144] where the time-dependent target screening is included better describe the experiment at all energies considered.

The results for ionisation of heavier elements by antiproton impact are shown in Figures 3.3 and 3.4. Our calculations for both Kr and Xe yield in general an agreement with the experiment of Paludan *et al.* [141] that is similar to Ar: at high energies calculated curves merge with the measured data; at intermediate

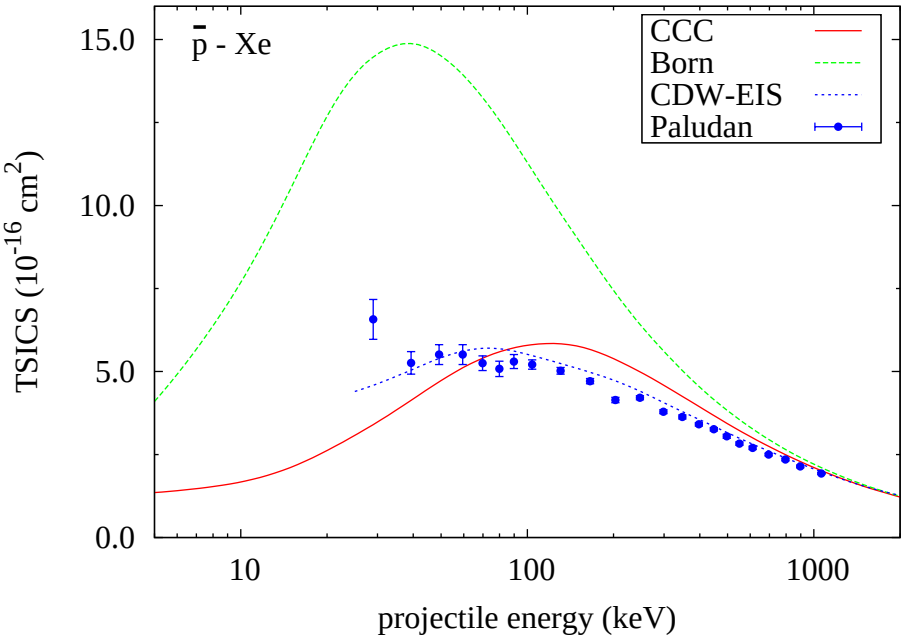

Figure 3.4: Integrated single ionisation cross section for $\bar{p}$−Xe collisions. Present CCC and Born results are compared with the experimental measurements of Paludan *et al.* [141] and CDW-EIS calculations of Montanari and Miraglia [146].

energy range from 90 keV to 600 keV they are slightly higher; below 60 keV calculated cross sections fall more rapidly as the impact energy decreases. The CDW-EIS calculations of Montanari and Miraglia [146] describe the experiment very well at all energies. Somewhat unexpectedly, for Kr and Xe the agreement between the CDW-EIS results and the experiment is better than for Ne and Ar while the target structure is more complicated.

3.5 Chapter summary

In this Chapter we have presented the results of the calculations for antiproton-impact single-ionisation of Ne, Ar, Kr and Xe using the time-dependent convergent close-coupling approach. For the description of Ne, Ar, Kr and Xe atom

wave functions we used a model of six p-shell electrons above an inert Hartree-Fock core with only one-electron excitations from the outer p shell allowed.

For all targets considered in the present work the expansion basis is obtained using the orthogonal Laguerre functions. Calculated single-ionisation cross sections for Ne, Ar, Kr and Xe are in good agreement with the experimental measurements. A common feature of the CCC cross sections for the noble gas targets is that they underestimate the experimental data below 100 keV and slightly overestimate them above this energy. Since we use the frozen-core approximation for the target structure, this is to be expected. Our previous calculations of antiproton-impact ionisation of He [136] where the target structure was treated using both frozen-core and multi-configuration approximations showed that the total ionisation cross sections obtained in the multi-configuration treatment were substantially higher at the lower energies (below 100 keV) than the frozen-core ones and slightly higher at the higher energies. This suggests that for a better agreement with experiment a proper multi-configurational treatment of the many-electron target is required. Finally, the agreement between our present results for the heavier noble-gas targets and experiment is slightly worse than for the lighter targets. This is likely because apart from the frozen-core approximation, heavier targets like Xe may require a relativistic treatment.

Chapter 4

Antiproton collisions with molecular targets

4.1 Introduction

Scattering of charged particles from molecules has become the subject of great theoretical and experimental interest. The clear understanding of antiproton interactions with atoms and molecules is important to the ALPHA collaboration at CERN that attempts to test the CPT invariance by forming and trapping antihydrogen [149] and study the gravitational behaviour of antimatter at rest [150–152]. Also, the upcoming Facility for Antiproton and Ion Research (FAIR) [1] at GSI requires the precise knowledge of the collision mechanism between antiproton and molecular hydrogen, since H_2 is expected to be one of the dominant residual-gas molecules.

Moreover, the interest to the processes occurring during the interactions of charged particles with biological matter has intensified due to their relevance to radiotherapy and oncology (see, e.g., Ref. [8, 153] and references therein). With the more and more regular use of ionising radiation in medicine, it is today necessary to assess the biological consequences of radiological examinations

particularly to know, with the highest degree of accuracy, the energy deposits induced by all the radiation commonly used in radiotherapy and even in medical imaging (light and heavy ions, electrons and positrons, X-rays and γ-rays). It is well known that the amount of water in a human body of average weight is 57% of the total body weight [154]. Hence, it is necessary to determine accurately the ionisation cross sections of water molecules in order to understand the inelastic processes induced by highly charged ions in biological matter.

From the fundamental aspect, the structure of molecular targets makes the underlying processes occur through mechanisms not observed for atomic targets. Indeed, the recent experiments for single nondissociative ionisation of molecular hydrogen by antiproton impact [155] have established that at very low energies the cross-section is suppressed and falls proportionally to the projectile velocity. This observation is in sharp contrast to the behaviours of the corresponding atomic cross-sections.

The antiproton-molecular hydrogen collision system is the simplest prototype of ion-molecule scattering due to the relative simplicity of the target and the absence of the electron capture channel. It is also the most convenient system to investigate molecular effects such as the influence of the vibrations and rotations of the molecule on the reaction dynamics. For this reason and also because of natural abundance of the target the antiproton scattering on molecular hydrogen is the most studied system both experimentally and theoretically. The cross sections for single nondissociative ionisation of molecular hydrogen have been measured on a wide energy range from 2.4 keV to 1.6 MeV [155–157]. From the theoretical side, in contrast to antiproton collisions with hydrogen [158] or helium [159] atoms, collisions with molecular hydrogen represent a greater challenge due to the existence of additional degrees of freedom. The lack of spherical symmetry, which stems from the multicentre nature of the target, represents an

additional challenge for both structure and subsequent scattering calculations. Available theoretical approaches to the problem [160–164] can be classified into two categories. First, there are studies that employ a one-electron approximation with the use of model spherical effective potentials for the description of the target [160, 161, 163]. These approaches reproduce a reasonably-accurate binding energy by tuning model parameters. Not surprisingly, these approaches are not sensitive to different molecular orientations. In addition, as the projectile energy decreases, these methods yield cross sections that fall-off slowly. This is contrary to the experimental observation. The other class of studies uses a more accurate description of H_2 where the contributions of electrons and nuclei of the molecular target are taken into account using the Born-Oppenheimer approximation [162–164]. These approaches obtain the orientationally averaged cross sections by averaging over only three orthogonal orientations. Calculations of [162] support the overall behaviour of the ionisation cross sections at low energies that was observed in the experiment, but, there still remains a significant discrepancy. The approach of Pindzola and coworkers [163, 164] yields results that agree with experiment at the two lowest calculated energies. However, at higher energies this approach produces cross sections that are too low.

Several models have been proposed to study the ionisation of water by proton impact. The plane-wave Born approximation (PWBA) with different molecular orbitals was used by Senger *et al.* [165, 166]. Actually, Senger *et al.* started from the well-known formula of Kuyatt and Jorgensen [167] for the ionisation of atomic hydrogen by proton impact and its extension to the other L and M subshells by Khandelwal and Merzbacher [168, 169] and Choi *et al.* [170]. Also, the authors applied the Salin factor [171] to account for the mechanism of electron transfer to the continuum. Olivera *et al.* [172] have used the continuum-distorted-wave-eikonal (CDW-EIS) approximation. In their treat-

ment the molecular orbitals were expressed by linear combinations of atomic orbitals of the constituents. The distortions due to the long-range Coulomb potential were introduced as multiplicative factors to the initial bound and final continuum states of the molecular target. It was then possible to take into account the two centre effects. Recently, Boudrioua *et al.* [173] have presented differential and total cross sections for the direct ionisation of water vapour by protons in the incident energy range 0.1 - 100 MeV. In their PWBA study the ground state of the target molecule was described by an accurate molecular wave function developed in terms of Slater-type-orbital functions, centred on the heaviest nucleus, i.e., the oxygen atom. This model had originally been proposed by Moccia [174]. Three different models differing by the choice of the final-state wave function were used. The first model introduced the interaction between the ejected electron and the residual target as in the PWBA. The second one included the scattered proton-ionised target interaction. And finally, the third one takes into account the pairwise interactions of the ionised target with the projectile and the ejected electron, and the attraction between the ejected electron and the scattered proton. The results of this sophisticated Born model are on overall in good agreement with experimental data. Very recently, Montanari and Miraglia [175] have developed a neonisation method to treat the molecules composed by hydrides of the second row of the periodic table of elements: CH_4, NH_3, H_2O, and HF. The method has been tested by calculating ionisation cross sections (total, single, and double differential), stopping power, energy-loss straggling, and mean excitation energy. The authors used CDW-EIS, the first-order Born, and the shellwise local plasma approximations. They showed that the neonisation model reproduces the various empirical values with high reliability in the intermediate- to high-energy region.

In this Chapter we present a semi-classical time-dependent CCC approach

to antiproton collisions with molecular targets: H_2, H_2^+ and H_2O. For H_2 and H_2^+, the method accounts for all possible orientations of the molecular target. Also, a technique that allows for calculating cross sections for proton production in antiproton-H_2 collisions by combining the ionisation cross section results for H_2 and H_2^+ targets will be described. For H_2O a neonisation method recently proposed by Montanari and Miraglia [175] will be used. This approach describes the ten-electron water molecule as a dressed Ne-like atom in a pseudospherical potential. A somewhat similarly effective spherically symmetric potential model was introduced by Lühr and Saenz [176] for the $\bar{p}$ + H_2 scattering problem.

4.2 Scattering equations

The treatment of antiproton collisions with molecular hydrogen or the hydrogen molecular ion requires solving a multicentre many-body Coulomb problem. In these molecular targets the electrons are exposed to the superposition of two potentials with centres at the locations of the target protons. This causes the electronic wave function to be symmetric around the molecular axis. Therefore, for the purpose of target structure calculations it is best to utilise the body frame coordinates with the origin between the two protons and the z' axis pointing in the molecular axis direction $\boldsymbol{d}$. The vector $\boldsymbol{d}$ can be chosen to be the position of any of the protons relative to the other one. At the same time the scattering equations have to be formulated in the laboratory frame with the z axis along the antiproton incident direction, since they directly lead to the experimental observables. The time-dependent, non-relativistic, Schrödinger equation of a many-body system consisting of the incident antiproton $\bar{p}$, two target protons, and one (H_2^+) or two (H_2) target electrons is

$$H\Psi = i\frac{\partial\Psi}{\partial t}, \tag{4.1}$$

where the total Hamiltonian $H = H_\mathrm{t} + V$ is the sum of the target Hamiltonian H_t and the Coulombic interaction between the projectile and the target V. The target Hamiltonian can be written as a sum of nuclear and electronic parts as

$$H_\mathrm{t} = H_\mathrm{nucl} + H_\mathrm{elec}. \tag{4.2}$$

Here the nuclear part is

$$H_\mathrm{nucl} = -\frac{1}{2M}\nabla^2_{\boldsymbol{R}_1} - \frac{1}{2M}\nabla^2_{\boldsymbol{R}_2} + \frac{1}{d} \tag{4.3}$$

with M being the mass of a proton. The electronic part is a function of position vectors of the nuclei ($\boldsymbol{R_n}$) and electrons ($\boldsymbol{r_i}$),

$$H_\mathrm{elec} = -\frac{1}{2}\sum_{i=1}^{N_\mathrm{e}} \nabla^2_{\boldsymbol{r_i}} - \sum_{n=1}^{2}\sum_{i=1}^{N_\mathrm{e}} \frac{1}{|\boldsymbol{r}_i - \boldsymbol{R}_n|} + \sum_{i=1}^{N_\mathrm{e}}\sum_{j>i}^{N_\mathrm{e}} \frac{1}{|\boldsymbol{r}_i - \boldsymbol{r}_j|}, \tag{4.4}$$

where $N_\mathrm{e} = 2$ for molecular hydrogen H_2 and 1 for the hydrogen molecular ion H_2^+. Finally, the interaction potential between the antiproton and the molecular target is

$$V = -\frac{1}{|\boldsymbol{R} - \boldsymbol{d}/2|} - \frac{1}{|\boldsymbol{R} + \boldsymbol{d}/2|} + \sum_{i=1}^{N_\mathrm{e}} \frac{1}{|\boldsymbol{R} - \boldsymbol{r}_i|}, \tag{4.5}$$

where $\boldsymbol{R}$ is the position vector of the antiproton in the laboratory frame, see Figure 4.1.

Solving the Schrödinger equation (4.1) with many degrees of freedom associated with nuclear and electronic motion of the target directly is extremely difficult. However, because of their much larger mass, the nuclei in a molecule move much slower than the electrons. This implies that the electrons can almost immediately adjust their positions to a changed nuclear configuration. In addition, we assume that the collision time is much shorter than the period of molecular oscillations. With these assumptions we can express the total wave

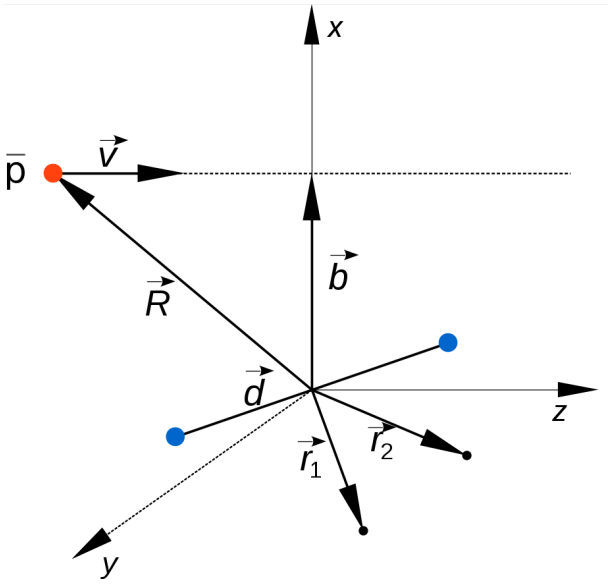

Figure 4.1: Sketch of the laboratory frame. The z axis is parallel to the incident antiproton direction.

function in a form where its parts dependent on the nuclear and electronic variables are separated, i.e.,

$$\Psi(t, \boldsymbol{r}, \boldsymbol{R}, \boldsymbol{d}) = \psi(t, \boldsymbol{r}, \boldsymbol{R})\chi_{\nu jm}(\boldsymbol{d}), \tag{4.6}$$

where $\chi_{\nu jm}(\boldsymbol{d}) = \tilde{\chi}_{\nu j}(d)Y_{jm}(\theta_d, \phi_d)$ are the molecular wave functions representing the dependence on the internuclear distance within the target and ψ is the electronic wave function. Here and elsewhere $\boldsymbol{r}$ collectively denotes the position vectors of all target electrons ($\boldsymbol{r} = \{\boldsymbol{r_1}, \boldsymbol{r_2}\}$ for H_2 and $\boldsymbol{r} = \{\boldsymbol{r_1}\}$ for H_2^+). Though the Eq. (4.6) assumes the constant internuclear distance within the target throughout the collision, we will later investigate the effect of molecular oscillations using the Franck-Condon principle [177]. With the total wave function defined this way we can first solve the electronic problem with fixed nuclei

$$(H_{\text{elec}} + V)\psi(t, \boldsymbol{r}, \boldsymbol{R}) = i\frac{\partial\psi(t, \boldsymbol{r}, \boldsymbol{R})}{\partial t}, \tag{4.7}$$

and then use the solution that depends parametrically on the nuclear coordinates

to restore the total wave function Ψ. The wave functions and corresponding energies for the rovibrational motion of the molecular target, $\chi_{\nu jm}(\boldsymbol{d})$ and $E^{\rm nucl}_{\nu j}$, can be found from the following equation that also stems from Eq. (4.1):

$$(H_{\rm nucl} + E^{\rm elec}_f)\chi_{\nu jm}(\boldsymbol{d}) = E^{\rm nucl}_{\nu j}\chi_{\nu jm}(\boldsymbol{d}), \tag{4.8}$$

where $E^{\rm elec}_f$ is the total electronic energy of the final target state.

In this work we neglect the rotational degrees of freedom of the molecular target and consider the total wave function as

$$\Psi(t, \boldsymbol{r}, \boldsymbol{R}, \boldsymbol{d}) = \frac{1}{\sqrt{4\pi}}\psi(t, \boldsymbol{r}, \boldsymbol{R})\tilde{\chi}_{\nu 00}(d) \equiv \psi(t, \boldsymbol{r}, \boldsymbol{R})\tilde{\chi}_{\nu}(d), \tag{4.9}$$

where ν is the vibrational quantum number.

Following the ideas of the convergent close-coupling method, details of which are given in Chapter 2, we expand the electronic scattering wave function in terms of a certain set of N target pseudostates Φ_f according to

$$\psi(t, \boldsymbol{r}, \boldsymbol{R} = \boldsymbol{b} + \boldsymbol{v}t, \boldsymbol{d}) = \sum_{f=1}^{N} A_f(t, \boldsymbol{b}, \boldsymbol{d})\Phi_f(\boldsymbol{r}, \boldsymbol{d})e^{-i\epsilon_f t}, \tag{4.10}$$

where ϵ_f is the energy of the target electronic state f. The expansion coefficients $A_f(t, \boldsymbol{b}, \boldsymbol{d})$ define the probability for transitions into electronic bound and continuum states.

With this representation of the total scattering wave function the semiclassical Schrödinger equation can be transformed into a set of coupled-channel differential equations for the time-dependent coefficients $A_f(t, \boldsymbol{b}, \boldsymbol{d})$,

$$i\frac{dA_f(t, \boldsymbol{b}, \boldsymbol{d})}{dt} = \sum_{j=1}^{N} A_j(t, \boldsymbol{b}, \boldsymbol{d})\langle\Phi_f|V(t, \boldsymbol{r}, \boldsymbol{b}, \boldsymbol{d})|\Phi_j\rangle e^{i(\epsilon_f - \epsilon_j)t}, \quad f = 1, \ldots, N. \tag{4.11}$$

Eq. (4.11) is solved with the initial conditions $A_f(t_0 = -\infty, \boldsymbol{b}, \boldsymbol{d}) = \delta_{f0}$, as the target is initially in the ground state Φ_0.

In contrast to atomic targets, which are spherically symmetric, for collisions with molecular targets solving just one set of coupled equations (4.11) is not sufficient. Here calculations for all molecular orientations have to be carried out in order to find orientationally averaged transition probabilities. A straightforward approach to solving Eq. (4.11) for all molecular orientations is computationally expensive. Therefore, in previous studies that accounted for the multicentre nature of H_2 the calculations were limited to only three orthogonal molecular orientations [162–164]. As far as the $\bar{p}+H_2^+$ system is concerned, Sakimoto [178] accounted for 11×5 orientations for (θ_d, ϕ_d). Later, Lühr and Saenz [179] compared their results obtained using only three orthogonal orientations with the results of Sakimoto [178], and found good agreement. They concluded that averaging over the three orientations was adequate for $\bar{p} + H_2^+$. Whether this is the case for $\bar{p}-H_2$ collisions as well, remains to be seen. To this end we have developed an alternative approach. Before giving details of the approach we need to describe how the target structure is treated.

4.3 Target description for molecular hydrogen and the hydrogen molecular ion

As indicated above the target structure calculations are performed in the body frame (BF) coordinates that are denoted with primed variables (Figure 4.2). For the description of the H_2 electronic functions a single-centre configuration-interaction (CI) expansion around the midpoint of the internuclear axis is used:

$$\Phi_f^{\mathrm{BF}}(\boldsymbol{r}_1', \boldsymbol{r}_2', d) = \sum_{\alpha\beta} B_{\alpha\beta}^f(d)\phi_\alpha(\boldsymbol{r}_1')\phi_\beta(\boldsymbol{r}_2'). \tag{4.12}$$

One-electron orbitals ϕ_α are defined as

$$\phi_\alpha(\boldsymbol{r}) = \frac{\xi_{kl_\alpha}^{(\lambda_{l_\alpha})}(r)}{r} Y_{l_\alpha m_\alpha}(\theta, \phi), \tag{4.13}$$

where $Y_{l_\alpha m_\alpha}(\theta, \phi)$ are the spherical harmonics. One-electron functions $\xi_{kl}(r)$ are constructed using Laguerre polynomials as

$$\xi_{kl}^{(\lambda_l)}(r) = \sqrt{\frac{\lambda_l r(k-1)!}{2(k+l)(k+2l)!}}(\lambda_l r)^{l+1} \exp\left(-\frac{\lambda_l r}{2}\right) L_{k-1}^{2l+1}(\lambda_l r), \tag{4.14}$$

where k ranges from 1 to the basis size N_l. The choice of the exponential fall-off parameter λ_l will be discussed later. The expansion coefficients $B_{\alpha\beta}^{f}$ and target energy levels ϵ_f are found by diagonalising the target Hamiltonian $H_{\rm t}$. Presently, for the purpose of describing single ionisation of H_2, we restrict the upper limit of one of the indices in Eq. (4.12) in order to prevent the inner electron from ejecting. Specifically, we include only one-electron $\{1s, 2s, 2p, 3s, 3p, 3d\}$ orbitals for the description of the inner electron excitations. The other index representing the one-electron states of the outer electron can be as large as required to ensure converged results.

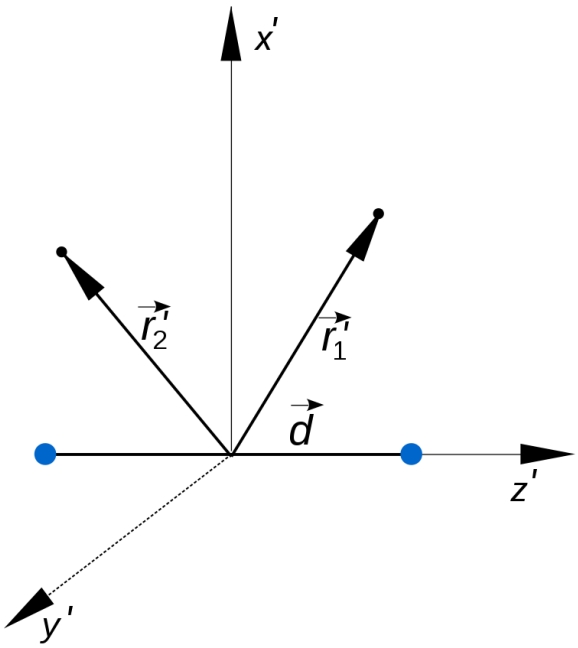

Figure 4.2: Sketch of the body frame. The z' axis is parallel to the internuclear axis of the target.

For the one-electron target, H_2^+, the electronic functions have a simpler form:

$$\Phi_f^{\mathrm{BF}}(\boldsymbol{r_1'}, d) = \sum_{\alpha} B_\alpha^f \phi_\alpha(\boldsymbol{r_1'}). \tag{4.15}$$

Laboratory-frame electronic pseudostates $\Phi_f(\boldsymbol{r}, \boldsymbol{d})$ can be generated from the body-frame pseudostates (4.12) and (4.15) by rotating the latter into laboratory frame $\Phi_f(\boldsymbol{r}, \boldsymbol{d}) = \hat{D}\Phi_f^{\mathrm{BF}}(\boldsymbol{r}, d)$, where $\hat{D}$ is the rotation operator. In the following section we derive the matrix elements $\langle\Phi_f|V(t, \boldsymbol{r}, \boldsymbol{b}, \boldsymbol{d})|\Phi_i\rangle$ for both $\bar{p}$–H_2 and $\bar{p}$–H_2^+ collision processes.

The CI expansion given by (4.12) has been commonly used to describe the hydrogen molecule structure [162, 180]. The CI states should represent a number of bound states of H_2 accurately, and the accuracy of the ground state energy in most cases is used to determine the quality of this expansion. With this type of expansion one can expect to represent a molecule of any size. However, the number of functions required may increase drastically. Therefore, it is hard to estimate up to which size of the molecule the CI expansion will be applicable. The accuracy of the ground state and the number of CI functions used in the current calculations will be discussed later.

4.4 Matrix elements

Straightforward, laboratory-frame calculations of $\langle\Phi_f|V(t, \boldsymbol{r}, \boldsymbol{b}, \boldsymbol{d})|\Phi_i\rangle$ are computationally expensive, since the available body-frame target pseudostates first need to be converted into the laboratory frame before taking integrals. However, if we factor out the molecular-orientation-dependent part from the interaction potential (4.5), it will become irrelevant to what coordinate frame is used for taking the integrals over the configuration space of the electrons. The validity of the technique has been confirmed by obtaining exactly the same results as in the

laboratory-frame calculations. The technique allows us to use the pseudostates defined in the body-frame.

For $\bar{p}-H_2$ collisions the matrix elements $\langle\Phi_f|V(t,\boldsymbol{r}_1,\boldsymbol{r}_2,\boldsymbol{b},\boldsymbol{d})|\Phi_i\rangle$ can be written as

$$\langle\Phi_f|V(t,\boldsymbol{r}_1,\boldsymbol{r}_2,\boldsymbol{b},\boldsymbol{d})|\Phi_i\rangle = \int d\boldsymbol{r}_1' d\boldsymbol{r}_2' \Phi_f^{\mathrm{BF}*}(\boldsymbol{r}_1',\boldsymbol{r}_2',d)\left(-\frac{1}{|\boldsymbol{R}-\boldsymbol{d}/2|}-\frac{1}{|\boldsymbol{R}+\boldsymbol{d}/2|}\right.$$
$$\left.+\frac{1}{|\boldsymbol{R}-\boldsymbol{r}_1|}+\frac{1}{|\boldsymbol{R}-\boldsymbol{r}_2|}\right)\Phi_i^{\mathrm{BF}}(\boldsymbol{r_1'},\boldsymbol{r_2'},d), \qquad (4.16)$$

where primed coordinates are relative to the body frame. Integration of the part corresponding to the interaction of the projectile with the target nuclei, which we denote by I_1, is straightforward due to the orthogonality of the target pseudostates and gives

$$\begin{aligned} I_1 &= \int d\boldsymbol{r}_1'\ d\boldsymbol{r}_2'\ \Phi_f^{\mathrm{BF}*}(\boldsymbol{r}_1',\boldsymbol{r}_2',d)\left(-\frac{1}{|\boldsymbol{R}-\boldsymbol{d}/2|}-\frac{1}{|\boldsymbol{R}+\boldsymbol{d}/2|}\right)\Phi_i^{\mathrm{BF}}(\boldsymbol{r}_1',\boldsymbol{r}_2',d) \\ &= -\delta_{fi}\left(\frac{1}{|\boldsymbol{R}-\boldsymbol{d}/2|}+\frac{1}{|\boldsymbol{R}+\boldsymbol{d}/2|}\right). \end{aligned} \qquad (4.17)$$

However, the remaining part, denoted by I_2, is more challenging and involves partial-wave decomposition. By considering the symmetry with respect to interchanging $\boldsymbol{r}_1$ and $\boldsymbol{r}_2$ we can rewrite it as

$$\begin{aligned} I_2 =& 2\int d\boldsymbol{r}_1'\ d\boldsymbol{r}_2'\ \Phi_f^{\mathrm{BF}*}(\boldsymbol{r}_1',\boldsymbol{r}_2',d)\frac{1}{|\boldsymbol{R}-\boldsymbol{r}_1|}\Phi_i^{\mathrm{BF}}(\boldsymbol{r}_1',\boldsymbol{r}_2',d) \\ =& 8\pi\sum_{\lambda\mu}\frac{1}{2\lambda+1}Y_{\lambda\mu}^*(\widehat{\boldsymbol{R}}) \\ & \times\int d\boldsymbol{r}_1' d\boldsymbol{r}_2' \Phi_f^{\mathrm{BF}*}(\boldsymbol{r}_1',\boldsymbol{r}_2',d)\Phi_i^{\mathrm{BF}}(\boldsymbol{r}_1',\boldsymbol{r}_2',d)v_\lambda(R,r_1)Y_{\lambda\mu}(\widehat{\boldsymbol{r}}_1), \end{aligned} \qquad (4.18)$$

where

$$v_\lambda(R,r_1) = \begin{cases} \frac{R^\lambda}{r_1^{\lambda+1}} & \text{if } R<r_1, \\ \frac{r_1^\lambda}{R^{\lambda+1}} & \text{otherwise.} \end{cases} \qquad (4.19)$$

With the target pseudostates defined as in Eq. (4.12) this term becomes

$$I_2 = 8\pi \sum_{\lambda\mu} \sum_{\alpha\beta\gamma\delta} \frac{1}{2\lambda+1} B^f_{\alpha\beta} B^i_{\gamma\delta} Y^*_{\lambda\mu}(\widehat{\boldsymbol{R}}) \langle \phi_\beta | \phi_\delta \rangle \int_0^\infty dr_1 \; \xi_{n_\alpha l_\alpha}(r_1) \xi_{n_\gamma l_\gamma}(r_1) v_\lambda(R, r_1) \times \int d\widehat{\boldsymbol{r}}'_1 \; Y^*_{l_\alpha m_\alpha}(\widehat{\boldsymbol{r}}'_1) Y_{l_\gamma m_\gamma}(\widehat{\boldsymbol{r}}'_1) Y_{\lambda\mu}(\widehat{\boldsymbol{r}}_1). \tag{4.20}$$

In order to perform the angular integration in Eq. (4.20), the coordinate $\boldsymbol{r}_1$ originating from the partial wave decomposition of the potential must be transformed to the body frame. $Y_{\lambda\mu}(\widehat{\boldsymbol{r}}_1)$ in the body frame becomes

$$Y_{\lambda\mu}(\widehat{\boldsymbol{r}}_1) = \sum_m Y_{\lambda m}(\widehat{\boldsymbol{r}}'_1) D^{\lambda *}_{\mu m}(\phi_d, \theta_d, 0), \tag{4.21}$$

where $D^{\lambda *}_{\mu m}(\phi_d, \theta_d, 0)$ is the usual Wigner rotation matrix with ϕ_d and θ_d being the azimuthal and polar angles of the internuclear axis $\boldsymbol{d}$. We finally obtain

$$I_2 = 4\sqrt{\pi} \sum_{\lambda\mu} D^{\lambda *}_{\mu m_\alpha - m_\gamma}(\phi_d, \theta_d, 0) Y^*_{\lambda\mu}(\widehat{\boldsymbol{R}}) \sum_{\alpha\beta\gamma\delta} B^f_{\alpha\beta} B^i_{\gamma\delta} \sqrt{\frac{2l_\gamma + 1}{(2\lambda+1)(2l_\alpha+1)}} \times C^{l_\alpha 0}_{l_\gamma 0 \lambda 0} C^{l_\alpha m_\alpha}_{l_\gamma m_\gamma \lambda m_\alpha - m_\gamma} \langle \phi_\beta | \phi_\delta \rangle \int_0^\infty dr_1 \; \xi_{n_\alpha l_\alpha}(r_1) \xi_{n_\gamma l_\gamma}(r_1) v_\lambda(R, r_1), \tag{4.22}$$

with $C^{LM}_{\lambda\mu sq}$ denoting the Clebsch-Gordan coefficients [137].

In order to combine this term with the term corresponding to the interaction of the projectile with the target nuclei, we also expand the Eq. (4.17) into partial waves as

$$\begin{aligned} \frac{1}{|\boldsymbol{R} - \boldsymbol{d}/2|} + \frac{1}{|\boldsymbol{R} + \boldsymbol{d}/2|} &= 8\pi \sum_{\lambda\mu} \frac{\mathrm{mod}(\lambda, 2)}{2\lambda+1} v_\lambda(R, d/2) Y^*_{\lambda\mu}(\widehat{\boldsymbol{R}}) Y_{\lambda\mu}(\widehat{\boldsymbol{d}}) \\ &= 4\sqrt{\pi} \sum_{\lambda\mu} D^{\lambda *}_{\mu 0}(\phi_d, \theta_d, 0) Y^*_{\lambda\mu}(\widehat{\boldsymbol{R}}) \frac{\mathrm{mod}(\lambda, 2)}{\sqrt{2\lambda+1}} v_\lambda(R, d/2), \end{aligned} \tag{4.23}$$

where $v_\lambda(R, d/2)$ is defined by Eq. (4.19). Finally, using Eqs. (4.16), (4.22) and (4.23) we can write the matrix elements in the following form

$$\langle \Phi_f | V(t, \boldsymbol{r}_1, \boldsymbol{r}_2, \boldsymbol{b}, \boldsymbol{d}) | \Phi_i \rangle = \sum_{\lambda\mu} \mathcal{V}^{fi}_{\lambda\mu}(t, b, d) D^{\lambda *}_{\mu, m_f - m_i}(\phi_d, \theta_d, 0), \tag{4.24}$$

where the molecular orientation-independent parts $\mathcal{V}^{fi}_{\lambda\mu}(t,b,d)$ are defined as

$$\mathcal{V}^{fi}_{\lambda\mu}(t,b,d) = \frac{4\sqrt{\pi}Y^*_{\lambda\mu}(\widehat{\boldsymbol{R}})}{\sqrt{2\lambda+1}}\Big[-\delta_{fi}\mathrm{mod}(\lambda,2)v_\lambda\left(R,d/2\right) + \sum_{\alpha\beta\gamma\delta} B^f_{\alpha\beta}B^i_{\gamma\delta}\sqrt{\frac{2l_\gamma+1}{2l_\alpha+1}} \times C^{l_\alpha 0}_{l_\gamma 0\lambda 0}C^{l_\alpha m_\alpha}_{l_\gamma m_\gamma \lambda m}\langle\phi_\beta|\phi_\delta\rangle \int_0^\infty dr_1\ \xi_{n_\alpha l_\alpha}(r_1)\xi_{n_\gamma l_\gamma}(r_1)v_\lambda(R,r_1)\Big]. \tag{4.25}$$

Expressing the interaction matrix elements in this form is important and will help to eliminate the molecular orientation dependence from the scattering equations.

Antiproton collisions with the hydrogen molecular ion, H_2^+, are also modelled by the same equation (4.11). However, in this case the matrix elements should be calculated using the H_2^+ pseudostates and the appropriate interaction potential. Following similar steps the matrix elements for the $\bar{p}$+H_2^+ collision can be shown to have the same form as Eq. (4.24). For this process the reduced matrix elements, independent of the molecular orientation, can be written as

$$\mathcal{V}^{fi}_{\lambda\mu}(t,b,d) = \frac{4\sqrt{\pi}Y^*_{\lambda\mu}(\widehat{\boldsymbol{R}})}{\sqrt{2\lambda+1}}\Big[-\delta_{fi}\mathrm{mod}(\lambda,2)v_\lambda\left(R,d/2\right) + \frac{1}{2}\sum_{\alpha\beta} B^f_{\alpha}B^i_{\beta}\sqrt{\frac{2l_\beta+1}{2l_\alpha+1}}C^{l_\alpha 0}_{l_\beta 0\lambda 0}C^{l_\alpha m_\alpha}_{l_\beta m_\beta \lambda m} \times \int_0^\infty dr\ \xi_{n_\alpha l_\alpha}(r_1)\xi_{n_\beta l_\beta}(r_1)v_\lambda(R,r_1)\Big]. \tag{4.26}$$

4.5 Equation for the molecular orientation-independent part of the scattering amplitude

We express the time-dependent coefficients in Eq. (4.11) in a form similar to (4.24) according to

$$A_f(t,\boldsymbol{b},\boldsymbol{d}) = \sum_{\lambda\mu}\mathcal{A}^f_{\lambda\mu}(t,b,d)D^{\lambda*}_{\mu,m_f}(\phi_d,\theta_d,0), \tag{4.27}$$

where $\mathcal{A}^f_{\lambda\mu}(t,b,d)$ are the probability amplitudes independent of the molecular orientation. The expansion indices are limited by the maximum allowed total orbital angular momentum.

We substitute expansions (4.24) and (4.27) into Eq. (4.11) and, using the following identities for the Wigner functions

$$\begin{aligned}\int_0^{2\pi} d\phi \int_0^{\pi} d\theta \sin\theta D^{J_2*}_{M_2M_2'}(\phi_d,\theta_d,0) D^{J_1*}_{M_1M_1'}(\phi_d,\theta_d,0) =& \frac{4\pi^2}{2J_2+1}\delta_{J_1J_2}\delta_{M_1M_2}\delta_{M_1'M_2'},\\ \int_0^{2\pi} d\phi \int_0^{\pi} d\theta \sin\theta D^{J_3*}_{M_3M_3'}(\phi_d,\theta_d,0) D^{J_2}_{M_2M_2'}(\phi_d,\theta_d,0) D^{J_1*}_{M_1M_1'}(\phi_d,\theta_d,0)&\\ =\frac{4\pi^2}{2J_3+1} C^{J_3M_3}_{J_1M_1J_2M_2} C^{J_3M_3'}_{J_1M_1'J_2M_2'},&\end{aligned} \tag{4.28}$$

derive a set of coupled differential equations for the molecular-orientation-independent parts of the scattering amplitudes $\mathcal{A}^f_{\lambda\mu}(t,b,d)$:

$$\begin{aligned} i\frac{d\mathcal{A}^f_{\lambda\mu}(t,b,d)}{dt} =& \sum_{j=1}^{N} e^{i(\epsilon_f-\epsilon_j)t} \sum_{LM} \mathcal{A}^j_{LM}(t,b,d)\\ &\times \sum_{sq} \frac{2\lambda+1}{2L+1} C^{LM}_{\lambda\mu sq} C^{Lm_j}_{\lambda m_f s m_j - m_f} \mathcal{V}^{fj}_{sq}(t,b,d), \quad f=1,\ldots,N. \end{aligned} \tag{4.29}$$

This set of equations is solved subject to the initial conditions $\mathcal{A}^f_{\lambda\mu}(t_0=-\infty,b,d) = \delta_{f0}\delta_{\lambda0}\delta_{\mu0}$. This boundary condition also implies that at infinite distance the antiproton does not feel the anisotropic nature of the molecular target.

4.6 Calculation of cross sections

Let us first consider antiproton collisions with molecular hydrogen. Cross sections for excitation and ionisation are written in terms of the probabilities for the corresponding transitions between the initial and final states of H_2. Those probabilities can be calculated via corresponding transition amplitudes, which

are the overlap between the total wave function at $t = +\infty$ and the final state of the target

$$f_{f0}(\boldsymbol{b}) = \frac{1}{\sqrt{4\pi}} \int d\boldsymbol{d}\ d\boldsymbol{r_1}\ d\boldsymbol{r_2}\ \psi^*(\boldsymbol{r_1}, \boldsymbol{r_2}, t, \boldsymbol{d})\Big|_{t=+\infty} \tilde{\chi}_0^*(d)\Phi_f(\boldsymbol{r_1}, \boldsymbol{r_2}, \boldsymbol{d})\tilde{\chi}_\nu^{\mathrm{r}}(d). \tag{4.30}$$

Here, $\tilde{\chi}_0(d)$ describes the first vibrational level in the ground electronic state of the H_2 molecule, whereas $\tilde{\chi}_\nu^{\mathrm{r}}(d)$ describes the residual H_2^+ ion, in the vibrational state ν of the particular electronic state f. The factor $1/\sqrt{4\pi}$ is the normalisation coefficient coming from molecular orientation averaging. The calculation of the integrals (4.30) is computationally expensive, since it involves generating a new set of pseudostates and solving the electronic problem for many internuclear distances d. For the collision processes of interest, however, the dependence on d is weak and almost linear as indicated in [178]. Therefore, it is possible to expand the electronic part of the integrand, $\psi^*(\boldsymbol{r_1}, \boldsymbol{r_2}, t, \boldsymbol{d})\Big|_{t=+\infty} \Phi_f(\boldsymbol{r_1}, \boldsymbol{r_2}, \boldsymbol{d})$, into a Taylor series around the equilibrium distance d_0 and use only the first term $\psi^*(\boldsymbol{r_1}, \boldsymbol{r_2}, t, \boldsymbol{d_0})\Big|_{t=+\infty} \Phi_f(\boldsymbol{r_1}, \boldsymbol{r_2}, \boldsymbol{d_0})$. With this we can factor out the integration over d and write Eq. (4.30) in the following form:

$$\begin{aligned} f_{f0}(\boldsymbol{b}) \approx & \frac{1}{\sqrt{4\pi}} \int \mathrm{d}d\ d^2\tilde{\chi}_0^*(d)\tilde{\chi}_\nu^{\mathrm{r}}(d) \\ & \times \int_0^{2\pi} \mathrm{d}\varphi_d\ \mathrm{d}\theta_d\ \mathrm{d}\boldsymbol{r_1}\ \mathrm{d}\boldsymbol{r_2}\ \sin\theta_d\ \psi^*(\boldsymbol{r_1}, \boldsymbol{r_2}, t, \boldsymbol{d_0})\Big|_{t=+\infty} \\ & \times \Phi_f(\boldsymbol{r_1}, \boldsymbol{r_2}, \boldsymbol{d_0}). \end{aligned} \tag{4.31}$$

Given the orthogonality properties of the target electronic states the transition probabilities, which are the square of the absolute transition amplitudes, can be written as a product of two factors as

$$P_{f0}(\boldsymbol{b}) = \frac{1}{4\pi} \left| \int_0^\infty \mathrm{d}d\ d^2\tilde{\chi}_0^*(d)\tilde{\chi}_\nu^{\mathrm{r}}(d) \right|^2 \int_0^\infty \mathrm{d}\varphi_d\ \mathrm{d}\theta_d\ \sin\theta_d\ A_f(t, \boldsymbol{b}, \boldsymbol{d_0})\Big|_{t=+\infty}^2. \tag{4.32}$$

The first factor $\left|\int_0^\infty \mathrm{d}d\ d^2\tilde{\chi}_0^*(d)\tilde{\chi}_\nu^{\mathrm{r}}(d)\right|^2$, also known as the Franck-Condon (FC) factor, carries information on probabilities for transitions between the vibra-

tional levels in one electronic state and vibrational levels in any other electronic states of the molecule. Since we mainly concentrate on single ionisation of H_2 in the present work, we will need a list of the FC factors for transitions between the first vibrational level in the ground state of the H_2 molecule and all possible vibrational levels in the ground state of the residual ion H_2^+. For this purpose we use the database of the FC factors for molecule-ion reactions of H_2 calculated by Wünderlich and Fantz [181] and Hunter *et al.* [182].

With this the total single ionisation cross section independent of the molecular axis of the target is

$$\begin{aligned}\sigma_{\rm ion}^{\nu} &= \sum_{f\in[\epsilon_f\geq 0]} \int \mathrm{d}\boldsymbol{b} P_{f0}(\boldsymbol{b}) \\ &= \left| \int_0^\infty \mathrm{d}d\ d^2 \tilde{\chi}_0^*(d) \tilde{\chi}_\nu^{\rm r}(d) \right|^2 \\ &\quad \times \sum_{f\in[\epsilon_f\geq 0]} \sum_{\lambda\mu} \frac{2\pi}{2\lambda+1} \int_0^\infty db\ b \left| \mathcal{A}_{\lambda\mu}^f(t,b,d_0) \Big|_{t=+\infty} \right|^2 . \end{aligned} \tag{4.33}$$

This cross section describes single ionisation of H_2 where the residual ion H_2^+ in the ground electronic state is in the ν-th vibrational level. At this point, if we are not concerned about the state of the residual ion and concentrate purely on the event of single ionisation of the molecular target, we can sum up the ionisation cross sections for all vibrational levels corresponding to both bound and continuum vibrational states. Since

$$\sum_\nu \left| \int_0^\infty \mathrm{d}d\ d^2 \tilde{\chi}_0^*(d) \tilde{\chi}_\nu^{\rm r}(d) \right|^2 = 1, \tag{4.34}$$

the single ionisation cross section can simply be calculated as

$$\sigma_{\rm ion} = \sum_{f\in[\epsilon_f\geq 0]} \sum_{\lambda\mu} \frac{2\pi}{2\lambda+1} \int_0^\infty db\ b \left| \mathcal{A}_{\lambda\mu}^f(t,b,d_0) \Big|_{t=+\infty} \right|^2 . \tag{4.35}$$

However, experimental data for single ionisation of H_2 by antiproton impact are available only for the process where the residual H_2^+ ion stays bound. In other

words, the experiment does not account for processes where the residual ion breaks apart into two protons before reaching the detector. Therefore, to take into account the possible experimental uncertainties we can use the following formula:

$$\sigma_{\rm ion}^{\rm exp} = \sum_{\nu\in[\epsilon_\nu<0]} \left| \int_0^\infty {\rm d}d\ d^2\tilde{\chi}_0^*(d)\tilde{\chi}_\nu^{\rm r}(d) \right|^2 \sigma_{\rm ion}, \tag{4.36}$$

where the summation is done over the negative energy ($\epsilon_\nu < 0$) vibrational levels.

Similarly, not being concerned about the fate of the residual ion, we can write the single ionisation cross section, which is differential in the angular coordinates of the molecular axis, as

$$\sigma_{\rm ion}(\theta_d,\phi_d) = \sum_{f\in[\epsilon_f\geq 0]} \int {\rm d}\boldsymbol{b} \left| A_f(t,\boldsymbol{b},\boldsymbol{d_0})\Big|_{t=+\infty} \right|^2. \tag{4.37}$$

The consistency of the results for orientation-dependent cross sections calculated from solving Eq. (4.29) with those obtained from the direct solution of Eq. (4.11) has been checked.

For antiproton collisions with H_2^+ orientationally averaged and orientation-dependent cross sections are calculated the same way as in Eqs. (4.35, 4.37), but using the scattering amplitudes, $\mathcal{A}^f_{\lambda\mu}(t,b,d_0)\Big|_{t=+\infty}$ and $A_f(t,\boldsymbol{b},\boldsymbol{d_0})\Big|_{t=+\infty}$ calculated for the $\bar{p}$–H_2^+ collision system. For the H_2^+ target we do not consider the influence of molecular oscillations and calculate the cross sections only in a fixed-nuclear approximation.

4.7 Proton production in antiproton collisions with H_2

Measurements of cross sections for proton production in antiproton collisions with H_2 were performed almost two decades ago [183]. However, the only theoretical work available so far significantly underestimates the experimental data [179]. Let us consider mechanisms in $\bar{p}-H_2$ collisions that may lead to the production of protons. First, the double-electron ionisation of the target results in the production of two protons. Second, the incident antiproton can ionise the molecular target, leaving the residual ion H_2^+ in (electronic) excited states that may further dissociate into atomic hydrogen and a proton. In the present work we use the so-called independent-event model (IEV) [126, 184]. In this model all of the residual ions dissociate, since H_2^+ with the internuclear distance of H_2 ($d = 1.4$ a.u.) does not support any bound state. Thus, summing cross sections for processes that produce protons we can write

$$\sigma_{H^+} = 2\sigma_{\rm di} + \sigma_{\rm ie}, \tag{4.38}$$

where $\sigma_{\rm di}$ and $\sigma_{\rm ie}$ are the cross sections for double ionisation and ionisation with excitation, respectively.

To calculate these processes we follow the idea suggested in [185] and implemented in [179]. We implement the IEV model within the current time-dependent CCC method. In the IEV model the double ionisation is considered as a two-step process. In the first and second steps single ionisation of H_2 and H_2^+ occur, respectively. Hence the total double ionisation probability should be equal to the product of the probabilities for these single ionisation processes:

$$\sigma_{\rm di} = 2\pi \int_0^\infty {\rm d}b\; b P_{\rm ion}^{H_2}(b) P_{\rm ion}^{H_2+}(b). \tag{4.39}$$

Similarly, the cross section for ionisation with excitation can be expressed as:

$$\sigma_{\rm ie} = 2\pi \int_0^\infty {\rm d}b\; b P_{\rm ion}^{\rm H_2}(b) P_{\rm exc}^{\rm H_2+}(b). \tag{4.40}$$

It should be noted that in calculating probabilities for H_2^+ the internuclear distance of the target is taken the same as for H_2, i.e. $d_0 = 1.4$ a.u, since the events are happening at the same time. Clearly, calculating cross sections this way neglects any interference between the two effects. However, this appears to be a good approximation for calculations of double ionisation in $\bar{p}$-He collisions [185].

4.8 Antiproton scattering on the water molecule

The structure of the water molecule is treated using a "neonisation" idea proposed in [175]. According to the idea the water molecule is described as a dressed pseudo-spherical atom. Following [175] the multi-centre nuclei Coulomb potential of H_2O is approximated with the following spherical potential:

$$V_{H_2O} = -\frac{8}{r} - \frac{2(1-\varepsilon)\Theta(R_H - r)}{R_H} - \frac{2(1-\varepsilon e^{1-r/R_H})\Theta(r - R_H)}{r}, \tag{4.41}$$

where R_H is the distance between the oxygen atom and either of two hydrogen atoms, Θ is the Heaviside step function and ε is introduced to account for the deviation of the target potential from spherical symmetry. With a multi-centre problem now reduced to a central one, we can apply the technique described in Chapter 3 to find energy levels and wave functions. This requires replacing the electron-nuclei term N/r in Eq. (3.2) with the potential (4.41). In addition, the $1s$, $2s$, and $2p$ core wave functions for the Ne atom are replaced by corresponding core wave functions for the water molecule. The latter are taken from the Slater basis representation presented in [175]. Finally, the parameter ε of the potential (4.41) is varied to match the experimentally measured value for the

ground state energy of the target. As a result the spectrum of the H_2O molecule is represented by the same model as we have used for Ne: six p-electrons above the inert Hartree-Fock core with only one-electron excitations allowed from the closed p shell.

4.9 Details of calculations

The calculations for the H_2 target presented below have been performed with $Z \equiv vt$ from -100 to $+100$ a.u. at all energies. In constructing the target basis we have included all H_2 target states with the maximum value of angular momentum projection $m_{\max}$ equal to $l_{\max}$. To improve the accuracy of the calculations the Laguerre $1s$ orbital was replaced with the H_2^+ $1s\sigma_g$ orbital, which was obtained via diagonalisation of the H_2^+ Hamiltonian in the same Laguerre basis. The full set of anti-symmetric two-electron configurations comprises two separate sets. The frozen-core $(1s, nlm)$ configurations, where one electron is limited to the $1s$ orbital of the H_2^+ ion, while the other occupies any of the Laguerre orbitals (nlm). The other set takes all possible $(n'l'm', nlm)$ configurations with principle quantum numbers of Laguerre orbitals n' and $n \leq 3$. The frozen-core configurations allow for a square-integrable representation of the target continuum and coupling to the ionisation channels in the scattering calculations. The primary reason for including the $(n'l'm', nlm)$ configurations is to increase the accuracy in accounting for electron-electron correlations in the ground and low-lying excited states.

The accuracy of the final results for the orientationally-averaged ionisation cross section has been checked by performing calculations with several structure models that differ in the value of maximum orbital angular momentum $l_{\max}$ and number of one-electron Laguerre functions $N_l = n_{\max} - l$. The convergence

studies have been carried out in the entire energy region considered in this work. We give typical examples at the projectile energies 5, 50 and 100 keV, i.e. at the position of the maximum in the experimentally measured total single ionisation cross section (see below) and at some distance from the maximum on both sides.

First, we fix the basis parameter $n_{\max}$ at some large value and systematically increase the parameter $l_{\max}$ starting from 0. Table 4.1 illustrates the convergence pattern of the total single ionisation cross section (TSICS) with increasing $l_{\max}$, while $n_{\max} = 20$ for each symmetry. One can see that at all considered energies convergence to within 0.2% is observed at $l_{\max} = 4$. Next, we check whether $n_{\max} = 20$ is sufficiently large in terms of the convergence of the cross section as a function of the principal quantum number of included states.

Table 4.1: Convergence of the total single ionisation cross section with increasing $l_{\max}$ when $n_{\max} = 20$.

Energy (keV)	l=0	l=1	l=2	l=3	l=4
10	0.7762	0.1274	1.177	1.174	1.176
50	0.3924	1.559	1.653	1.653	1.653
100	0.2313	1.293	1.437	1.488	1.489

In Table 4.2, we examine the convergence of the TSICS with $n_{\max}$ by setting $l_{\max} = 4$. The convergence in the cross section when $n_{\max}$ changes from 5 to 20 is within 5%. A similar rate of convergence has been achieved across the entire energy range with the target model consisting of 674 states, where $l_{\max} = 4$, $N_l = 20 - l$, and a Laguerre basis exponential fall-off parameter $\lambda_l = 2$. The ground-state energy obtained with this basis is -1.16497 a.u., which compares well with the accurate value of -1.1745 [186]. We have also checked the consistency of the calculations obtained using the present code with the previous fully quantum-mechanical results for the helium target [136], by taking the internuclear separation to zero (i.e., considering He as the united

atom limit of H_2) and exactly reproduced results of [136].

For the calculations of $\bar{p}$–H_2^+ collisions with the target internuclear distances $d_0 = 1.4$ and 2.0 a.u. we use the basis with the same parameters. Because of the relative simplicity of H_2^+ compared to H_2, the number of molecular target states is reduced to 430.

Due to the partial-wave decomposition the dimension of the set of differential equations for the molecular-orientation-independent coefficients (4.29) is equal to the number of target channels multiplied by the number of partial waves representing the molecular target state. Thus, with $l_{\max} = 4$ these numbers for H_2 and H_2^+ are 81554 and 52030, respectively.

Table 4.2: Convergence of the TSICS with increasing $n_{\max}$ when $l_{\max} = 4$.

Energy (keV)	n=5	n=10	n=15	n=20
10	0.6382	1.154	1.156	1.146
50	1.281	1.793	1.664	1.662
100	1.130	1.627	1.469	1.479

For H_2O we use the basis set that was generated for Ne, except that the states of the basis are obtained by diagonalisation of the target Hamiltonian containing the Hartree-Fock potential representing the water molecule as a dressed pseudo-spherical atom. The 2p-subshell ionisation energy in our calculations is the same as the experimentally measured value of 12.6 eV since in our model this energy was used as the empirical parameter to generate the target structure. As have been discussed in Chapter 3, the inclusion of $l_{\max} = 3$ (which results in the number of nlm-states being 806) was sufficient to get the converged results.

4.10 Results of calculations

4.10.1 $\bar{p}-H_2$ collisions

In [187] the energy dependence of the total cross section for single non-dissociative ionisation in $\bar{p}-H_2$ collisions was presented. The CCC results obtained using analytical averaging over all molecular orientations produced excellent agreement with experiment across the whole range of energies except for a small region from 20 to 90 keV. Here we study the quality of approximate averaging that is obtained from a limited number of molecular orientations. This knowledge could be useful in the treatment of molecular collisions where the analytical averaging is not possible. We consider three perpendicular directions, $(\theta_d, \phi_d) = (0, 0)$, $(\pi/2, 0)$ and $(\pi/2, \pi/2)$, as used by Lühr and Saenz [162] and Lee *et al.* [164]. In addition, we consider two other intermediate orientations $(\theta_\mathrm{d}, \phi_\mathrm{d}) = (\pi/4, 0)$ and $(-\pi/4, 0)$. The energy dependence of the total ionisation cross sections for these five orientations is presented in Figure 4.3. One can see that the curves differ considerably for different orientations. As the projectile energy increases above 100 keV the results for molecular orientations lying on the plane with $\phi_\mathrm{d} = 0$ converge to the same value. At lower energies there is considerable variation in the energy dependence of the cross sections. Compared to the results for other displayed orientations, cross sections for the molecular orientation $(\pi/2, \pi/2)$, which is perpendicular to the $\phi_\mathrm{d} = 0$ plane are significantly larger at lower calculated energies and significantly smaller above 20 keV. A similar situation is observed in the calculations of Lühr and Saenz [179] for antiproton-impact ionisation of H_2^+. The results for the $(\pi/2, \pi/2)$ orientation are significantly different from the results for the other two, $(0, 0)$ and $(\pi/2, 0)$, orientations.

We present in Figure 4.4 the energy dependence of our single ionisation cross sections averaged using two techniques together with the experimental measure-

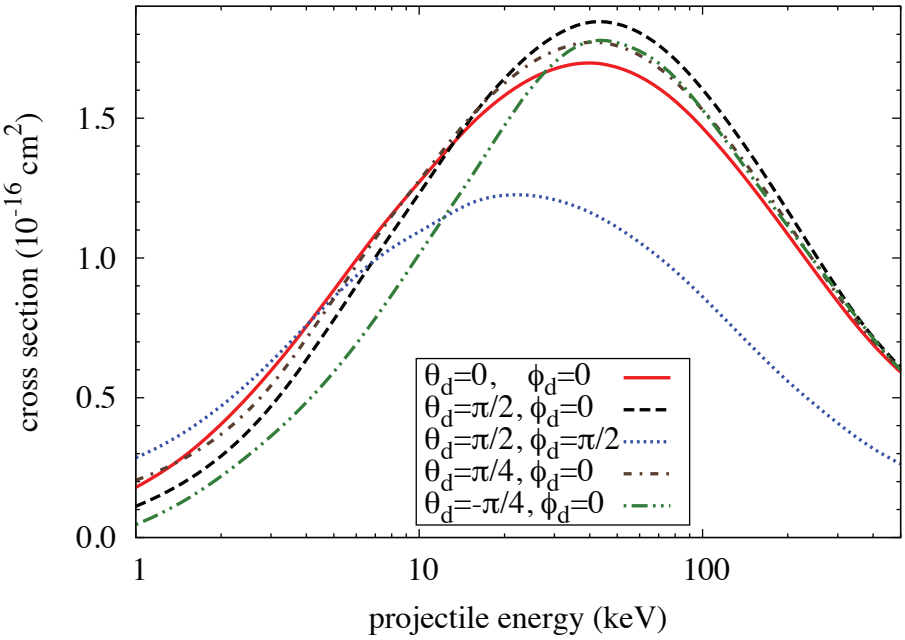

Figure 4.3: The total cross section for single ionisation of H_2 by antiprotons for different molecular orientations.

ments [155–157] and the two-electron calculations of Lühr and Saenz [162] and Lee *et al.* [164] obtained using three orthogonal molecular orientations. The results of Lühr and Saenz [162], being in excellent agreement with experiment at high energies clearly overestimates it at energies below 20 keV, whereas the results of Lee *et al.* [164] are generally lower and agree with experiment only at lower calculated energies. It should be noted that the calculations of Lee *et al.* [164] are for single ionisation of the target with allowance for excited H_2^+ states. Their calculations without account of excited H_2^+ states (not shown) produced even smaller cross sections. Interestingly, our present results obtained from three orthogonal molecular orientations disagree with other calculations based on the three-orientation approximation. At the same time the present three-orientation results slightly overestimate our analytically averaged results at low energies, and significantly underestimate them at energies above 20 keV. In order to check whether the present results with approximate averaging come closer

to the analytical results with increasing number of included molecular orientations we have considered two more intermediate orientations ($(\theta_d, \phi_d) = (\pi/4, 0)$ and $(-\pi/4, 0)$). The averaged results over five orientations indeed are closer to the analytical results. As seen in Figure 4.4 the difference between the analytical results and the results based on the three-orientation approximation can be as large as 20% at some energies. This suggests that the typical inclusion of only three orthogonal molecular orientations is not sufficient and an accurate method of orientation averaging is important. The present analytical averaging technique has certainly improved the agreement with experiment.

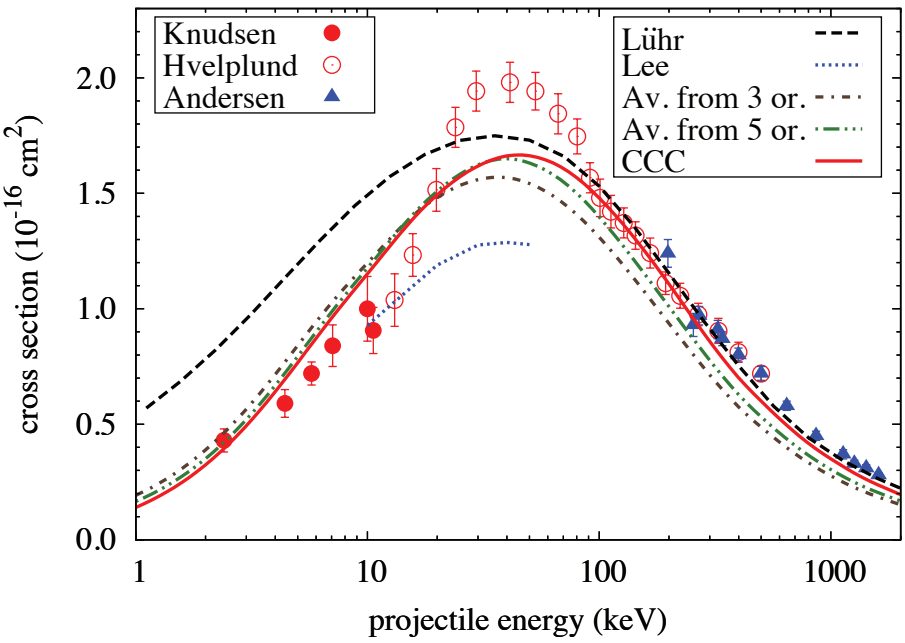

Figure 4.4: The total cross section for single ionisation of H_2 by antiprotons. Present CCC results obtained using various averaging techniques are compared with the experimental data of Andersen *et al.* [156], *et al.* Hvelplund [157], and Knudsen *et al.* [155], and two-electron calculations of Lee *et al.* [164] and Lühr and Saenz [162].

The discrepancy between theory and experiment in the energy region around 50 keV still remains, and it is not likely to be related to the method of orientation

averaging. As indicated in the previous section, after single nondissociative ionisation, the residual ions of H_2^+ can dissociate before they reach the detector, provided they are in the vibrational continuum states. Therefore, to evaluate the cross section that was measured in the experiment we have to use the Eq. (4.36), which contains the Franck-Condon estimates for transitions from the ground vibrational level of H_2 into all the negative energy vibrational levels of H_2^+. The Franck-Condon factors were obtained from the database provided by Wünderlich and Fantz [181] and Hunter *et al.* [182]. The modified results are 1.7% lower than the results shown in Figure 4.4. This way we find that at most 1.7% of the residual H_2^+ ions may dissociate before reaching the detector. A similar estimate gives 0.5% for the D_2^+ ions used in the experiment. Thus, possible excitation of the vibrational continuum has little effect on our results.

4.10.2 $\bar{p}-\mathbf{H}_2^+$ collisions

In Figure 4.5 the present Franck-Condon results for total ionisation obtained by analytical molecular-orientation-averaging are compared to the corresponding results of Sakimoto [178] obtained from 11×5 orientations and those by Lühr and Saenz [179] obtained using only three orientations. While the previous two calculations [178, 179] are in good agreement with each other, the present results are slightly lower at low energies and slightly higher at the energies where the cross section has a maximum. Overall, the disagreement between the present results and the results of Lühr and Saenz [179] is surprisingly small in comparison with the disagreement observed for the molecular hydrogen target (Figure 4.4). This observation is counterintuitive. The hydrogen molecular ion, H_2^+, with the equilibrium internuclear distance ($d_0 = 2.0$ a.u.) larger than that of the neutral molecule, H_2 ($d_0 = 1.4$ a.u.), exhibits larger deviation from the spherical symmetry. Consequently, using only three molecular orientations for the purpose

of calculating the orientationally averaged cross section for antiproton-impact ionisation of H_2^+ should have produced results that are in larger disagreement with the present analytically averaged results. This, however, is not the case.

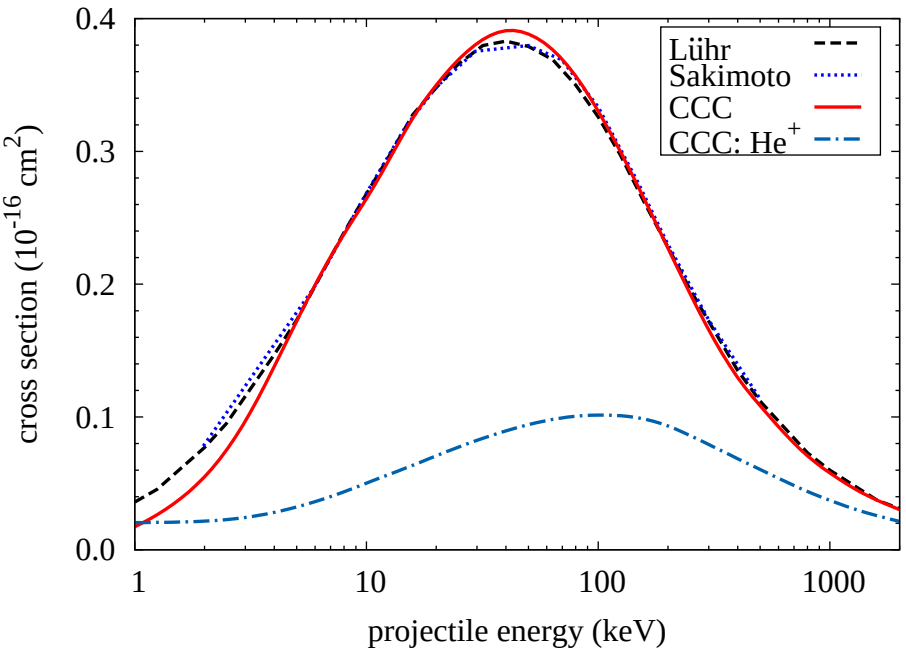

Figure 4.5: The total cross section for single ionisation of H_2^+ by antiprotons. Present CCC results are compared with the two-centre molecular-target calculations of Lühr and Saenz [179] and Sakimoto [178]. CCC results for the He^+ target are also presented.

In Figure 4.5 we also present our results for antiproton-impact ionisation of He^+ which is the united atom limit of H_2^+. One can see that the ionisation cross section for He^+ has a maximum near 100 keV and slowly falls with decreasing impact energy, practically becoming flat at the lowest calculated energies. At all presented energies the cross section for ionisation of He^+ is significantly less than the cross section for ionisation of H_2^+ due to the large difference in the binding energies. One can see strong suppression of the H_2^+ cross section at low energies. The reason for this is the same as in the molecular hydrogen case [187]. In order to see this point we have calculated the electron cloud distribution of the H_2^+

target during the collision. The snapshots shown in Figure 4.6 reveal that the suppression mechanism is indeed the same, however the electron movement from one target proton to another under the influence of the incoming antiproton is more pronounced than in the case of antiproton collisions with molecular hydrogen. This is related to the fact that the distance between the protons in the H_2^+ ion is larger than the corresponding distance within the H_2 molecule. In other words, when the antiproton is close to one of the protons in H_2^+, the electron has a chance to be bound to the other proton which is more isolated from Coulomb fields of the antiproton and the first proton.

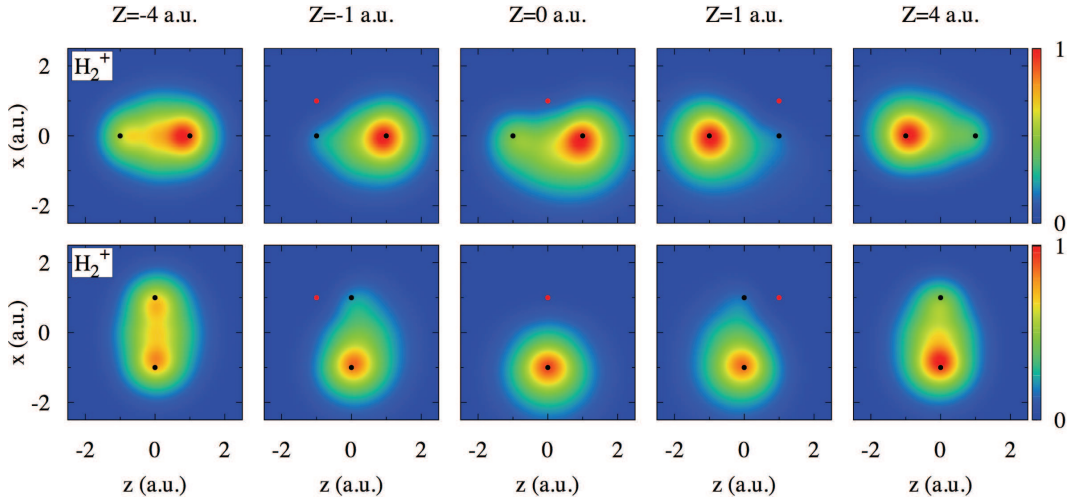

Figure 4.6: The electron distribution dynamics in antiproton collisions with H_2^+ at 1 keV. The snapshots are taken at the impact parameter $b = 1$ a.u. and several representative values of $Z = vt$. The corresponding projectile position is shown by red dots. The target nuclei are shown by black dots.

4.10.3 H^+ production in $\bar{p}-H_2$ collisions

In Figure 4.7 the present CCC results for $\sigma_{\rm di}$, $\sigma_{\rm ie}$, and σ_{H^+} are compared with the experimental data of Hvelplund *et al.* [157]. Also shown are the corresponding cross sections calculated by Lühr and Saenz [179]. In spite of the two-step approximation the present results agree reasonably well with experiment above

40 keV. Below 40 keV our results are systematically higher than experiment, indicating that the IEV model becomes less reliable at low energies. Also, it is worth mentioning that the mechanism of H^+ production due to ionisation with excitation contributes more than twice compared to double ionisation.

The results of Lühr and Saenz [179] are systematically lower than experiment at all available energies. The individual cross sections for double ionisation and ionisation with excitation of the target are also systematically lower than the corresponding present results. We emphasize that Lühr and Saenz [179] performed σ_{H^+} calculations using an internuclear distance d_0=2.0 a.u. for H_2^+ and 1.4478 a.u. for H_2, despite the fact that the two-step approximation requires using the same internuclear distance d_0=1.4478 a.u. for both targets. They indicated that similar calculations with d_0=1.4478 a.u. for H_2^+ produced even lower cross sections.

4.10.4 $\bar{p}$-H_2O collisions

Finally, Figure 4.8 exhibits the present calculations for single ionisation of H_2O by antiproton impact. At this stage there are no experimental measurements available for antiproton scattering on the water molecule. However, as we mentioned earlier such experiments are planned for near future.

At this stage it is worth emphasizing that most methods used to treat ion-water molecule scattering are essentially perturbative. These are different Born treatments [165, 166, 173] and CDW-EIS approaches [172, 188] valid for relatively high collision energies. The target description plays an important role in such calculations as has recently been analysed by Champion and co-workers [189]. In our current treatment, following neonisation idea of Montanari and Miraglia [175], ten-electron water molecule has been described as a dressed Ne-like

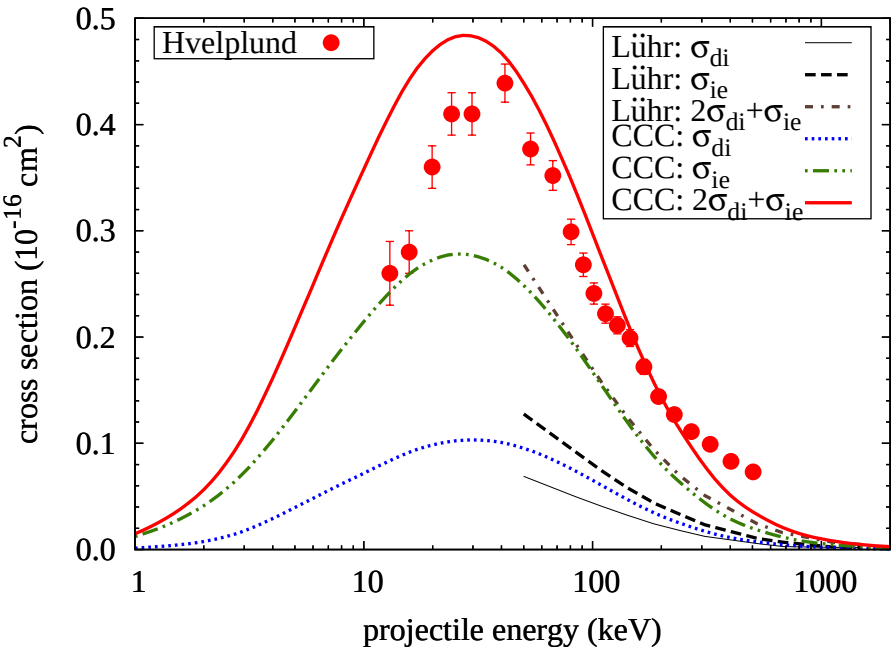

Figure 4.7: Cross sections leading for production of H^+ in antiproton collisions with H_2. Present CCC results obtained within the two-step approximation are compared with the experimental data of Hvelplund *et al.* [157] and calculations of Lühr and Saenz [179].

atom in a pseudospherical potential. As a result H_2O molecule is represented by the same model as we have used for Ne (detailed description of which is given in Chapter 3): six p-electrons above the inert Hartree-Fock core with only one-electron excitations allowed from the closed p shell. We expect that the current close-coupling approach with such a multi-electron target structure should produce reliable results at energies down to 1 keV. From this viewpoint it should provide guidance to future experiments.

4.11 Chapter summary

In this Chapter we have investigated the collisions of antiprotons with molecular targets using a time-dependent convergent close-coupling approach.

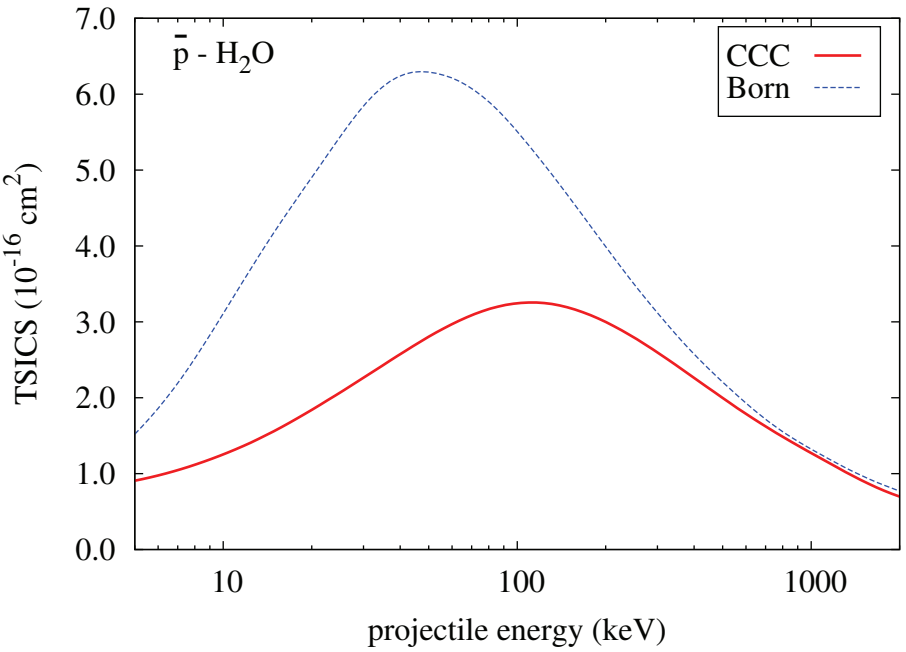

Figure 4.8: Integrated single ionisation cross section for $\bar{p}-H_2O$ collisions. The present CCC and Born results are shown.

For H_2 we presented an approach that accounts for *all* possible orientations of the molecular target by analytically averaging over the molecular orientations. A new set of scattering equations that are independent of the molecular orientation has been derived. A similar technique can be implemented in studies of projectile collisions with other molecular targets. The presented approach is valid at all energies, and significantly improves the agreement between theory and experiment for $\bar{p} - H_2$ single ionisation cross sections. The strong suppression of the single ionisation cross section at low energies has been shown to be attributed solely to the structure of the molecular target. Studies of the time evolution of the electron cloud distribution during the antiproton collisions with atomic and molecular hydrogen showed that the electron, which would have gone into the continuum in the atomic hydrogen case, gets caught by one of the target protons in the molecular hydrogen case. A small region near the experimental maximum, where a discrepancy is observed needs further attention from both

theorists and experimentalists.

In addition, to complete the picture of the full target breakup, the cross sections for ionisation with excitation, double ionisation, and proton production in antiproton-molecular hydrogen collisions have been calculated using a two-step approximation. Good agreement with experiment for proton production was found above 40 keV. Apparently, the two-step approximation employed in the calculations is problematic at lower energies. A more accurate treatment of the two-electron processes is yet to be developed.

The approach has been extended to study antiproton-impact ionisation of another homonuclear diatomic molecule, H_2^+. Except for minor discrepancies the present results with analytical orientational averaging are in good agreement with previous studies that used only three orthogonal orientations of the H_2^+ target.

For antiproton scattering on H_2O we applied our approach given in Chapter 3 for multi-electron inert-gas atoms. The water molecule was modelled as dressed atoms in a pseudo-spherical potential. It is worthwhile to stress that most theoretical calculations are based on Born and continuum-distorted-wave approximations. Hence, we expect the current close-coupling method to $\bar{p}$+H_2O will be more reliable in the intermediate collision energies.

Chapter 5

Two-centre time-dependent convergent close-coupling method

5.1 Introduction

Since the original works of Bates [68, 69] two-centre coupled channel methods have been significantly developed. In this development the proton-hydrogen collision system has served as a prototype. The first application of the method was carried out by McCarroll [70] using a two-state approximation and it gave good results for capture to the ground state. Wilets and Gallaher [71] performed calculations including eigenstates with the maximum principal quantum number $n = 2$ and $n = 3$. The authors for the first time utilised molecular symmetry properties of the proton-hydrogen collision system. The other significance of their work was the implementation of the so-called invaluable check, which is basically a unitarity conservation rule. Rapp and Dinwiddie [76] provided the expressions for the exchange matrix elements as one-dimensional integrals involving eigenstates with the principal quantum number up to $n = 3$. Cheshire [74] developed an alternative differential equation based method to evaluate

two-centre integrals.

To improve the basis further, it was necessary in some way to include the effect of continuum states. The first attempt was done by Cheshire *et al.* [72]. They considered excitation and charge transfer between $1s$, $2s$, and $2p$ levels in p-H($1s$) collisions and retained these particular eigenfunctions in order to represent well the states of interest at infinite separation. Pseudostates were chosen to have high overlap with the low-lying state of the united atom He^+. They argued that such inclusion of pseudostates should lead to a more rapid convergence. The results of Cheshire *et al.* [72] were in good agreement with the experiments. Later, Shakeshaft [78] attempted at computing the total ionisation cross sections at intermediate impact energies. He employed a two-centre expansion using the Sturmian functions. At the ionisation maximum, Shakeshaft's calculations were about 20% below the cross sections from experiments. Further two-centre calculations by Kuang and Lin [50] showed very good agreement with the experiment of Shah *et al.* [104, 190]. However, the detailed study of Toshima [89] established that the previous close-coupling results were not converged. But at E=50 keV the total ionisation cross section by Toshima [89] now was almost 30% higher than the experiment. It is interesting to note from the experimental perspective that the recent studies by Kerby *et al.* [191], focusing on the doubly differential cross section for ejected electrons in the p-H system, gave substantially different total ionisation cross sections than by Shah *et al.* [104, 190].

Despite the fact that the two-centre close-coupling approaches are the most reliable techniques, there are some problems with the present approaches. These are oscillatory structures observed in the calculations of Shakeshaft [72], Slim and Ermolaev [83] and Kuang and Lin [50]. There have been several efforts to overcome these issues. For example, Kuang and Lin [50] proposed to use asymmetric two-centre expansions. But this approach was unable to provide reliable

excitation and capture cross section at the same time. On the other hand, the basis generator method (BGM) [98] and finite Hilbert basis set (FHBS) [192] treatments are believed to better represent the dynamical properties of an ion-atom collision.

The discrepancies between the theory and experiment as well as the differences among various theoretical approaches warrant development of better theories. These can be the development of new models or further development of well-established approaches. In this Chapter a new time-dependent two-centre convergent close-coupling method will be introduced.

5.2 Coupled equations

We consider the collision process of a proton with the hydrogen atom. Jacobi coordinates for the system is shown in Figure 5.1. Target and projectile are labelled by A and B. The position of the target with respect to the centre of mass of the projectile nucleus-electron bound system is denoted by $\boldsymbol{\rho}$, while $\boldsymbol{\sigma}$ is the position of the projectile with respect to the target nucleus-electron system. $\boldsymbol{R}$ represents the position vector of the projectile relative to the target.

The total Schrödinger equation for the system is

$$H\Psi = E\Psi, \tag{5.1}$$

with Hamiltonian

$$H = T + V, \tag{5.2}$$

where T and V are the kinetic and potential energy operators,

$$T = -\frac{1}{2\mu}\nabla^2_{\boldsymbol{\sigma}} - \frac{1}{2}\nabla^2_{\boldsymbol{r}_A} \equiv -\frac{1}{2\mu}\nabla^2_{\boldsymbol{\rho}} - \frac{1}{2}\nabla^2_{\boldsymbol{r}_B}, \tag{5.3}$$

$$V = \frac{1}{R} - \frac{1}{r_A} - \frac{1}{r_B}, \tag{5.4}$$

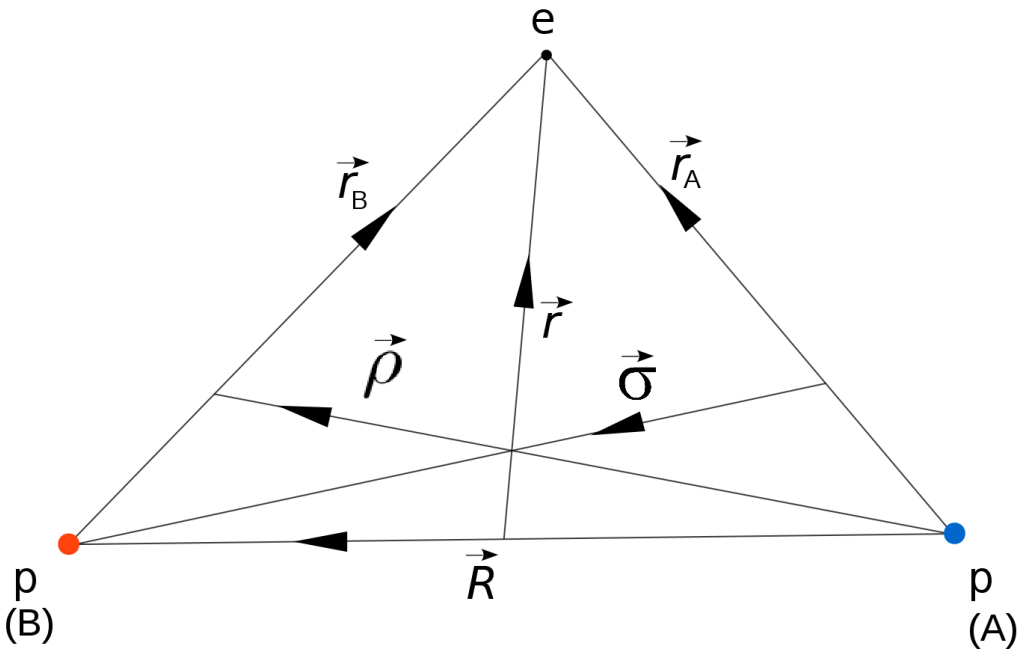

Figure 5.1: Jacobi coordinates for the proton hydrogen collision.

and E being the total energy,

$$E \equiv \frac{k_i^2}{2\mu} + \epsilon_i \quad (i = \alpha, \beta), \tag{5.5}$$

k_i is the momentum of the nucleus-electron system in channel i, μ is the reduced mass and ϵ_i is the eigenenergy corresponding to level i.

The total wave function is expanded as

$$\Psi = \sum_{\alpha=1}^{N_\alpha} F_\alpha^A(\boldsymbol{r}_A, \boldsymbol{\sigma}) e^{i\boldsymbol{k}_\alpha \boldsymbol{\sigma}} + \sum_{\beta=1}^{N_\beta} G_\beta^B(\boldsymbol{r}_B, \boldsymbol{\rho}) e^{i\boldsymbol{k}_\beta \boldsymbol{\rho}}. \tag{5.6}$$

where $F_\alpha^A(\boldsymbol{r}_A, \boldsymbol{\sigma})$ and $G_\beta^B(\boldsymbol{r}_B, \boldsymbol{\rho})$ are the wave functions of the target nucleus-electron and projectile nucleus-electron systems, respectively. N_α and N_β denote the number of states in centres A and B, respectively.

Substituting the expansion (5.6) into the Schrödinger equation (5.1), we get

$$\begin{aligned}
&\sum_{\alpha=1}^{N_\alpha}\left[-\frac{1}{2\mu}\nabla_{\boldsymbol{\sigma}}^2-\frac{1}{2}\nabla_{\boldsymbol{r}_A}^2+V\right]F_\alpha^A(\boldsymbol{r}_A,\boldsymbol{\sigma})e^{i\boldsymbol{k}_\alpha\boldsymbol{\sigma}}\\
&+\sum_{\beta=1}^{N_\beta}\left[-\frac{1}{2\mu}\nabla_{\boldsymbol{\rho}}^2-\frac{1}{2}\nabla_{\boldsymbol{r}_B}^2+V\right]G_\beta^B(\boldsymbol{r}_B,\boldsymbol{\rho})e^{i\boldsymbol{k}_\beta\boldsymbol{\rho}}\\
&=E\sum_{\alpha=1}^{N_\alpha}F_\alpha^A(\boldsymbol{r}_A,\boldsymbol{\sigma})e^{i\boldsymbol{k}_\alpha\boldsymbol{\sigma}}+E\sum_{\beta=1}^{N_\beta}G_\beta^B(\boldsymbol{r}_B,\boldsymbol{\rho})e^{i\boldsymbol{k}_\beta\boldsymbol{\rho}}. \qquad (5.7)
\end{aligned}$$

Equation (5.7) can be written

$$\begin{aligned}
&-\frac{1}{2\mu}\sum_{\alpha=1}^{N_\alpha}\nabla_{\boldsymbol{\sigma}}\left[\nabla_{\boldsymbol{\sigma}}F_\alpha^A(\boldsymbol{r}_A,\boldsymbol{\sigma})e^{i\boldsymbol{k}_\alpha\boldsymbol{\sigma}}\right]+\sum_{\alpha=1}^{N_\alpha}H_eF_\alpha^A(\boldsymbol{r}_A,\boldsymbol{\sigma})e^{i\boldsymbol{k}_\alpha\boldsymbol{\sigma}}\\
&-E\sum_{\alpha=1}^{N_\alpha}F_\alpha^A(\boldsymbol{r}_A,\boldsymbol{\sigma})e^{i\boldsymbol{k}_\alpha\boldsymbol{\sigma}}-\frac{1}{2\mu}\sum_{\beta=1}^{N_\beta}\nabla_{\boldsymbol{\rho}}\left[\nabla_{\boldsymbol{\rho}}G_\beta^B(\boldsymbol{r}_B,\boldsymbol{\rho})e^{i\boldsymbol{k}_\beta\boldsymbol{\rho}}\right]\\
&+\sum_{\beta=1}^{N_\beta}H_eG_\beta^B(\boldsymbol{r}_B,\boldsymbol{\rho})e^{i\boldsymbol{k}_\beta\boldsymbol{\rho}}-E\sum_{\beta=1}^{N_\beta}G_\beta^B(\boldsymbol{r}_B,\boldsymbol{\rho})e^{i\boldsymbol{k}_\beta\boldsymbol{\rho}}=0, \qquad (5.8)
\end{aligned}$$

with the electronic Hamiltonian

$$H_e=-\frac{1}{2}\nabla_{\boldsymbol{r}_A}^2+V=-\frac{1}{2}\nabla_{\boldsymbol{r}_B}^2+V. \qquad (5.9)$$

Given

$$\nabla_{\boldsymbol{\sigma}}F_\alpha^A(\boldsymbol{r}_A,\boldsymbol{\sigma})e^{i\boldsymbol{k}_\alpha\boldsymbol{\sigma}}=F_\alpha^A(\boldsymbol{r}_A,\boldsymbol{\sigma})\nabla_{\boldsymbol{\sigma}}e^{i\boldsymbol{k}_\alpha\boldsymbol{\sigma}}+e^{i\boldsymbol{k}_\alpha\boldsymbol{\sigma}}\nabla_{\boldsymbol{\sigma}}F_\alpha^A(\boldsymbol{r}_A,\boldsymbol{\sigma}) \qquad (5.10)$$

and

$$\nabla_{\boldsymbol{\rho}}G_\beta^B(\boldsymbol{r}_B,\boldsymbol{\rho})e^{i\boldsymbol{k}_\beta\boldsymbol{\rho}}=G_\beta^B(\boldsymbol{r}_B,\boldsymbol{\rho})\nabla_{\boldsymbol{\rho}}e^{i\boldsymbol{k}_\beta\boldsymbol{\rho}}+e^{i\boldsymbol{k}_\beta\boldsymbol{\rho}}\nabla_{\boldsymbol{\rho}}G_\beta^B(\boldsymbol{r}_B,\boldsymbol{\rho}), \qquad (5.11)$$

Eq. (5.8) becomes

$$
\begin{aligned}
&-\frac{1}{2\mu}\sum_{\alpha=1}^{N_\alpha}\left\{2\left[\nabla_{\boldsymbol{\sigma}}e^{i\boldsymbol{k}_\alpha\boldsymbol{\sigma}}\right]\left[\nabla_{\boldsymbol{\sigma}}F_\alpha^A(\boldsymbol{r}_A,\boldsymbol{\sigma})\right]+e^{i\boldsymbol{k}_\alpha\boldsymbol{\sigma}}\nabla_{\boldsymbol{\sigma}}^2F_\alpha^A(\boldsymbol{r}_A,\boldsymbol{\sigma})\right\}\\
&+\sum_{\alpha=1}^{N_\alpha}F_\alpha^A(\boldsymbol{r}_A,\boldsymbol{\sigma})\left[-\frac{1}{2\mu}\nabla_{\boldsymbol{\sigma}}^2-E\right]e^{i\boldsymbol{k}_\alpha\boldsymbol{\sigma}}+\sum_{\alpha=1}^{N_\alpha}H_eF_\alpha^A(\boldsymbol{r}_A,\boldsymbol{\sigma})e^{i\boldsymbol{k}_\alpha\boldsymbol{\sigma}}\\
&-\frac{1}{2\mu}\sum_{\beta=1}^{N_\beta}\left\{2\left[\nabla_{\boldsymbol{\rho}}e^{i\boldsymbol{k}_\beta\boldsymbol{\rho}}\right]\left[\nabla_{\boldsymbol{\rho}}G_\beta^B(\boldsymbol{r}_B,\boldsymbol{\rho})\right]+e^{i\boldsymbol{k}_\beta\boldsymbol{\rho}}\nabla_{\boldsymbol{\rho}}^2G_\beta^B(\boldsymbol{r}_B,\boldsymbol{\rho})\right\}\\
&+\sum_{\beta=1}^{N_\beta}G_\beta^B(\boldsymbol{r}_B,\boldsymbol{\rho})\left[-\frac{1}{2\mu}\nabla_{\boldsymbol{\rho}}^2-E\right]e^{i\boldsymbol{k}_\beta\boldsymbol{\rho}}+\sum_{\beta=1}^{N_\beta}H_eG_\beta^B(\boldsymbol{r}_B,\boldsymbol{\rho})e^{i\boldsymbol{k}_\beta\boldsymbol{\rho}}=0. \qquad (5.12)
\end{aligned}
$$

The Born-Oppenheimer separation allows one to separate the electronic and nuclear motions [12]. Under this semi-classical approximation, the wave function F_α^A (G_β^B) is assumed to vary slowly with $\boldsymbol{\sigma}$ ($\boldsymbol{\rho}$) and the term containing $\nabla_{\boldsymbol{\sigma}}^2F_\alpha^A$ ($\nabla_{\boldsymbol{\rho}}^2G_\beta^B$) in Eq. (5.12) can be neglected (see chapter 3 in [13]).

Taking into account

$$\nabla_{\boldsymbol{\sigma}}e^{i\boldsymbol{k}_\alpha\boldsymbol{\sigma}}=i\boldsymbol{k}_\alpha e^{i\boldsymbol{k}_\alpha\boldsymbol{\sigma}},\quad \nabla_{\boldsymbol{\sigma}}^2e^{i\boldsymbol{k}_\alpha\boldsymbol{\sigma}}=-k_\alpha^2e^{i\boldsymbol{k}_\alpha\boldsymbol{\sigma}}, \qquad (5.13)$$

$$\nabla_{\boldsymbol{\rho}}e^{i\boldsymbol{k}_\beta\boldsymbol{\rho}}=i\boldsymbol{k}_\beta e^{i\boldsymbol{k}_\beta\boldsymbol{\rho}},\quad \nabla_{\boldsymbol{\rho}}^2e^{i\boldsymbol{k}_\beta\boldsymbol{\rho}}=-k_\beta^2e^{i\boldsymbol{k}_\beta\boldsymbol{\rho}}, \qquad (5.14)$$

and neglecting terms $\nabla_{\boldsymbol{\sigma}}^2F_\alpha^A(\boldsymbol{r}_A,\boldsymbol{\sigma})$, $\nabla_{\boldsymbol{\rho}}^2G_\beta^B(\boldsymbol{r}_B,\boldsymbol{\rho})$ in Eq. (5.12), we have

$$
\begin{aligned}
&-\frac{i}{\mu}\sum_{\alpha=1}^{N_\alpha}\boldsymbol{k}_\alpha e^{i\boldsymbol{k}_\alpha\boldsymbol{\sigma}}\nabla_{\boldsymbol{\sigma}}F_\alpha^A(\boldsymbol{r}_A,\boldsymbol{\sigma})+\sum_{\alpha=1}^{N_\alpha}e^{i\boldsymbol{k}_\alpha\boldsymbol{\sigma}}(H_e-\epsilon_\alpha)F_\alpha^A(\boldsymbol{r}_A,\boldsymbol{\sigma})\\
&-\frac{i}{\mu}\sum_{\beta=1}^{N_\beta}\boldsymbol{k}_\beta e^{i\boldsymbol{k}_\beta\boldsymbol{\rho}}\nabla_{\boldsymbol{\rho}}G_\beta^B(\boldsymbol{r}_B,\boldsymbol{\rho})+\sum_{\beta=1}^{N_\beta}e^{i\boldsymbol{k}_\beta\boldsymbol{\rho}}(H_e-\epsilon_\beta)G_\beta^B(\boldsymbol{r}_B,\boldsymbol{\rho})=0. \qquad (5.15)
\end{aligned}
$$

With some simple algebra we get

$$\frac{\boldsymbol{k}_\alpha}{\mu}\nabla_{\boldsymbol{\sigma}}=\frac{\partial}{\partial t},\quad \frac{\boldsymbol{k}_\beta}{\mu}\nabla_{\boldsymbol{\rho}}=\frac{\partial}{\partial t}. \qquad (5.16)$$

which allows us to write Eq. (5.15) in the form

$$
\begin{aligned}
&-i\sum_{\alpha=1}^{N_\alpha} e^{i\boldsymbol{k}_\alpha\boldsymbol{\sigma}}\frac{\partial}{\partial t}F_\alpha^A(\boldsymbol{r}_A,\boldsymbol{\sigma})+\sum_{\alpha=1}^{N_\alpha} e^{i\boldsymbol{k}_\alpha\boldsymbol{\sigma}}(H_e-\epsilon_\alpha)F_\alpha^A(\boldsymbol{r}_A,\boldsymbol{\sigma})\\
&-i\sum_{\beta=1}^{N_\beta} e^{i\boldsymbol{k}_\beta\boldsymbol{\rho}}\frac{\partial}{\partial t}G_\beta^B(\boldsymbol{r}_B,\boldsymbol{\rho})+\sum_{\beta=1}^{N_\beta} e^{i\boldsymbol{k}_\beta\boldsymbol{\rho}}(H_e-\epsilon_\beta)G_\beta^B(\boldsymbol{r}_B,\boldsymbol{\rho})=0. \qquad (5.17)
\end{aligned}
$$

We decompose the Hamiltonian

$$H_e=H_{\rm t}^A+V^A(R,r_B)=H_{\rm t}^B+V^B(R,r_A), \qquad (5.18)$$

with

$$V^A(R,r_B)=\frac{1}{R}-\frac{1}{r_B},\quad V^B(R,r_A)=\frac{1}{R}-\frac{1}{r_A}, \qquad (5.19)$$

where

$$H_{\rm t}^A=-\frac{1}{2}\Delta_{\boldsymbol{r}_A}-\frac{1}{r_A},\quad H_{\rm t}^B=-\frac{1}{2}\Delta_{\boldsymbol{r}_B}-\frac{1}{r_B}. \qquad (5.20)$$

Then we define ψ_α^A (ψ_β^B) to be the eigenfunctions of the target (projectile) Hamiltonian

$$H_{\rm t}^A\psi_\alpha^A(\boldsymbol{r}_A)=\epsilon_\alpha\psi_\alpha^A(\boldsymbol{r}_A), \qquad (5.21)$$

$$H_{\rm t}^B\psi_\beta^B(\boldsymbol{r}_B)=\epsilon_\beta\psi_\beta^B(\boldsymbol{r}_B). \qquad (5.22)$$

We now separate the time-dependence in $F_\alpha^A(\boldsymbol{r}_A,\boldsymbol{\sigma})$ and $G_\beta^B(\boldsymbol{r}_B,\boldsymbol{\rho})$ as

$$
\begin{aligned}
F_\alpha^A(\boldsymbol{r}_A,\boldsymbol{\sigma})&=a_\alpha(t)\psi_\alpha^A(\boldsymbol{r}_A),\\
G_\beta^B(\boldsymbol{r}_B,\boldsymbol{\rho})&=b_\beta(t)\psi_\beta^B(\boldsymbol{r}_B).
\end{aligned} \qquad (5.23)
$$

Eq. (5.17) can be written in the form

$$
\begin{aligned}
&-i\sum_{\alpha=1}^{N_\alpha}\dot{a}_\alpha(t)\psi_\alpha^A(\boldsymbol{r}_A)e^{i\boldsymbol{k}_\alpha\boldsymbol{\sigma}}+\sum_{\alpha=1}^{N_\alpha}a_\alpha(t)\psi_\alpha^A(\boldsymbol{r}_A)V^A(R,r_B)e^{i\boldsymbol{k}_\alpha\boldsymbol{\sigma}}\\
&-i\sum_{\beta=1}^{N_\beta}\dot{b}_\beta(t)\psi_\beta^B(\boldsymbol{r}_B)e^{i\boldsymbol{k}_\beta\boldsymbol{\rho}}+\sum_{\beta=1}^{N_\beta}b_\beta(t)\psi_\beta^B(\boldsymbol{r}_B)V^B(R,r_A)e^{i\boldsymbol{k}_\beta\boldsymbol{\rho}}=0. \qquad (5.24)
\end{aligned}
$$

Multiplying Eq. (5.24) by $\psi^{A*}_{\alpha'}(\boldsymbol{r}_A)e^{-i\boldsymbol{k}_{\alpha'}\boldsymbol{\sigma}}$ and integrating over $\boldsymbol{r}_A$, we obtain

$$
\begin{aligned}
& i\sum_{\alpha=1}^{N_\alpha}\dot{a}_\alpha\int d\boldsymbol{r}_A\psi^{A*}_{\alpha'}(\boldsymbol{r}_A)e^{i(\boldsymbol{k}_\alpha-\boldsymbol{k}_{\alpha'})\boldsymbol{\sigma}}\psi^{A}_{\alpha}(\boldsymbol{r}_A) \\
& + i\sum_{\beta=1}^{N_\beta}\dot{b}_\beta\int d\boldsymbol{r}_A\psi^{A*}_{\alpha'}(\boldsymbol{r}_A)e^{i\left(\boldsymbol{k}_\beta\boldsymbol{\rho}-\boldsymbol{k}_{\alpha'}\boldsymbol{\sigma}\right)}\psi^{B}_{\beta}(\boldsymbol{r}_B) \\
& = \sum_{\alpha=1}^{N_\alpha}a_\alpha\int d\boldsymbol{r}_A\psi^{A*}_{\alpha'}(\boldsymbol{r}_A)e^{i(\boldsymbol{k}_\alpha-\boldsymbol{k}_{\alpha'})\boldsymbol{\sigma}}V^A(R,r_B)\psi^{A}_{\alpha}(\boldsymbol{r}_A) \\
& + \sum_{\beta=1}^{N_\beta}b_\beta\int d\boldsymbol{r}_A\psi^{A*}_{\alpha'}(\boldsymbol{r}_A)e^{i\left(\boldsymbol{k}_\beta\boldsymbol{\rho}-\boldsymbol{k}_{\alpha'}\boldsymbol{\sigma}\right)}V^B(R,r_A)\psi^{B}_{\beta}(\boldsymbol{r}_B). \qquad (5.25)
\end{aligned}
$$

Eq. (5.25) can be further simplified by considering the exponentials. This is achieved by introducing the momentum transfers

$$\boldsymbol{p}=\gamma\boldsymbol{k}_{\alpha'}-\boldsymbol{k}_\beta,\quad \boldsymbol{q}=\gamma\boldsymbol{k}_\beta-\boldsymbol{k}_{\alpha'} \qquad (5.26)$$

with components

$$p_\parallel=-\frac{v}{2}+\frac{\Delta\epsilon}{v},\quad q_\parallel=-\frac{v}{2}-\frac{\Delta\epsilon}{v},\quad p_\perp=-q_\perp, \qquad (5.27)$$

where

$$\Delta\epsilon=\epsilon_\beta-\epsilon_{\alpha'} \qquad (5.28)$$

and $\gamma=m_p/(m_p+1)$, with m_p being the proton mass.

From Figure 5.1 we see that

$$\boldsymbol{\rho}=\boldsymbol{r}_A-\gamma\boldsymbol{r}_B,\quad \boldsymbol{\sigma}=\gamma\boldsymbol{r}_A-\boldsymbol{r}_B, \qquad (5.29)$$

Expressing $\boldsymbol{r}_B$ via $\boldsymbol{r}_A$ in (5.29) and taking into account $\boldsymbol{q}+\boldsymbol{p}=-\boldsymbol{v}$ we get

$$e^{i(\boldsymbol{k}_\beta\boldsymbol{\rho}-\boldsymbol{k}_{\alpha'}\boldsymbol{\sigma})}=e^{i\boldsymbol{q}\boldsymbol{R}}e^{i\boldsymbol{v}\boldsymbol{r}_A}=e^{iq_\perp b}e^{iq_\parallel Z}e^{i\boldsymbol{v}\boldsymbol{r}_A}, \qquad (5.30)$$

where we used

$$\boldsymbol{R}=\boldsymbol{b}+Z\hat{\mathbf{v}}, \qquad (5.31)$$

with $\hat{\mathbf{v}}$ being a unit vector along the incident velocity $\boldsymbol{v}$ and $Z \equiv vt$.

For the power of the other exponential factor in Eq. (5.25), using $\boldsymbol{\sigma} \approx \boldsymbol{R}$ approximation we may write

$$(\boldsymbol{k}_\alpha - \boldsymbol{k}_{\alpha'})\boldsymbol{\sigma} \approx (\boldsymbol{k}_\alpha - \boldsymbol{k}_{\alpha'})\boldsymbol{R} = (\boldsymbol{k}_\alpha - \boldsymbol{k}_{\alpha'})_\parallel Z + (\boldsymbol{k}_\alpha - \boldsymbol{k}_{\alpha'})_\perp b. \tag{5.32}$$

Within the small angle approximation the components of the vector $\boldsymbol{k}_\alpha - \boldsymbol{k}_{\alpha'}$ are

$$(\boldsymbol{k}_\alpha - \boldsymbol{k}_{\alpha'})_\parallel = k_\alpha - k_{\alpha'}\cos\theta \approx k_\alpha - k_{\alpha'} = \frac{\epsilon_\alpha - \epsilon_{\alpha'}}{v}, \tag{5.33}$$

and

$$(\boldsymbol{k}_\alpha - \boldsymbol{k}_{\alpha'})_\perp = 0, \tag{5.34}$$

where θ is a small scattering angle. Consequently,

$$e^{i(\boldsymbol{k}_\alpha - \boldsymbol{k}_{\alpha'})\boldsymbol{\sigma}} = e^{i(\epsilon_\alpha - \epsilon_{\alpha'})t}. \tag{5.35}$$

With the considered simplifications of the exponential factors, Eq. (5.25) reduces to

$$\begin{aligned}
&ie^{iq_\perp b}\sum_{\alpha=1}^{N_\alpha}\dot{a}_\alpha e^{(\epsilon_\alpha-\epsilon_{\alpha'})t}\int d\boldsymbol{r}_A\psi^{A*}_{\alpha'}(\boldsymbol{r}_A)\psi^A_\alpha(\boldsymbol{r}_A)\\
&+ ie^{iq_\perp b}\sum_{\beta=1}^{N_\beta}\dot{b}_\beta e^{iq_\parallel Z}\int d\boldsymbol{r}_A\psi^{A*}_{\alpha'}(\boldsymbol{r}_A)e^{i\boldsymbol{v}\boldsymbol{r}_A}\psi^B_\beta(\boldsymbol{r}_B)\\
&= e^{iq_\perp b}\sum_{\alpha=1}^{N_\alpha}a_\alpha e^{(\epsilon_\alpha-\epsilon_{\alpha'})t}\int d\boldsymbol{r}_A\psi^{A*}_{\alpha'}(\boldsymbol{r}_A)V^A(R,r_B)\psi^A_\alpha(\boldsymbol{r}_A)\\
&+ e^{iq_\perp b}\sum_{\beta=1}^{N_\beta}b_\beta e^{iq_\parallel Z}\int d\boldsymbol{r}_A\psi^{A*}_{\alpha'}(\boldsymbol{r}_A)e^{i\boldsymbol{v}\boldsymbol{r}_A}V^B(R,r_A)\psi^B_\beta(\boldsymbol{r}_B).
\end{aligned} \tag{5.36}$$

Taking into account the orthonormality of functions $\psi^A(\boldsymbol{r}_A)$

$$\int d\boldsymbol{r}_A\psi^{A*}_{\alpha'}(\boldsymbol{r}_A)\psi^A_\alpha(\boldsymbol{r}_A) = \delta_{\alpha'\alpha} \tag{5.37}$$

and dropping the common factor $e^{iq_\perp b}$ one can write Eq. (5.36) as

$$i\dot{a}_{\alpha'} + i\sum_{\beta=1}^{N_\beta} \dot{b}_\beta K^A_{\alpha'\beta} = \sum_{\alpha=1}^{N_\alpha} a_\alpha D^A_{\alpha'\alpha} + \sum_{\beta=1}^{N_\beta} b_\beta Q^A_{\alpha'\beta}, \quad \alpha' = 1, 2, 3, \ldots, N_\alpha. \tag{5.38}$$

where

$$\begin{aligned} K^A_{\alpha'\beta} =& e^{iq_\parallel Z} \int d\boldsymbol{r}_A \psi^{A*}_{\alpha'}(\boldsymbol{r}_A) e^{i\boldsymbol{v}\boldsymbol{r}_A} \psi^B_\beta(\boldsymbol{r}_B), & (5.39)\\ D^A_{\alpha'\alpha} =& e^{i(\epsilon_{\alpha'}-\epsilon_\alpha)t} \int d\boldsymbol{r}_A \psi^{A*}_{\alpha'}(\boldsymbol{r}_A) \left(\frac{1}{R} - \frac{1}{r_B}\right) \psi^A_\alpha(\boldsymbol{r}_A) \\ =& e^{i(\epsilon_{\alpha'}-\epsilon_\alpha)t} \left(\frac{\delta_{\alpha'\alpha}}{R} + \tilde{C}^A_{\alpha'\alpha}\right), & (5.40)\\ Q^A_{\alpha'\beta} =& e^{iq_\parallel Z} \int d\boldsymbol{r}_A \psi^{A*}_{\alpha'}(\boldsymbol{r}_A) e^{i\boldsymbol{v}\boldsymbol{r}_A} \left(\frac{1}{R} - \frac{1}{r_A}\right) \psi^B_\beta(\boldsymbol{r}_B) \\ =& e^{iq_\parallel Z} \left(\frac{K^A_{\alpha'\beta}}{R} + P^A_{\alpha'\beta}\right), & (5.41) \end{aligned}$$

with

$$\tilde{C}^A_{\alpha'\alpha} = -\int d\boldsymbol{r}_A \psi^{A*}_{\alpha'}(\boldsymbol{r}_A) \frac{1}{r_B} \psi^A_\alpha(\boldsymbol{r}_A). \tag{5.42}$$

and

$$P^A_{\alpha'\beta} = -\, e^{iq_\parallel Z} \int d\boldsymbol{r}_A \psi^{A*}_{\alpha'}(\boldsymbol{r}_A) \frac{e^{i\boldsymbol{v}\boldsymbol{r}_A}}{r_A} \psi^B_\beta(\boldsymbol{r}_B). \tag{5.43}$$

Similarly, multiplying Eq. (5.24) by $\psi^{B*}_{\beta'}(\boldsymbol{r}_B) e^{-i\boldsymbol{k}_{\beta'}\boldsymbol{\rho}}$ and integrating over $\boldsymbol{r}_B$ we get

$$\begin{aligned} & i\sum_{\alpha=1}^{N_\alpha} \dot{a}_\alpha \int d\boldsymbol{r}_B \psi^{B*}_{\beta'}(\boldsymbol{r}_B) e^{i\left(\boldsymbol{k}_\alpha\boldsymbol{\sigma} - \boldsymbol{k}_{\beta'}\boldsymbol{\rho}\right)} \psi^A_\alpha(\boldsymbol{r}_A) \\ & + i\sum_{\beta=1}^{N_\beta} \dot{b}_\beta \int d\boldsymbol{r}_B \psi^{B*}_{\beta'}(\boldsymbol{r}_B) e^{i(\boldsymbol{k}_\beta - \boldsymbol{k}_{\beta'})\boldsymbol{\rho}} \psi^B_\beta(\boldsymbol{r}_B) \\ & = \sum_{\alpha=1}^{N_\alpha} a_\alpha \int d\boldsymbol{r}_B \psi^{B*}_{\beta'}(\boldsymbol{r}_B) e^{i\left(\boldsymbol{k}_\alpha\boldsymbol{\sigma} - \boldsymbol{k}_{\beta'}\boldsymbol{\rho}\right)} V^A(R, r_B) \psi^A_\alpha(\boldsymbol{r}_A) \\ & + \sum_{\beta=1}^{N_\beta} b_\beta \int d\boldsymbol{r}_B \psi^{B*}_{\beta'}(\boldsymbol{r}_B) e^{i(\boldsymbol{k}_\beta - \boldsymbol{k}_{\beta'})\boldsymbol{\rho}} V^B(R, r_A) \psi^B_\beta(\boldsymbol{r}_B). \end{aligned} \tag{5.44}$$

Redefining the momentum transfers as

$$\boldsymbol{p} = \gamma \boldsymbol{k}_{\beta'} - \boldsymbol{k}_\alpha, \quad \boldsymbol{q} = \gamma \boldsymbol{k}_\alpha - \boldsymbol{k}_{\beta'} \tag{5.45}$$

components of which are defined by (5.27) with

$$\Delta\epsilon = \epsilon_\alpha - \epsilon_{\beta'}. \tag{5.46}$$

we get that the exponentials reduce to

$$e^{i(\boldsymbol{k}_\alpha \boldsymbol{\sigma} - \boldsymbol{k}_{\beta'} \boldsymbol{\rho})} = e^{iq_\perp b} e^{iq_\parallel Z} e^{-i\boldsymbol{v}\boldsymbol{r}_B}, \tag{5.47}$$

$$e^{i(\boldsymbol{k}_\beta - \boldsymbol{k}_{\beta'})\boldsymbol{\rho}} = e^{i(\epsilon_\beta - \epsilon_{\beta'})t}. \tag{5.48}$$

Within the small angle approximation the components of the vector $\boldsymbol{k}_\beta - \boldsymbol{k}_{\beta'}$ become

$$(\boldsymbol{k}_\beta - \boldsymbol{k}_{\beta'})_\parallel = k_\beta - k_{\beta'} \cos\theta \approx k_\beta - k_{\beta'} = \frac{\epsilon_\beta - \epsilon_{\beta'}}{v}, \tag{5.49}$$

and

$$(\boldsymbol{k}_\beta - \boldsymbol{k}_{\beta'})_\perp = 0, \tag{5.50}$$

where θ is a small scattering angle.

Proceeding as before, i.e. taking into account the orthonormality of functions $\psi^B(\boldsymbol{r}_B)$, and neglecting the common factor we reduce Eq. (5.44) to

$$i \sum_{\alpha=1}^{N_\alpha} \dot{a}_\alpha K^B_{\beta'\alpha} + i\dot{b}_{\beta'} = \sum_{\alpha=1}^{N_\alpha} a_\alpha Q^B_{\beta'\alpha} + \sum_{\beta=1}^{N_\beta} b_\beta D^B_{\beta'\beta}, \quad \beta' = 1, 2, 3, \ldots, N_\beta, \tag{5.51}$$

where

$$K^B_{\beta'\alpha} = e^{iq_\parallel Z} \int d\boldsymbol{r}_B \psi^{B*}_{\beta'}(\boldsymbol{r}_B) e^{-i\boldsymbol{v}\boldsymbol{r}_B} \psi^A_\alpha(\boldsymbol{r}_A). \tag{5.52}$$

$$\begin{aligned} D^B_{\beta'\beta} &= e^{i(\epsilon_{\beta'} - \epsilon_\beta)t} \int d\boldsymbol{r}_B \psi^{B*}_{\beta'}(\boldsymbol{r}_B) \left(\frac{1}{R} - \frac{1}{r_A} \right) \psi^B_\beta(\boldsymbol{r}_B) \\ &= e^{i(\epsilon_{\beta'} - \epsilon_\beta)t} \left(\frac{\delta_{\beta'\beta}}{R} + \tilde{C}^B_{\beta'\beta} \right), \end{aligned} \tag{5.53}$$

$$
\begin{aligned}
Q^B_{\beta'\beta} =& e^{iq_\parallel Z} \int d\boldsymbol{r}_B \psi^{B*}_{\beta'}(\boldsymbol{r}_B) e^{-i\boldsymbol{v}\boldsymbol{r}_B} \left(\frac{1}{R} - \frac{1}{r_B} \right) \psi^A_\alpha(\boldsymbol{r}_A) \\
=& e^{iq_\parallel Z} \left(\frac{K^B_{\beta'\alpha}}{R} + P^B_{\beta'\alpha} \right),
\end{aligned} \tag{5.54}
$$

with

$$
\tilde{C}^B_{\beta'\beta} = - \int d\boldsymbol{r}_B \psi^{B*}_{\beta'}(\boldsymbol{r}_B) \frac{1}{r_A} \psi^B_\beta(\boldsymbol{r}_B). \tag{5.55}
$$

and

$$
P^B_{\beta'\alpha} = - e^{iq_\parallel Z} \int d\boldsymbol{r}_B \psi^{B*}_{\beta'}(\boldsymbol{r}_B) \frac{e^{-i\boldsymbol{v}\boldsymbol{r}_B}}{r_B} \psi^A_\alpha(\boldsymbol{r}_A). \tag{5.56}
$$

System of differential equations (5.38) and (5.51)

$$
\begin{cases}
i\dot{a}_{\alpha'} + i \sum\limits_{\beta=1}^{N_\beta} \dot{b}_\beta K^A_{\alpha'\beta} = \sum\limits_{\alpha=1}^{N_\alpha} a_\alpha D^A_{\alpha'\alpha} + \sum\limits_{\beta=1}^{N_\beta} b_\beta Q^A_{\alpha'\beta}, \quad \alpha' = 1, 2, 3, \ldots, N_\alpha, & (5.57) \\
i \sum\limits_{\alpha=1}^{N_\alpha} \dot{a}_\alpha K^B_{\beta'\alpha} + i\dot{b}_{\beta'} = \sum\limits_{\alpha=1}^{N_\alpha} a_\alpha Q^B_{\beta'\alpha} + \sum\limits_{\beta=1}^{N_\beta} b_\beta D^B_{\beta'\beta}, \quad \beta' = 1, 2, 3, \ldots, N_\beta, & (5.58)
\end{cases}
$$

can be combined and written in the matrix form as

$$
i \begin{pmatrix} \boldsymbol{I} & \boldsymbol{K}^A \\ \boldsymbol{K}^B & \boldsymbol{I} \end{pmatrix} \begin{pmatrix} \dot{\boldsymbol{a}} \\ \dot{\boldsymbol{b}} \end{pmatrix} = \begin{pmatrix} \boldsymbol{D}^A & \boldsymbol{Q}^A \\ \boldsymbol{Q}^B & \boldsymbol{D}^B \end{pmatrix} \begin{pmatrix} \boldsymbol{a} \\ \boldsymbol{b} \end{pmatrix}, \tag{5.59}
$$

where $\boldsymbol{I}$ is the identity matrix, submatrices $\boldsymbol{K}$, $\boldsymbol{Q}$ and $\boldsymbol{D}$ contain the corresponding matrix elements.

The conservation of the norm of the total wave function (5.6) is a useful check on the numerical integration of the coupled differential equations (5.59).

We define the norm as

$$\begin{aligned}
N(t) &= \int d\boldsymbol{r}\Psi^*(\boldsymbol{r},t)\Psi(\boldsymbol{r},t) \\
&= \int d\boldsymbol{r}\left[\sum_{\alpha'=1}^{N_\alpha} a^*_{\alpha'}\psi^{A*}_{\alpha'}e^{-i\boldsymbol{k}_{\alpha'}\boldsymbol{\sigma}} + \sum_{\beta'=1}^{N_\beta} b^*_{\beta'}\psi^{B*}_{\beta'}e^{-i\boldsymbol{k}_{\beta'}\boldsymbol{\rho}}\right] \\
&\quad\times\left[\sum_{\alpha=1}^{N_\alpha} a_\alpha\psi^A_\alpha e^{i\boldsymbol{k}_\alpha\boldsymbol{\sigma}} + \sum_{\beta=1}^{N_\beta} b_\beta\psi^B_\beta e^{i\boldsymbol{k}_\beta\boldsymbol{\rho}}\right] \\
&= \sum_{\alpha=1}^{N_\alpha}|a_\alpha|^2 + \sum_{\beta=1}^{N_\beta}|b_\beta|^2 + \sum_{\alpha'=1}^{N_\alpha} a^*_{\alpha'}\sum_{\beta=1}^{N_\beta} b_\beta\int d\boldsymbol{r}_A\psi^{A*}_{\alpha'}e^{i(\boldsymbol{k}_\beta\boldsymbol{\rho}-\boldsymbol{k}_{\alpha'}\boldsymbol{\sigma})}\psi^B_\beta \\
&\quad + \sum_{\beta'=1}^{N_\beta} b^*_{\beta'}\sum_{\alpha=1}^{N_\alpha} a_\alpha\int d\boldsymbol{r}_B\psi^{B*}_{\beta'}e^{i(\boldsymbol{k}_\alpha\boldsymbol{\sigma}-\boldsymbol{k}_{\beta'}\boldsymbol{\rho})}\psi^A_\alpha. \qquad (5.60)
\end{aligned}$$

Taking into account (5.30), (5.47), (5.39) and (5.53), Eq. (5.60) reduces to

$$N(t) = \sum_{\alpha=1}^{N_\alpha}|a_\alpha|^2 + \sum_{\beta=1}^{N_\beta}|b_\beta|^2 + \sum_{\alpha'=1}^{N_\alpha} a^*_{\alpha'}\sum_{\beta=1}^{N_\beta} b_\beta K^A_{\alpha'\beta} + \sum_{\beta'=1}^{N_\beta} b^*_{\beta'}\sum_{\alpha=1}^{N_\alpha} a_\alpha K^B_{\beta'\alpha}. \qquad (5.61)$$

Equation (5.61) represents the unitarity condition to be satisfied by the total wave function and it will be employed in the numerical computations. In the ideal case, the sum given by (5.61) should equal unity along the integration path at each impact parameter. Numerical accuracy to which the unitarity is conserved will be discussed in the next chapter.

System of the differential equations (5.59) is solved under the initial conditions,

$$\begin{aligned}
a_\alpha(-\infty,\boldsymbol{b}) &= \delta_{\alpha 1}, \quad \alpha = 1,2,3,\ldots,N_\alpha, \\
b_\beta(-\infty,\boldsymbol{b}) &= 0, \quad \beta = 1,2,3,\ldots,N_\beta. \qquad (5.62)
\end{aligned}$$

Excitation and electron transfer probabilities are given by

$$P^{\text{excit.}}_\alpha(b) = |a_\alpha(+\infty,\boldsymbol{b})|^2, \qquad (5.63)$$

and

$$P_\beta^{\text{exch.}}(b) = |b_\beta(+\infty, \boldsymbol{b})|^2. \tag{5.64}$$

The corresponding partial cross sections are

$$\sigma_\alpha^{\text{excit.}} = 2\pi \int_0^\infty db\ bP_\alpha^{\text{excit.}}(b), \tag{5.65}$$

and

$$\sigma_\beta^{\text{exch.}} = 2\pi \int_0^\infty db\ bP_\beta^{\text{exch.}}(b). \tag{5.66}$$

The total ionisation cross section is defined as the sum of the partial cross sections corresponding to transitions into the positive energy pseudostates

$$\sigma_{\text{tot}}^{\text{ion}} = \sum_{\alpha,\epsilon_\alpha>0} \sigma_\alpha^{\text{excit.}} + \sum_{\beta,\epsilon_\beta>0} \sigma_\beta^{\text{exch.}}. \tag{5.67}$$

5.3 Direct matrix elements

In this section we describe how the direct matrix elements given by (5.42) and (5.55) are calculated. The calculation procedure of these matrix elements follows similar lines shown in Chapter 2 for the antiproton-hydrogen collision.

We expand $1/r_B$ as follows

$$\frac{1}{r_B} = \frac{1}{|\boldsymbol{r}_A - \boldsymbol{R}|} = 4\pi \sum_{\lambda\mu} \frac{1}{2\lambda+1} \tilde{U}_\lambda(R, r_A) Y_{\lambda\mu}(\widehat{\boldsymbol{R}}) Y_{\lambda\mu}^*(\widehat{\boldsymbol{r}}_A), \tag{5.68}$$

with

$$\tilde{U}_\lambda(R, r_A) = \begin{cases} R^\lambda / r_A^{\lambda+1} & \text{for} \quad r_A \geq R, \\ r_A^\lambda / R^{\lambda+1} & \text{for} \quad r_A < R. \end{cases} \tag{5.69}$$

Then the matrix element $\tilde{C}^A_{\alpha'\alpha}$ is

$$\begin{aligned} \tilde{C}^A_{\alpha'\alpha} = &-4\pi \sum_{\lambda\mu} \frac{1}{2\lambda+1} Y_{\lambda\mu}(\widehat{\boldsymbol{R}}) \int_0^\infty dr_A\ r_A^2 \phi^A_{\ell_{\alpha'} m_{\alpha'}}(r_A) \tilde{U}_\lambda(R, r_A) \phi^A_{\ell_\alpha m_\alpha}(r_A) \\ &\times \int d\widehat{\boldsymbol{r}}_A\ Y^*_{\ell_{\alpha'} m_{\alpha'}}(\widehat{\boldsymbol{r}}_A) Y^*_{\lambda\mu}(\widehat{\boldsymbol{r}}_A) Y_{\ell_\alpha m_\alpha}(\widehat{\boldsymbol{r}}_A), \end{aligned} \tag{5.70}$$

where the functions $\phi_{\ell_\alpha m_\alpha}$ are the radial parts of the target pseudostates, $\psi^A_\alpha(\boldsymbol{r}_A)$.

Angular integration is performed analytically and it is

$$\int d\hat{\boldsymbol{r}}_A Y^*_{\ell_{\alpha'} m_{\alpha'}}(\hat{\boldsymbol{r}}_A) Y^*_{\lambda\mu}(\hat{\boldsymbol{r}}_A) Y_{\ell_\alpha m_\alpha}(\hat{\boldsymbol{r}}_A) = \sqrt{\frac{[\ell_{\alpha'}][\lambda]}{4\pi[\ell_\alpha]}} C^{\ell_\alpha 0}_{\ell_{\alpha'} 0\ \lambda 0} C^{\ell_\alpha m_\alpha}_{\ell_{\alpha'} m_{\alpha'}\ \lambda\mu}, \tag{5.71}$$

with $[L] \equiv 2L+1$ and $\mu = m_\alpha - m_{\alpha'}$. Thus, the matrix element $\tilde{C}^A_{\alpha'\alpha}(\boldsymbol{R})$ is calculated by

$$\begin{aligned}\tilde{C}^A_{\alpha'\alpha}(\boldsymbol{R}) = &- \sqrt{\frac{4\pi[\ell_{\alpha'}]}{[\ell_\alpha]}} \sum_{\lambda=|\ell_\alpha-\ell_{\alpha'}|}^{\ell_\alpha+\ell_{\alpha'}} \frac{C^{\ell_\alpha 0}_{\ell_{\alpha'} 0\ \lambda 0} C^{\ell_\alpha m_\alpha}_{\ell_{\alpha'} m_{\alpha'}\ \lambda\mu}}{\sqrt{[\lambda]}} Y_{\lambda\mu}(\widehat{\boldsymbol{R}}) \\ &\times \int_0^\infty dr_A\ r_A^2 \phi^A_{\ell_{\alpha'} m_{\alpha'}}(r_A) \tilde{U}_\lambda(R, r_A) \phi^A_{\ell_\alpha m_\alpha}(r_A).\end{aligned} \tag{5.72}$$

The other direct matrix element $\tilde{C}^B_{\beta'\beta}(\boldsymbol{R})$ is treated in the same way and the resulting expression for it is

$$\begin{aligned}\tilde{C}^B_{\beta'\beta}(\boldsymbol{R}) = &(-1)^{\ell_\beta+\ell_{\beta'}+1} \sqrt{\frac{4\pi[\ell_{\beta'}]}{[\ell_\beta]}} \sum_{\lambda=|\ell_\beta-\ell_{\beta'}|}^{\ell_\beta+\ell_{\beta'}} \frac{C^{\ell_\beta 0}_{\ell_{\beta'} 0\ \lambda 0} C^{\ell_\beta m_\beta}_{\ell_{\beta'} m_{\beta'}\ \lambda\mu}}{\sqrt{[\lambda]}} Y_{\lambda\mu}(\widehat{\boldsymbol{R}}) \\ &\times \int_0^\infty dr_B\ r_B^2 \phi^B_{\ell_{\beta'} m_{\beta'}}(r_B) \tilde{U}_\lambda(R, r_B) \phi^B_{\ell_\beta m_\beta}(r_B),\end{aligned} \tag{5.73}$$

with $\mu = m_\beta - m_{\beta'}$.

5.4 Exchange matrix elements

We have the following exchange matrix elements:

$$K^A_{\alpha'\beta}(\boldsymbol{R}) = e^{iq_\parallel Z}\tilde{K}^A_{\alpha'\beta}(\boldsymbol{R}), \tag{5.74}$$

$$\tilde{K}^A_{\alpha'\beta}(\boldsymbol{R}) = \int d\boldsymbol{r}_A \psi^{A*}_{\alpha'}(\boldsymbol{r}_A) e^{i\boldsymbol{v}\boldsymbol{r}_A}\psi^B_\beta(\boldsymbol{r}_B). \tag{5.75}$$

$$P^A_{\alpha'\beta}(\boldsymbol{R}) = -\, e^{iq_\parallel Z}\tilde{P}^A_{\alpha'\beta}(\boldsymbol{R}), \tag{5.76}$$

$$\tilde{P}^A_{\alpha'\beta}(\boldsymbol{R}) = \int d\boldsymbol{r}_A \psi^{A*}_{\alpha'}(\boldsymbol{r}_A) \frac{e^{i\boldsymbol{v}\boldsymbol{r}_A}}{r_A}\psi^B_\beta(\boldsymbol{r}_B). \tag{5.77}$$

$$K^B_{\beta'\alpha}(\boldsymbol{R}) = e^{iq_\parallel Z}\tilde{G}^B_{\beta'\alpha}(\boldsymbol{R}), \tag{5.78}$$

$$\tilde{P}^B_{\beta'\alpha}(\boldsymbol{R}) = \int d\boldsymbol{r}_B \psi^{B*}_{\beta'}(\boldsymbol{r}_B) e^{-i\boldsymbol{v}\boldsymbol{r}_B}\psi^A_\alpha(\boldsymbol{r}_A). \tag{5.79}$$

$$P^B_{\beta'\alpha}(\boldsymbol{R}) = -\, e^{iq_\parallel Z}\tilde{K}^B_{\beta'\alpha}(\boldsymbol{R}), \tag{5.80}$$

$$\tilde{P}^B_{\beta'\alpha}(\boldsymbol{R}) = \int d\boldsymbol{r}_B \psi^{B*}_{\beta'}(\boldsymbol{r}_B) \frac{e^{-i\boldsymbol{v}\boldsymbol{r}_B}}{r_B}\psi^A_\alpha(\boldsymbol{r}_A). \tag{5.81}$$

The factors $e^{i\boldsymbol{v}\boldsymbol{r}_A}$ and $e^{-i\boldsymbol{v}\boldsymbol{r}_B}$ in the matrix elements are plane-wave electron-translational factors (PWETF) [12, 56]. In this Section we describe in detail how $\tilde{K}^A_{\alpha'\beta}(\boldsymbol{R})$ matrix elements are calculated. Since the other matrix elements are treated in the same way, only the final expressions will be given for them.

Expressing $\boldsymbol{r}_B$ through $\boldsymbol{r}_A$ by

$$\boldsymbol{r}_B = \boldsymbol{r}_A - \boldsymbol{R}, \tag{5.82}$$

and dropping the index A (i.e. $\boldsymbol{r}_A = \boldsymbol{r}$), $\tilde{K}^A_{\alpha'\beta}$ takes the form

$$\tilde{K}^A_{\alpha'\beta} = \int d\boldsymbol{r} \psi^{A*}_{\alpha'}(\boldsymbol{r}) e^{i\boldsymbol{v}\boldsymbol{r}}\psi^B_\beta(\boldsymbol{r}-\boldsymbol{R}). \tag{5.83}$$

We now separate $\psi^B_\beta(\boldsymbol{r}-\boldsymbol{R})$ into radial and angular parts

$$\psi^B_\beta(\boldsymbol{r}-\boldsymbol{R}) = \phi^B_\beta(|\boldsymbol{r}-\boldsymbol{R}|) Y^B_{\ell_\beta m_\beta}(\widehat{\boldsymbol{r}-\boldsymbol{R}}) \tag{5.84}$$

and expand $Y^B_{\ell_\beta m_\beta}(\widehat{\boldsymbol{r}-\boldsymbol{R}})$ as

$$Y^B_{\ell_\beta m_\beta}(\widehat{\boldsymbol{r}-\boldsymbol{R}}) = \frac{(-1)^{\ell_2}}{|\boldsymbol{r}-\boldsymbol{R}|^{\ell_\beta}} \sum_{\ell_1=0}^{\ell_\beta} \sum_{m_1=-\ell_1}^{\ell_1} (\ell_1 m_1 | \ell_\beta m_\beta) r^{\ell_1} R^{\ell_2} Y_{\ell_1 m_1}(\widehat{\boldsymbol{r}}) Y_{\ell_2 m_2}(\widehat{\boldsymbol{R}}), \tag{5.85}$$

where

$$(\ell_1 m_1|\ell_\beta m_\beta) = \sqrt{\frac{4\pi[\ell_\beta]!}{[\ell_1]![\ell_2]!}} C^{\ell_\beta m_\beta}_{\ell_1 m_1\ \ell_2 m_2} \delta_{\ell_1+\ell_2,\ell_\beta}. \tag{5.86}$$

Further, we expand

$$\frac{\phi^B_\beta(|\boldsymbol{r}-\boldsymbol{R}|)}{|\boldsymbol{r}-\boldsymbol{R}|^{\ell_\beta}} = 2\pi \sum_{\lambda\mu}^{\infty} g^B_\beta(\lambda, R, r) Y_{\lambda\mu}(\widehat{\boldsymbol{r}}) Y^*_{\lambda\mu}(\widehat{\boldsymbol{R}}), \tag{5.87}$$

with

$$g^B_\beta(\lambda, R, r) = \int_{-1}^{1} dz \frac{\phi^B_\beta(|\boldsymbol{r}-\boldsymbol{R}|)}{|\boldsymbol{r}-\boldsymbol{R}|^{\ell_\beta}} P_\lambda(z). \tag{5.88}$$

where $P_\lambda(z)$ is the Legendre function and z is the angle between the vectors $\boldsymbol{r}$ and $\boldsymbol{R}$. The calculation technique of this integral will be discussed in the next Chapter. Lastly, we use the partial-wave expansion of the plane wave

$$e^{i\boldsymbol{v}\boldsymbol{r}} = 4\pi \sum_{\lambda_1\mu_1}^{\infty} i^{\lambda_1} j_{\lambda_1}(vr) Y^*_{\lambda_1\mu_1}(\widehat{\mathbf{v}}) Y_{\lambda_1\mu_1}(\widehat{\boldsymbol{r}}), \tag{5.89}$$

where $j_\lambda(y)$ is the spherical Bessel function.

With (5.84), (5.87) and (5.89), Exp. (5.83) becomes

$$\begin{aligned}
\tilde{K}^A_{\alpha'\beta} =& 8\pi^2 \sum_{\lambda_1\mu_1}^{\infty} i^{\lambda_1} Y^*_{\lambda_1\mu_1}(\widehat{\mathbf{v}}) \int_0^\infty dr r^2 j_{\lambda_1}(vr) \phi^A_{\alpha'}(r) \\
&\times \sum_{\lambda\mu} g^B_\beta(\lambda, R, r) Y^*_{\lambda\mu}(\widehat{\boldsymbol{R}}) \sum_{\ell_1=0}^{\ell_\beta} \sum_{m_1=-\ell_1}^{\ell_1} (-1)^{\ell_2} (\ell_1 m_1|\ell_\beta m_\beta) r^{\ell_1} R^{\ell_2} Y_{\ell_2 m_2}(\widehat{\boldsymbol{R}}) \\
&\times \int d\hat{\boldsymbol{r}}\ Y_{\lambda\mu}(\hat{\boldsymbol{r}}) Y_{\ell_1 m_1}(\hat{\boldsymbol{r}}) Y^*_{\ell_{\alpha'} m_{\alpha'}}(\hat{\boldsymbol{r}}) Y_{\lambda_1\mu_1}(\hat{\boldsymbol{r}}).
\end{aligned} \tag{5.90}$$

We now evaluate the angular part of $\tilde{K}^A_{\alpha'\beta}(\boldsymbol{R})$,

$$I_\Omega = \int d\hat{\boldsymbol{r}}\ Y_{\lambda\mu}(\hat{\boldsymbol{r}}) Y_{\ell_1 m_1}(\hat{\boldsymbol{r}}) Y^*_{\ell_{\alpha'} m_{\alpha'}}(\hat{\boldsymbol{r}}) Y_{\lambda_1\mu_1}(\hat{\boldsymbol{r}}). \tag{5.91}$$

The first two spherical harmonics in (5.91) are combined

$$Y_{\lambda\mu}(\hat{\boldsymbol{r}}) Y_{\ell_1 m_1}(\hat{\boldsymbol{r}}) = \sum_{LM}^{\lambda+\ell_1} \sqrt{\frac{[\lambda][\ell_1]}{4\pi[L]}} C^{L0}_{\lambda 0\ \ell_1 0} C^{LM}_{\lambda\mu\ \ell_1 m_1} Y_{LM}(\hat{\boldsymbol{r}}). \tag{5.92}$$

Carrying out the angular integration over the product of three spherical harmonics by (2.33), one obtains

$$\begin{aligned} I_\Omega =& \sum_{LM}^{\lambda+\ell_1} \sqrt{\frac{[\lambda][\ell_1]}{4\pi[L]}} C^{L0}_{\lambda 0\ \ell_1 0} C^{LM}_{\lambda\mu\ \ell_1 m_1} \int d\hat{\boldsymbol{r}}\ Y_{LM}(\hat{\boldsymbol{r}}) Y_{\lambda_1\mu_1}(\hat{\boldsymbol{r}}) Y^*_{\ell_{\alpha'} m_{\alpha'}}(\hat{\boldsymbol{r}}) \\ =& \frac{1}{4\pi} \sqrt{\frac{[\lambda][\ell_1][\lambda_1]}{[\ell_{\alpha'}]}} \sum_{LM}^{\lambda+\ell_1} C^{L0}_{\lambda 0\ \ell_1 0} C^{LM}_{\lambda\mu\ \ell_1 m_1} C^{\ell_{\alpha'} 0}_{L0\ \lambda_1 0} C^{\ell_{\alpha'} m_{\alpha'}}_{LM\ \lambda_1\mu_1}. \end{aligned} \tag{5.93}$$

With this result, Exp. (5.90) takes the form

$$\begin{aligned} \tilde{K}^A_{\alpha'\beta}(\boldsymbol{R}) =& 4\pi^{3/2} \sqrt{\frac{[\ell_\beta]!}{[\ell_{\alpha'}]}} \sum_{\lambda\mu}^{\infty} \sqrt{[\lambda]} Y^*_{\lambda\mu}(\widehat{\boldsymbol{R}}) \\ & \times \sum_{\ell_1=0}^{\ell_\beta} \sum_{m_1=-\ell_1}^{\ell_1} (-1)^{\ell_2} \sqrt{\frac{[\ell_1]}{[\ell_1]![\ell_2]!}} C^{\ell_\beta m_\beta}_{\ell_1 m_1\ \ell_2 m_2} \delta_{\ell_1+\ell_2,\ell_\beta} Y_{\ell_2 m_2}(\widehat{\boldsymbol{R}}) R^{\ell_2} \\ & \times \sum_{LM}^{\lambda+\ell_1} C^{L0}_{\lambda 0\ \ell_1 0} C^{LM}_{\lambda\mu\ \ell_1 m_1} \sum_{\lambda_1\mu_1}^{L+\ell_{\alpha'}} i^{\lambda_1} \sqrt{[\lambda_1]} C^{\ell_{\alpha'} 0}_{L0\ \lambda_1 0} C^{\ell_{\alpha'} m_{\alpha'}}_{LM\ \lambda_1\mu_1} Y^*_{\lambda_1\mu_1}(\widehat{\mathbf{v}}) \\ & \times I^{K^A}_{\alpha'\beta}(\lambda, \lambda_1, \ell_1, R), \end{aligned} \tag{5.94}$$

with

$$I^{K^A}_{\alpha'\beta}(\lambda, \lambda_1, \ell_1, R) = \int_0^\infty dr\ g^B_\beta(\lambda, R, r) j_{\lambda_1}(vr) \phi^A_{\alpha'}(r) r^{\ell_1+2}. \tag{5.95}$$

Combining $Y^*_{\lambda\mu}(\widehat{\boldsymbol{R}})$ and $Y_{\ell_2 m_2}(\widehat{\boldsymbol{R}})$ in (5.94) gives

$$\begin{aligned} Y^*_{\lambda\mu}(\widehat{\boldsymbol{R}}) Y_{\ell_2 m_2}(\widehat{\boldsymbol{R}}) =& (-1)^\mu Y_{\lambda-\mu}(\widehat{\boldsymbol{R}}) Y_{\ell_2 m_2}(\widehat{\boldsymbol{R}}) \\ =& (-1)^\mu \sum_{L_1 M_1}^{\lambda+\ell_2} \sqrt{\frac{[\lambda][\ell_2]}{4\pi[L_1]}} C^{L_1 0}_{\lambda 0\ \ell_2 0} C^{L_1 M_1}_{\lambda-\mu\ \ell_2 m_2} Y_{L_1 M_1}(\widehat{\boldsymbol{R}}). \end{aligned} \tag{5.96}$$

At this point significant simplifications arise if we recall that the z axis is chosen to be the direction of the incident proton. In such a case it is easy to show that

$$Y^*_{\lambda_1\mu_1}(\widehat{\mathbf{v}}) = \sqrt{\frac{2\lambda_1+1}{4\pi}} \delta_{\mu_1 0}. \tag{5.97}$$

Carefully examining the Clebsch-Gordan coefficients $C^{\ell_{\alpha'} m_{\alpha'}}_{LM\ \lambda_1\mu_1}$ and $C^{LM}_{\lambda\mu\ \ell_1 m_1}$ together with (5.97), we see that $M = m_{\alpha'}$, $\mu = m_{\alpha'} - m_1$ and $M_1 = m_\beta - m_{\alpha'}$.

Consequently, after some rearranging (5.94) is reduced to

$$\begin{aligned}\tilde{K}^A_{\alpha'\beta}(\boldsymbol{R}) =&\sqrt{\frac{\pi[\ell_\beta]!}{[\ell_{\alpha'}]}}\sum_{\lambda}^{\infty}[\lambda]\sum_{\ell_1=0}^{\ell_\beta}\frac{(-1)^{\ell_2}\delta_{\ell_1+\ell_2,\ell_\beta}}{\sqrt{(2\ell_1)!(2\ell_2)!}}R^{\ell_2}\sum_{L_1}^{\lambda+\ell_2}\frac{C^{L_10}_{\lambda0\ \ell_20}}{\sqrt{[L_1]}}Y_{L_1M_1}(\widehat{\boldsymbol{R}})\sum_{L}^{\lambda+\ell_1}C^{L0}_{\lambda0\ \ell_10}\\ &\times\sum_{\lambda_1}^{L+\ell_{\alpha'}}i^{\lambda_1}[\lambda_1]C^{\ell_{\alpha'}0}_{L0\ \lambda_10}C^{\ell_{\alpha'}m_{\alpha'}}_{Lm_{\alpha'}\ \lambda_10}I^{G^A}_{\alpha'\beta}(\lambda,\lambda_1,\ell_1,R)\\ &\times\sum_{m_1=-\ell_1}^{\ell_1}(-1)^{\mu}C^{\ell_\beta m_\beta}_{\ell_1m_1\ \ell_2m_2}C^{L_1M_1}_{\lambda-\mu\ \ell_2m_2}C^{Lm_{\alpha'}}_{\lambda\mu\ \ell_1m_1}.\end{aligned}\tag{5.98}$$

In the last formula the sum of the product of three Clebsch-Gordan coefficients is expressed by $6j$-symbol and eventually Exp. (5.98) takes the form

$$\begin{aligned}\tilde{K}^A_{\alpha'\beta}(\boldsymbol{R}) =&(-1)^{\ell_\beta}\sqrt{\frac{\pi[\ell_\beta]!}{[\ell_{\alpha'}]}}\sum_{\lambda}^{\infty}[\lambda]\sum_{\ell_1=0}^{\ell_\beta}\frac{\delta_{\ell_1+\ell_2,\ell_\beta}}{\sqrt{(2\ell_1)!(2\ell_2)!}}R^{\ell_2}\sum_{L_1}^{\lambda+\ell_2}C^{L_10}_{\lambda0\ \ell_20}Y_{L_1M_1}(\widehat{\boldsymbol{R}})\\ &\times\sum_{L}^{\lambda+\ell_1}(-1)^L\sqrt{[L]}C^{L0}_{\lambda0\ \ell_10}\sum_{\lambda_1}^{L+\ell_{\alpha'}}i^{\lambda_1}[\lambda_1]C^{\ell_{\alpha'}0}_{L0\ \lambda_10}C^{\ell_{\alpha'}m_{\alpha'}}_{Lm_{\alpha'}\ \lambda_10}I^{G^A}_{\alpha'\beta}(\lambda,\lambda_1,\ell_1,R)\\ &\times C^{\ell_\beta m_\beta}_{Lm_{\alpha'}\ L_1M_1}\begin{Bmatrix}\lambda & \ell_1 & L\\ \ell_\beta & L_1 & \ell_2\end{Bmatrix}.\end{aligned}\tag{5.99}$$

Changing the orders of summations over λ and L_1, we arrive at the final expression for this matrix element

$$\begin{aligned}\tilde{K}^A_{\alpha'\beta}(\boldsymbol{R}) =&(-1)^{\ell_\beta}\sqrt{\frac{\pi[\ell_\beta]!}{[\ell_{\alpha'}]}}\sum_{\lambda=|q|}^{\infty}Y_{\lambda q}(\widehat{\boldsymbol{R}})\sum_{\ell_1=0}^{\ell_\beta}\frac{\delta_{\ell_1+\ell_2,\ell_\beta}}{\sqrt{(2\ell_1)!(2\ell_2)!}}R^{\ell_2}\sum_{L_1=|\lambda-\ell_2|}^{\lambda+\ell_2,2}C^{\lambda0}_{L_10\ \ell_20}[L_1]\\ &\times\sum_{L=\max(|L_1-\ell_1|,|\lambda-\ell_\beta|)}^{\min(L_1+\ell_1,\lambda+\ell_\beta),2}(-1)^L\sqrt{[L]}C^{L0}_{L_10\ \ell_10}C^{\ell_\beta m_\beta}_{Lm_{\alpha'}\ \lambda q}\begin{Bmatrix}L_1 & \ell_1 & L\\ \ell_\beta & \lambda & \ell_2\end{Bmatrix}\\ &\times\sum_{\lambda_1=|L-\ell_{\alpha'}|}^{L+\ell_{\alpha'},2}i^{\lambda_1}[\lambda_1]C^{\ell_{\alpha'}0}_{L0\ \lambda_10}C^{\ell_{\alpha'}m_{\alpha'}}_{Lm_{\alpha'}\ \lambda_10}I^{K^A}_{\alpha'\beta}(L_1,\lambda_1,\ell_1,R),\end{aligned}\tag{5.100}$$

with $I^{K^A}_{\alpha'\beta}(L_1,\lambda_1,\ell_1,R)$ given by (5.95), and $q=m_\beta-m_{\alpha'}$.

The corresponding expression for the matrix element $\tilde{P}^A_{\alpha'\beta}(\boldsymbol{R})$ is

$$\begin{aligned}\tilde{P}^A_{\alpha'\beta}(\boldsymbol{R}) =&(-1)^{\ell_\beta}\sqrt{\frac{\pi[\ell_\beta]!}{[\ell_{\alpha'}]}}\sum_{\lambda=|q|}^{\infty}Y_{\lambda q}(\widehat{\boldsymbol{R}})\sum_{\ell_1=0}^{\ell_\beta}\frac{\delta_{\ell_1+\ell_2,\ell_\beta}}{\sqrt{(2\ell_1)!(2\ell_2)!}}R^{\ell_2}\sum_{L_1=|\lambda-\ell_2|}^{\lambda+\ell_2,2}C^{\lambda 0}_{L_1 0\ \ell_2 0}[L_1]\\ &\times\sum_{L=\max(|L_1-\ell_1|,|\lambda-\ell_\beta|)}^{\min(L_1+\ell_1,\lambda+\ell_\beta),2}(-1)^L\sqrt{[L]}C^{L0}_{L_1 0\ \ell_1 0}C^{\ell_\beta m_\beta}_{Lm_{\alpha'}\ \lambda q}\begin{Bmatrix}L_1 & \ell_1 & L\\ \ell_\beta & \lambda & \ell_2\end{Bmatrix}\\ &\times\sum_{\lambda_1=|L-\ell_{\alpha'}|}^{L+\ell_{\alpha'},2}i^{\lambda_1}[\lambda_1]C^{\ell_{\alpha'}0}_{L0\ \lambda_1 0}C^{\ell_{\alpha'}m_{\alpha'}}_{Lm_{\alpha'}\ \lambda_1 0}I^{PA}_{\alpha'\beta}(L_1,\lambda_1,\ell_1,R),\end{aligned}\tag{5.101}$$

with

$$I^{PA}_{\alpha'\beta}(\lambda,\lambda_1,\ell_1,R)=\int_0^\infty dr\ g^B_\beta(\lambda,R,r)j_{\lambda_1}(vr)\phi^A_{\alpha'}(r)r^{\ell_1+1}.\tag{5.102}$$

In other words, the only difference in the expressions for $\tilde{K}^A_{\alpha'\beta}(\boldsymbol{R})$ and $\tilde{P}^A_{\alpha'\beta}(\boldsymbol{R})$ is the radial integrals, $I^{KA}_{\alpha'\beta}(\lambda,\lambda_1,\ell_1,R)$ and $I^{PA}_{\alpha'\beta}(\lambda,\lambda_1,\ell_1,R)$. Consequently, these two matrix elements can be evaluated simultaneously.

The other set of matrix elements are calculated by

$$\begin{aligned}\tilde{K}^B_{\beta'\alpha}(\boldsymbol{R}) =&\sqrt{\frac{\pi[\ell_\alpha]!}{[\ell_{\beta'}]}}\sum_{\lambda=|q|}^{\infty}Y_{\lambda q}(\widehat{\boldsymbol{R}})\sum_{\ell_1=0}^{\ell_\alpha}\frac{(-1)^{\ell_1}\delta_{\ell_1+\ell_2,\ell_\alpha}}{\sqrt{(2\ell_1)!(2\ell_2)!}}R^{\ell_2}\sum_{L_1=|\lambda-\ell_2|}^{\lambda+\ell_2,2}C^{\lambda 0}_{L_1 0\ \ell_2 0}[L_1]\\ &\times\sum_{L=\max(|L_1-\ell_1|,|\lambda-\ell_\alpha|)}^{\min(L_1+\ell_1,\lambda+\ell_\alpha),2}(-1)^L\sqrt{[L]}C^{L0}_{L_1 0\ \ell_1 0}C^{\ell_\alpha m_\alpha}_{Lm_{\beta'}\ \lambda q}\begin{Bmatrix}L_1 & \ell_1 & L\\ \ell_\alpha & \lambda & \ell_2\end{Bmatrix}\\ &\times\sum_{\lambda_1=|L-\ell_{\beta'}|}^{L+\ell_{\beta'},2}(-i)^{\lambda_1}[\lambda_1]C^{\ell_{\beta'}0}_{L0\ \lambda_1 0}C^{\ell_{\beta'}m_{\beta'}}_{Lm_{\beta'}\ \lambda_1 0}I^{KB}_{\beta'\alpha}(L_1,\lambda_1,\ell_1,R),\end{aligned}\tag{5.103}$$

$$\begin{aligned}\tilde{P}^B_{\beta'\alpha}(\boldsymbol{R}) =&\sqrt{\frac{\pi[\ell_\alpha]!}{[\ell_{\beta'}]}}\sum_{\lambda=|q|}^{\infty}Y_{\lambda q}(\widehat{\boldsymbol{R}})\sum_{\ell_1=0}^{\ell_\alpha}\frac{(-1)^{\ell_1}\delta_{\ell_1+\ell_2,\ell_\alpha}}{\sqrt{(2\ell_1)!(2\ell_2)!}}R^{\ell_2}\sum_{L_1=|\lambda-\ell_2|}^{\lambda+\ell_2,2}C^{\lambda 0}_{L_1 0\ \ell_2 0}[L_1]\\ &\times\sum_{L=\max(|L_1-\ell_1|,|\lambda-\ell_\alpha|)}^{\min(L_1+\ell_1,\lambda+\ell_\alpha),2}(-1)^L\sqrt{[L]}C^{L0}_{L_1 0\ \ell_1 0}C^{\ell_\alpha m_\alpha}_{Lm_{\beta'}\ \lambda q}\begin{Bmatrix}L_1 & \ell_1 & L\\ \ell_\alpha & \lambda & \ell_2\end{Bmatrix}\\ &\times\sum_{\lambda_1=|L-\ell_{\beta'}|}^{L+\ell_{\beta'},2}(-i)^{\lambda_1}[\lambda_1]C^{\ell_{\beta'}0}_{L0\ \lambda_1 0}C^{\ell_{\beta'}m_{\beta'}}_{Lm_{\beta'}\ \lambda_1 0}I^{PB}_{\beta'\alpha}(L_1,\lambda_1,\ell_1,R),\end{aligned}\tag{5.104}$$

with

$$I^{K^B}_{\beta'\alpha}(\lambda,\lambda_1,\ell_1,R) = \int_0^\infty dr\ g^A_\alpha(\lambda,R,r) j_{\lambda_1}(vr)\phi^B_{\beta'}(r) r^{\ell_1+2}, \tag{5.105}$$

$$I^{P^B}_{\beta'\alpha}(\lambda,\lambda_1,\ell_1,R) = \int_0^\infty dr\ g^A_\alpha(\lambda,R,r) j_{\lambda_1}(vr)\phi^B_{\beta'}(r) r^{\ell_1+1}, \tag{5.106}$$

$$g^A_\alpha(\lambda,R,r) = \int_{-1}^{1} dz \frac{\phi^A_\alpha(|\boldsymbol{r}+\boldsymbol{R}|)}{|\boldsymbol{r}+\boldsymbol{R}|^{\ell_\alpha}} P_\lambda(z), \tag{5.107}$$

and $q = m_\alpha - m_{\beta'}$.

All final expressions for the exchange matrix elements can be written as

$$\tilde{W}(\boldsymbol{R}) = \sum_{\lambda=|q|}^{\infty} Y_{\lambda q}(\widehat{\boldsymbol{R}}) f_\lambda(R), \tag{5.108}$$

where $\tilde{W}(\boldsymbol{R})$ is any exchange matrix element and $f_\lambda(R)$ stands for the inner four summations. This allows us to calculate $f_\lambda(R)$ in a fine mesh of R for all possible combinations of initial and final states. Then the required value of the matrix elements are simply obtained by interpolation. This is in sharp contrast to the common way of treating charge exchange matrix elements in the prolate spheroidal coordinates [12, 90], where one has to calculate them at each impact parameter along the integration axis.

5.5 Chapter summary

In this Chapter we have described in detail a new semi-classical close-coupling approach. In the method we expanded the total wave function in terms of the asymptotic form of the scattering wave function (about each centre) and substitute it into the total Schrödinger equation. Then under relevant semi-classical approximations we obtained coupled channel differential equations for the expansion coefficients. The PWETF appear in the matrix elements from our derivations in systematic and mathematically rigorous way. While in traditional

close-coupling methods, based on the prescription of Bates, two-centre electronic wave function is expanded as combination of atomic functions with the attached PWETF [12, 56]. And the necessity of the PWETF has been controversial for some time in ion-atom collisions theory [56, 193].

In addition to the fundamental aspect described above, we proposed a different numerical technique for evaluating exchange matrix elements. Comparing the expressions for the direct (for example, Eq. (5.72)) and exchange matrix elements Eq. (5.108), one can see that they are basically of the same form. The only difference being that in the case of the exchange matrix elements the upper limit of the summation is infinite. In practical calculations this summation will be limited by $\lambda_{\max}$. Moreover, the matrix elements can be calculated as a function of the internuclear distance, R. While solving the system of differential equations the required values of the matrix elements are found by interpolation. This result can be considered as an advantage over the most commonly used way of evaluating exchange matrix elements in the prolate spheroidal coordinates [12, 194], in which the impact parameter (b) and the integration variable (Z) are not separable and one has to evaluate a two-dimensional integral on the (b, Z) grid. Choice of $\lambda_{\max}$ and the other numerical parameters that influence the accuracy of the matrix elements will be discussed in the next Chapter.

Chapter 6

Proton-hydrogen collisions

In this Chapter we give an application of the proposed two-centre semi-classical CC method to the p-H($1s$) system. Before going to larger scale calculations we do several tests. As noted before, the direct matrix elements are relatively simple and they have been tested in Chapter 2 for antiproton collisions with atomic hydrogen. In contrast, the exchange matrix elements have a fairly complex form. Therefore, we start with the discussion of the numerical methods that will be used in the evaluation of the exchange matrix elements. In order to test the code, the first Born approximation results and coupled-channel calculations with few eigenstates will be compared with the corresponding results in the literature. Then we proceed to larger calculations with asymmetric and symmetric treatments of two-centres.

6.1 Details of calculations

6.1.1 Calculation of the angular integrations

In order to do accurate calculations it is essential to be able to evaluate the angular integration (Eqs. (5.88) and (5.107)) to a high precision for a wide range

of the variables r and R. Note that these integrands do not have a singularity, as the denominator is cancelled with the same factor available in the basis functions (2.25). However, for some values of the variables r and R the integrand becomes highly peaked at the end point of the integration.

For the calculation of this integral, we have found that the tanh-sinh quadrature rule [195] suits best. The tanh-sinh quadrature is used to approximately calculate integrals of the form $\int_{-1}^{1} f(z)\, dz$, where the integrand has singularities or infinite derivatives at the end points. This rule is based on the change of variable

$$z = \tanh\left(\frac{\pi}{2}\sinh(t)\right), \tag{6.1}$$

which transforms the integral on the interval $z \in (-1, +1)$ to the one on the entire real line $t \in (-\infty, +\infty)$. After this transformation, the integrand decays with a double-exponential rate. Therefore, this method is also known as the double-exponential formula. For a given step size h, the integral is approximated as a sum

$$\int_{-1}^{1} f(z)\, dz \approx \sum_{k=-\infty}^{\infty} \omega_k f(z_k), \tag{6.2}$$

with the abscissas

$$z_k = \tanh\left(\frac{\pi}{2}\sinh(kh)\right), \tag{6.3}$$

and weights

$$\omega_k = \frac{h\pi\cosh(kh)/2}{\cosh^2\left(\pi\sinh(kh)/2\right)}. \tag{6.4}$$

In practice the summation in (6.2) is limited to $[-N_z, N_z]$. In the calculations the value of the step size is set to $h = 2^{-4}$.

6.1.2 Integration of the coupled equations

The system of the first order differential equations (5.59) is solved, subject to initial conditions (5.62), in the range $(-Z_{\max}, Z_{\max})$ by an adaptive step size

solver. The idea behind this solver is similar to the one in the method of Hamming [196]. This equation solver works by comparing the results obtained by the 4th order Runge-Kutta and 5th order Runge-Kutta-Butcher [197] methods. The solver starts solving the system of the first order differential equations with some trial step size. This step size varies automatically during the computation. At each step the length of the error vector (defined as the difference of the results from the Runge-Kutta and Runge-Kutta-Butcher methods), is compared with two limits ϵ_1 and ϵ_2, where $\epsilon_1 < \epsilon_2$. If this deviation is less than ϵ_1, then the step size will be doubled. If it exceeds ϵ_2, the step size will be halved in the next step.

6.1.3 Numerical parameters

There are several numerical parameters that have an effect on the results. Below the choice of these parameters is discussed.

The radial integrations of both the direct and exchange matrix elements are performed by Simpson's rule. The calculation of the direct matrix elements has been considered in Chapter 2 in the case of the antiproton scattering on hydrogen. The only difference between radial integrations of the direct and exchange matrix elements is the presence of the spherical Bessel functions in the latter. Hence, the number of integration points is increased to make sure that radial integrations of the exchange matrix elements are calculated accurately.

The accuracy of the angular integrations (Eqs. (5.88) and (5.107)), carried out by the tanh-sinh quadrature, has been tested by increasing parameter N_z to 60. In the calculations the usual value of N_z is 40. The limit of the summation in the exchange matrix elements (see Eq. (5.108)), $\lambda_{\max}$, will be determined by performing Born type calculations. However, the value of this parameter will be

increased as necessary while doing fully coupled calculations.

The other parameters are related to the solution of the coupled differential equations. The coupled equations have been integrated using the chosen lower and upper truncation error limits, $\epsilon_1 = 10^{-8}$ and $\epsilon_2 = 10^{-6}$. Then the equations are solved again using ϵ_1 and ϵ_2 one-tenth as large. Another parameter is the upper limit of Z, $Z_{\max}$, used to solve the differential equations. In the full calculations $Z_{\max}$ is chosen to be 125.

Finally, the number of the impact parameter points used to calculate cross sections (Eqs. (5.65), (5.66)) was 60. We used the Gauss-Legendre quadrature rule in the range $(0, b_{\max})$ where, typically, $b_{\max} = 10$. These parameters have been increased, where necessary. For example, at lower impact energies the electron transfer channel probabilities become oscillatory, or at higher energies the excitation probabilities are of longer range. In order to make sure that the cross sections corresponding to these probabilities are accurately calculated 150 Gauss-Legendre points and $b_{\max} = 20$ have been used in the calculations.

6.2 Born results

Electron transfer problem in proton collisions has been solved in [198] using the true eigenstates and within the on-shell approximation. In addition, in [198] only Brinkmann-Kramers (BK) term has been included. The matrix element given by (5.77) corresponds to this term. In order to be able to compare the effective potentials, in our code (written for pseudostates) we can construct our basis in such a way that the lowest pseudostates represent the exact hydrogenic eigenstates. This is done by taking a sufficiently large basis size and using the lowest pseudostates in the calculations. The exponential cut-off parameter of the Laguerre functions is set to $\lambda_l = 1$. For example, when the basis size is

40, $n = 4$ eigenstates are well reproduced. Therefore, as a first important test we have compared the impact parameter dependence of the BK amplitude for all possible combinations of the transitions involving up to $n = 4$ eigenstates. From this test we determine a practical upper limit of the summation $\lambda_{\max}$ in Eq. (5.108). We have observed that the summation converges rapidly and the main contribution comes from the first 10 terms. An excellent agreement of the BK effective potentials from the method used in [198] and our method has been obtained with $\lambda_{\max} = 20$.

To validate the calculation method for the exchange matrix elements, we have calculated the Born cross sections for p-H($1s$), taking into account both the BK and Jackson-Schiff (JS) interactions and compared with those from Belkić [199]. We give this comparison in Table 6.1. As can be seen from the table almost one-to-one agreement is achieved. However, a small discrepancy has been observed at higher impact energies. This could be due to the fact that these results are obtained from the pseudostate code, not from the eigenstate one. Also, it is worthwhile to mention that the Born cross sections are obtained from the general two-centre code. This serves as a necessary (but not sufficient) check of the correct inclusion of the BK and JS interactions. In the next section the tests of channel coupling with limited number of eigenstates will be discussed.

6.3 Coupled calculations with eigenstates

Lovell and McElroy [200] carried out (2+1) and (1+2) coupled calculations with different combinations of $1s$ and $2s$ hygrogenic states retained in target and projectile centres. The authors tabulated excitation and electron capture cross sections for several energies. We have very good agreement with their tabulated data, except for a single case. This is the cross section for the excitation to $2s$

Table 6.1: Born cross sections (in units of cm^2) for electron capture by p from H($1s$). For comparison the results of Belkić [199] are given. The first row is Belkić's results, while the second one is the present calculations. Notation $X[-N]$ means $X \times 10^{-N}$.

Final	Energy (keV)						
state	20	30	50	100	200	500	1000
$1s$	3.01[-16]	1.42[-16]	4.57[-17]	6.45[-18]	5.26[-19]	8.80[-20]	2.57[-22]
	3.01[-16]	1.42[-16]	4.58[-17]	6.46[-18]	5.27[-19]	8.83[-20]	2.58[-22]
$2s$	3.69[-16]	1.97[-17]	6.92[-18]	1.02[-18]	8.12[-20]	1.25[-21]	3.47[-23]
	3.69[-16]	1.97[-17]	6.94[-18]	1.03[-18]	8.14[-20]	1.25[-21]	3.47[-23]
$2p$	5.37[-17]	2.86[-17]	8.87[-18]	8.42[-19]	3.57[-20]	2.18[-22]	2.97[-24]
	5.38[-17]	2.86[-17]	8.89[-18]	8.44[-19]	3.58[-20]	2.19[-22]	2.98[-24]
$3s$	1.03[-17]	5.89[-18]	2.14[-18]	3.18[-19]	2.51[-20]	3.79[-22]	1.03[-23]
	1.03[-17]	5.90[-18]	2.14[-18]	3.19[-19]	2.51[-20]	3.81[-22]	1.04[-23]
$3p$	1.39[-17]	8.21[-18]	2.84[-18]	2.92[-19]	1.27[-20]	7.78[-23]	1.05[-24]
	1.39[-17]	8.22[-18]	2.84[-18]	2.93[-19]	1.27[-20]	7.81[-23]	1.06[-24]
$3d$	3.38[-18]	1.58[-18]	4.36[-19]	3.01[-20]	7.56[-22]	1.97[-24]	1.35[-26]
	3.38[-18]	1.58[-18]	4.37[-19]	3.02[-20]	7.60[-22]	1.99[-24]	1.36[-26]
$4s$	4.22[-18]	2.48[-18]	9.13[-19]	1.37[-19]	1.07[-20]	1.64[-22]	4.38[-24]
	4.22[-18]	2.49[-18]	9.15[-19]	1.37[-19]	1.08[-20]	1.62[-22]	4.42[-24]
$4p$	5.55[-18]	3.40[-18]	1.22[-18]	1.29[-19]	5.67[-21]	3.47[-22]	4.68[-25]
	5.55[-18]	3.40[-18]	1.23[-18]	1.30[-19]	5.69[-21]	3.49[-22]	4.72[-25]
$4d$	1.78[-18]	8.58[-19]	2.46[-19]	1.77[-20]	4.52[-22]	1.19[-24]	8.12[-27]
	1.79[-18]	8.59[-19]	2.47[-19]	1.78[-20]	4.54[-22]	1.19[-24]	8.20[-27]
$4f$	1.04[-19]	4.43[-20]	1.10[-20]	5.67[-22]	8.73[-24]	1.01[-26]	3.51[-29]
	1.04[-19]	4.42[-20]	1.10[-20]	5.69[-22]	8.78[-24]	1.02[-26]	3.56[-29]

state at 12.5 keV energy for the case where $1s$ and $2s$ for the projectile and $1s$ for the target centres are retained. For this transition Lovell and McElroy [200] gave 7.53×10^{-18} cm^2, while our calculations produce 5.75×10^{-18} cm^2. However, we get a perfect agreement at the other reported collision energies. The fact that the same coupled calculation yields the correct result for the capture to $1s$ channel suggests that there could be a misprint in [200].

Calculations with five ($1s$, $2s$, $2p_0$ and $2p_{\pm1}$) eigenstates reported by Cheshire [72]

and Rapp and Dinwiddie [76] could serve as another test. These two papers give excitation and capture cross sections for all channels in tabulated form. There are eight common incident energies in these two works. Comparing the cross sections (at common incident energies reported) from our calculations with those by Cheshire [72] and Rapp and Dinwiddie [76], we conclude that our results agree well with the results by Rapp and Dinwiddie [76]. However, there are some discrepancies to consider. For example, at E=20 keV we get for $1s$ capture 4.149×10^{-16} cm^2, whereas Rapp and Dinwiddie [76] gave 4.080×10^{-16} cm^2. While at the same energy there is a different picture for $2p$ excitation channel: we have a value of 0.206×10^{-16} cm^2 in contrast to their 0.217×10^{-16} cm^2. We have tested our results by increasing the numerical parameters: $\lambda_{\max}, Z_{\max}, N_z$ and the radial mesh points. Also, the unitarity condition (Eq. (5.61)) of the wave function has been calculated along the integration path. The deviation from unity is always less than 10^{-4} for all energies and impact parameters.

Lastly, we compare with the results of Winter and Lin [201]. In this paper the authors performed calculations with $1s$ in the target centre and ($1s$, $2s$, $2p_0$ and $2p_{\pm1}$) states in the projectile centre and gave $2s$ and $2p$ capture cross sections at $E = 25$ and 100 keV. Our results agree with those by Winter and Lin [201] within 2%. The performed tests validate both the theoretical method and the fortran code written based on it.

6.4 Full two-centre close-coupling calculations

6.4.1 Convergence studies

Two types of expansions are commonly employed in the two-centre close-coupling calculations. The first one is the full two-centre expansion in which the same pseudocontinuum states are used on both centres. We call this a symmetric expansion. In the second type of expansion the pseudocontinuum states are retained on either the projectile or target centre only. We call this an asym-

metric expansion. Toshima [89] performed calculations based on both types of expansions and obtained consistent ionisation cross sections. While Kuang and Lin [50] used asymmetric expansions in their calculations.

As a first application of the developed semi-classical close-coupling method an asymmetric type of calculations have been performed. The diagonalisation of the atomic Hamiltonian yields a set of pseudostates. In the current calculations all the generated states are included in the target centre, while only the negative energy states are retained in the projectile centre. We emphasize that no further truncation of the basis has been performed. In the following the number of states on each centre is used to classify the basis. For example, the diagonalisation of the atomic Hamiltonian with ($l_{\max} = 4$, $n_{\max} = 21$) gives 95 nl-states. In the nlm notation (including all m with $|m| \leq l_{\max}$) this corresponds to 455 states and 71 of them are of negative energy. Therefore, we call this basis T455P71. With ($l_{\max} = 5$, $n_{\max} = 20$) and ($l_{\max} = 5$, $n_{\max} = 21$) we get T595P75 and T631P82, respectively.

We have performed a series of asymmetric calculations in the energy interval between 5 keV and 1 MeV with increasing $l_{\max}$ and $n_{\max}$. In Figure 6.1 we plot the total ionisation cross section (TICS) obtained including a large number of pseudostates with $l_{\max} = 5$ and $n_{\max} = 18, 19, 20, 21$. This figure shows that the TICS is very well converged at fixed $l_{\max}$ with increasing $n_{\max}$. To be specific, at $E = 50$ keV the difference of the TICS between T595P75 and T631P82 is only about 1%. The calculations with $l_{\max} = 0 - 4$ have also been performed and similar good convergence with $n_{\max}$ has been observed. Figure 6.2 displays the TICS for different $l_{\max}$ at fixed $n_{\max} = 21$. These results have been obtained with the parameters $\lambda_{\max} = 25$ and $Z_{\max} = 125$. Calculations with $\lambda_{\max} = 30$, $Z_{\max} = 150$ and 175 have also been carried out to make sure the results do not depend on them.

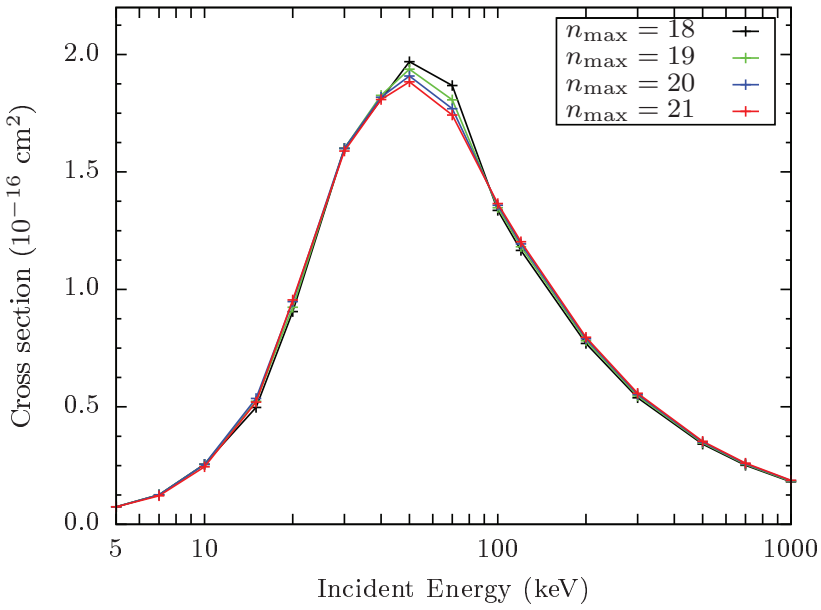

Figure 6.1: The total ionisation cross section for the p-H($1s$) collisions with $n_{\max} = 18, 19, 20$ and 21 at fixed $l_{\max} = 5$.

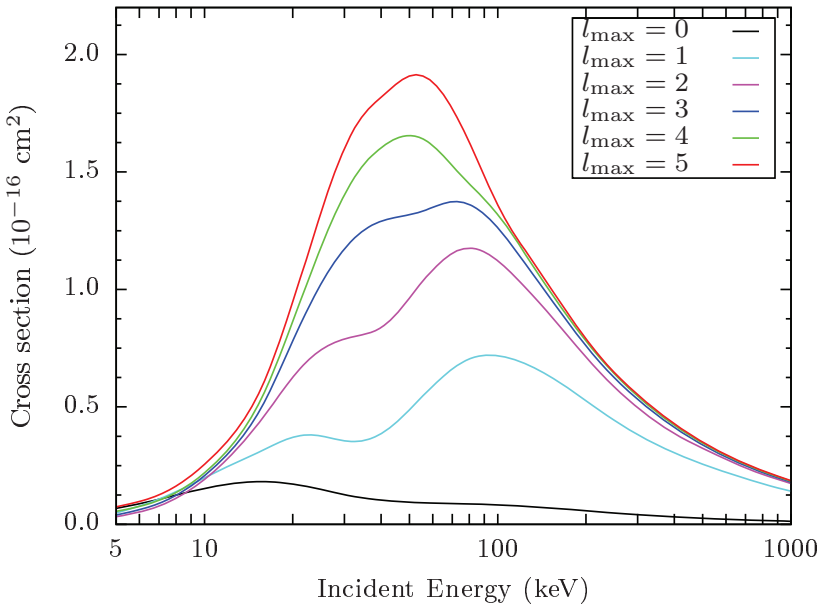

Figure 6.2: The total ionisation cross section for the p-H($1s$) collisions with increasing $l_{\max}$ at fixed $n_{\max} = 21$.

6.4.2 Excitation and electron capture to 2s and 2p states

In Figures 6.3-6.6 we compare our 2s and 2p excitation and capture cross section with those from various calculations and experiments. The agreement with the calculations of Winter [90], the most recent work on the subject, is very good. However, detailed comparison with Winter's 220 state Sturmian function calculations (Table V in [90]) reveals that there are some discrepancies. These are clearly noticeable at energies 8 and 25 keV. In the 2s excitation cross sections (Figure 6.3), the disagreement at these energies are about 13% and 16%, respectively. While in the case of excitation to the 2p state the discrepancies are 5% and 12%, respectively. Interestingly, our cross sections for electron capture to 2p level agree very well with those by Winter [90] at all tabulated energies.

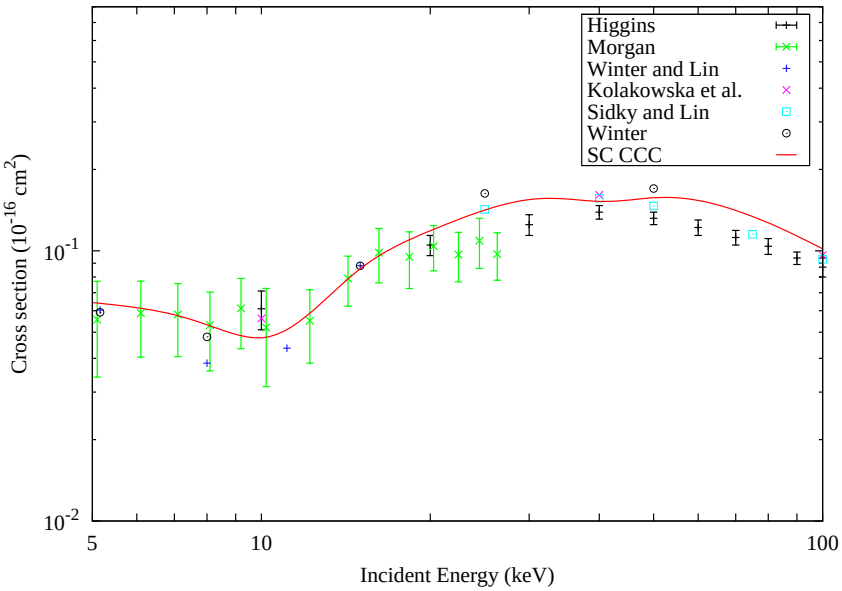

Figure 6.3: The cross section for excitation to the 2s state for the p-H(1s) collisions. Experimental results of Higgins *et al.* [49] and Morgan *et al.* [202] as well as the theoretical calculations by Winter and Lin [94], Kolakowska *et al.* [47], Sidky and Lin [203] and Winter [90] are shown. The present SC CCC results are shown by a red solid line. Experimental results are given with error bars, while symbols indicate the theoretical calculations.

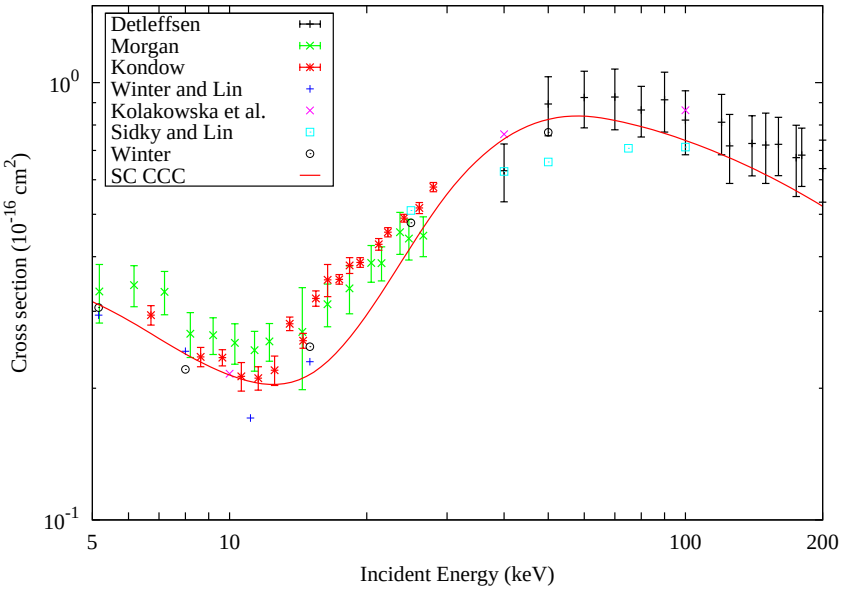

Figure 6.4: The cross section for excitation to the $2p$ state for the p-H($1s$) collisions. Experimental results are due to Detleffsen *et al.* [85], Morgan *et al.* [202] and Kondow *et al.* [204]. Theoretical calculations are as described in Figure 6.3.

Also shown are the lattice-based Fourier collocation method cross sections by Kolakowska *et al.* [47]. Comparison of our results with those by Kolakowska *et al.* [47] at energies 10, 40 and 100 keV shows good agreement. The exceptions are at 100 keV for excitation to the $2p$ and at 40 keV for electron capture to the $2s$ state. Relatively worse agreement is observed with the calculations from the two-centre momentum-space discretization method of Sidky and Lin [203]. Significant differences in $2p$ excitation and $2s$ capture cross sections are visible almost at all five energies given by Sidky and Lin [203]. 36 state triple-centre results of Winter and Lin [205] (at E=8, 11.11 and 15 keV) are also displayed in Figures 6.3-6.6. Overall agreement with the calculations of Winter and Lin [205] is rather bad. For example, for $2s$ excitation (Figure 6.3) at 8 keV the discrepancy is almost 40%. This gets even worse for $2p$ excitation channel at E=11.11 keV.

We now turn to the comparison with experimental data. For the $2s$ excita-

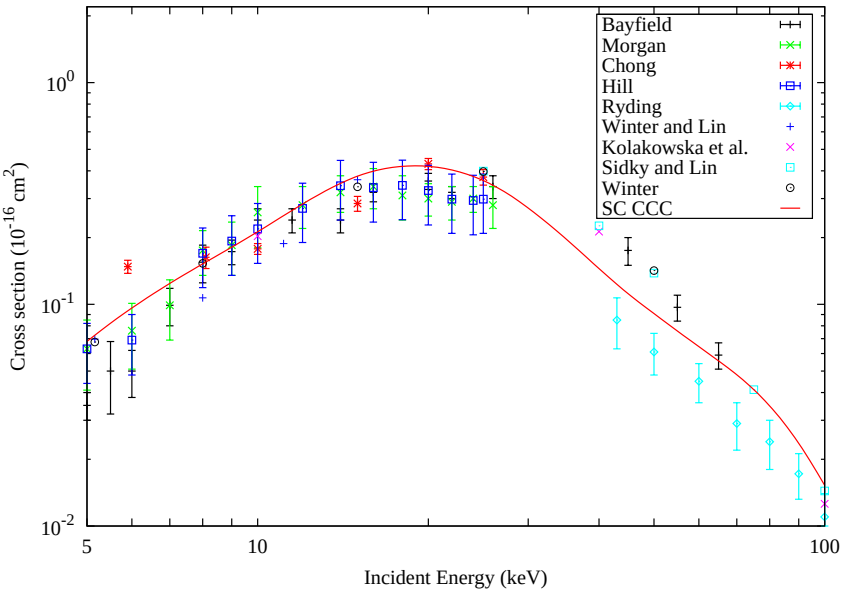

Figure 6.5: The cross section for electron transfer to the $2s$ state for the p-H($1s$) collisions. Experimental results are due to Bayfield *et al.* [206], Chong *et al.* [207], Hill *et al.* [208], Morgan *et al.* [202] and Ryding *et al.* [209]. Theoretical calculations are as described in Figure 6.3.

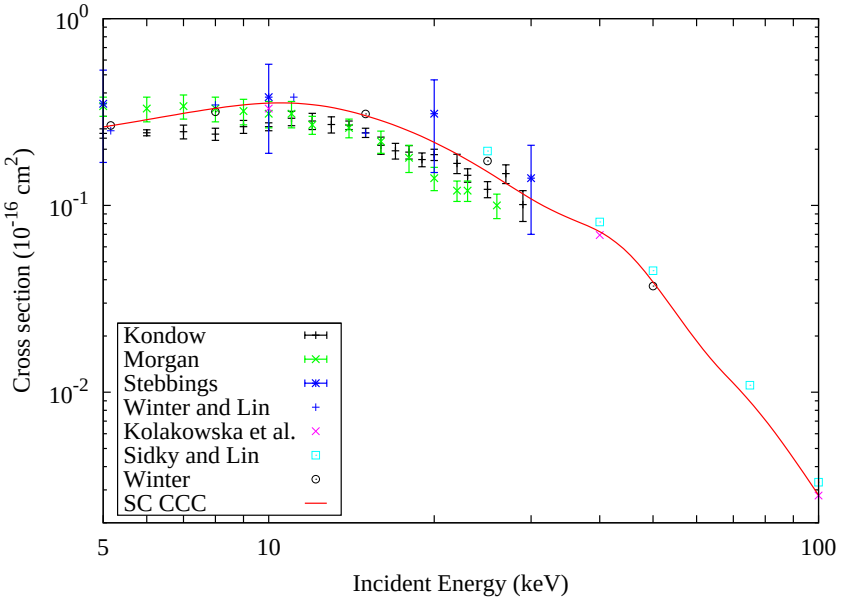

Figure 6.6: The cross section for electron transfer to the $2p$ state for the p-H($1s$) collisions. Experimental results are due to Kondow *et al.* [204], Morgan *et al.* [202] and Stebbings *et al.* [210]. Theoretical calculations are as described in Figure 6.3.

tion (Figure 6.3), in the range 5-15 keV there is an excellent agreement with the experimental values of Morgan *et al.* [202]. But at higher energies our results lie slightly above the experimental data of Higgins *et al.* [49]. As it is seen from Figure 6.4, the $2p$ excitation cross section is in good agreement with the experiment except for the region 15-25 keV. At higher energies our cross sections are within the error bars of the data by Detleffsen *et al.* [85]. Regarding electron transfer to the $2s$ state (Figure 6.5), our cross sections are in accord with the experimental data of Bayfield *et al.* [206], Chong *et al.* [207], Hill *et al.* [208] and Morgan *et al.* [202]. But in the 40-100 keV energy interval our results are located between the values given by Bayfield *et al.* [206] and Ryding *et al.* [209]. Comparison of the calculated $2p$ electron-transfer cross section in Figure 6.6 shows a good agreement with the experiment of Kondow *et al.* [204], Morgan *et al.* [202] and Stebbings *et al.* [210]. Figures 6.7-6.8 show the impact parameter dependence of the $2s$, $2p$ excitation and capture probabilities at E=20 keV.

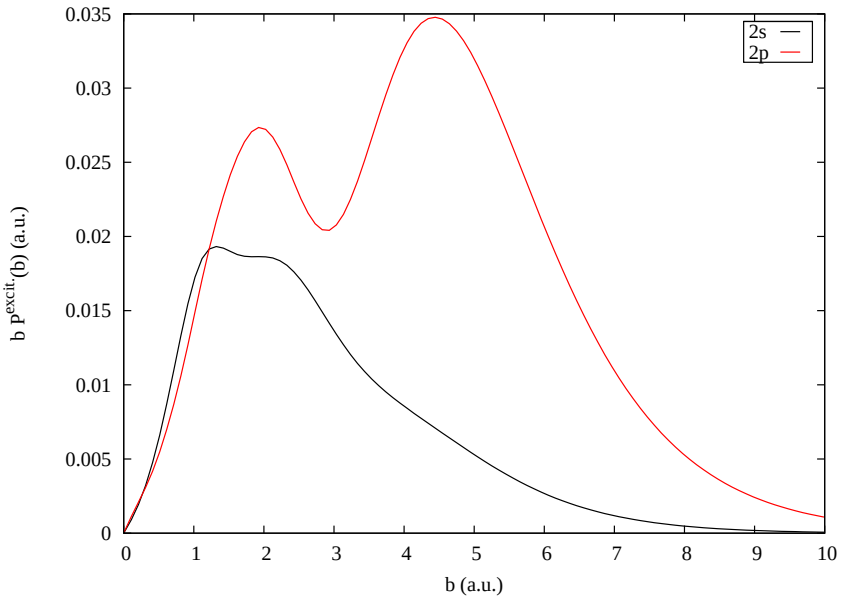

Figure 6.7: Impact-parameter dependencies of the weighted $2s$ and $2p$ excitation probabilities at incident energy $E = 20$ keV.

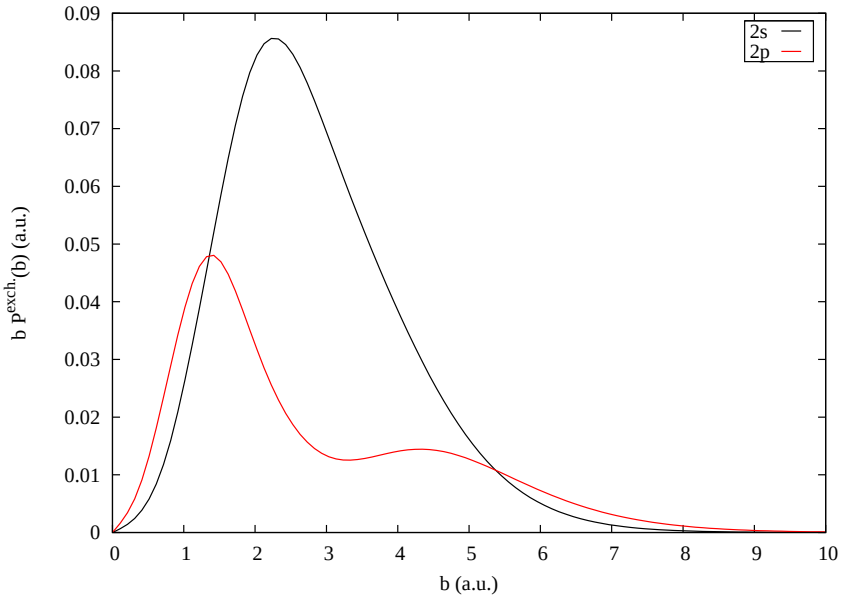

Figure 6.8: Impact-parameter dependencies of the weighted $2s$ and $2p$ electron capture probabilities at incident energy $E = 20$ keV.

6.4.3 Total electron capture

In Figure 6.9 the total electron-transfer cross section calculated in the CCC approach is compared with experimental data and the other calculations. Like in the case of excitation and capture into $2s$ and $2p$ states, electron-transfer cross section is in excellent agreement with the tabulated data of Winter [90]. From Figure 6.9 we see that there is a small discrepancy at 25 keV. At this point the current semi-classical CCC produces 38.96×10^{-17} cm^2 against Winter's tabulated value of 39.42 $\times10^{-17}$ cm^2. Moreover, in this case our results are in good accord with those from the 36 state triple centre calculations of Winter and Lin [94]. For instance, at E=15 keV the discrepancy is only around 6%. Also shown in Figure 6.9 are the experimental results reported by Bayfield [206] and McClure [211]. The estimated accuracy of McClure's data is 5%. Whereas the results of Bayfield have larger inaccuracy. The error is 15% at E <10 keV and 10% for E >10 keV. Also shown are the experimental data of Wittkower [212]

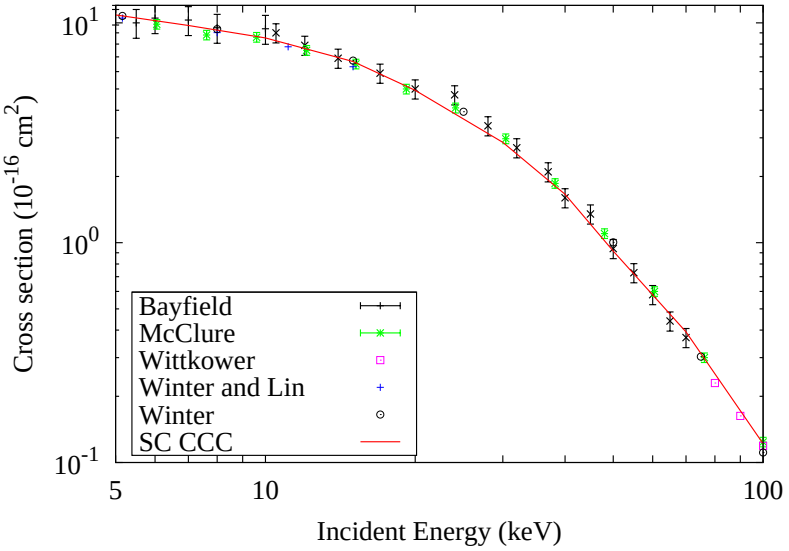

Figure 6.9: The total electron-capture cross section for the p-H($1s$) collisions. Experimental results are due to Bayfield *et al.* [206], McClure *et al.* [211] and Wittkower *et al.* [212]. The experimental data of Wittkower *et al.* [212] are given without error bars. The theoretical results are by Winter and Lin [94] and Winter [90].

obtained by furnace target technique. These data are shown at higher energies without error bars, as reported [212]. There is excellent agreement between our theoretical results and these experimental values.

6.4.4 Total ionisation cross sections

As discussed earlier, asymmetric calculations with systematically increasing $l_{\max}$ and $n_{\max}$ have been performed. And good convergence at fixed value of the maximal orbital angular momentum with respect to $n_{\max}$ is reached (see Figure 6.1). Pseudostates with $l_{\max} = 5$ have been included in the calculations, but no convergence with respect to the orbital angular momentum has been observed. The results from the current asymmetric CCC calculations are shown in Figure 6.10 in comparison with the experimental cross sections of Shah *et al.* [104, 105, 213]. Also shown are the results of Sidky and Lin [203] obtained by the two-centre

momentum-space discretization method and those by Toshima [89]. The corresponding solid curves are obtained by cubic spline interpolation of the reported results. As it is seen from Figure 6.10 the TICS is markedly larger than those by Toshima and Sidky and Lin. At the ionisation peak (E =50 keV) our TICS is about 7% larger than the corresponding value of Toshima [89]. This is also clearly seen from Figure 6.11, where the total ionisation probability is compared with that by Toshima [89].

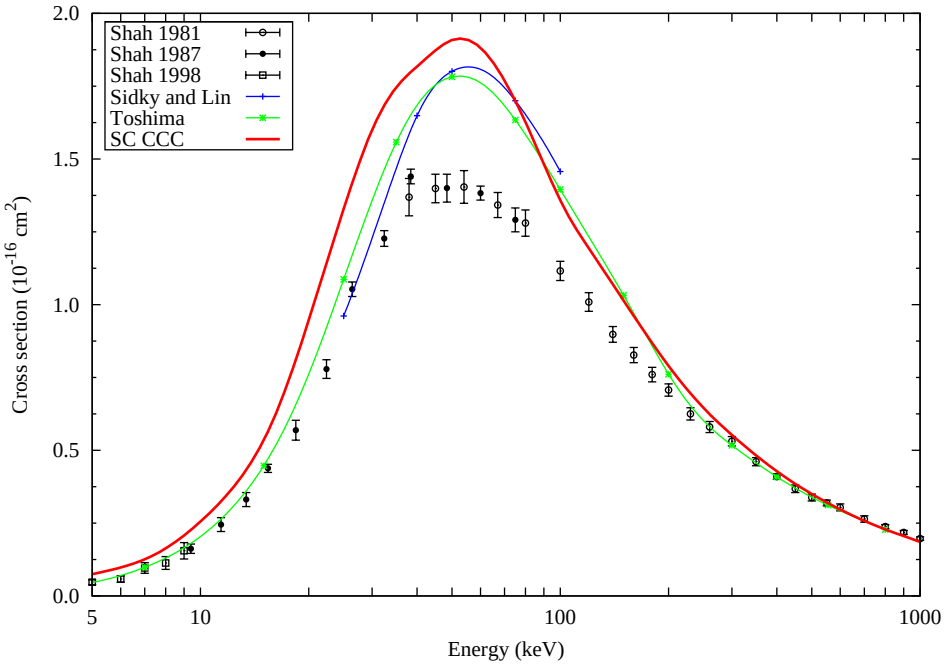

Figure 6.10: The total ionisation cross section for the p-H($1s$) collisions. Experimental results are by Shah *et al.* [104, 105, 213]. Theoretical calculations are by Sidky and Lin [203] and Toshima [89].

In addition to the asymmetric calculations discussed above, a limited number of full two-centre calculations have also been performed. Here we give the results of the symmetric calculations including s and p states. In Figure 6.12 we plot the TICS from the symmetric calculations. For comparison, unpublished results from the fully quantum-mechanical approach (which is being developed at the moment in our group) are also shown. Semi-classical cross sections are

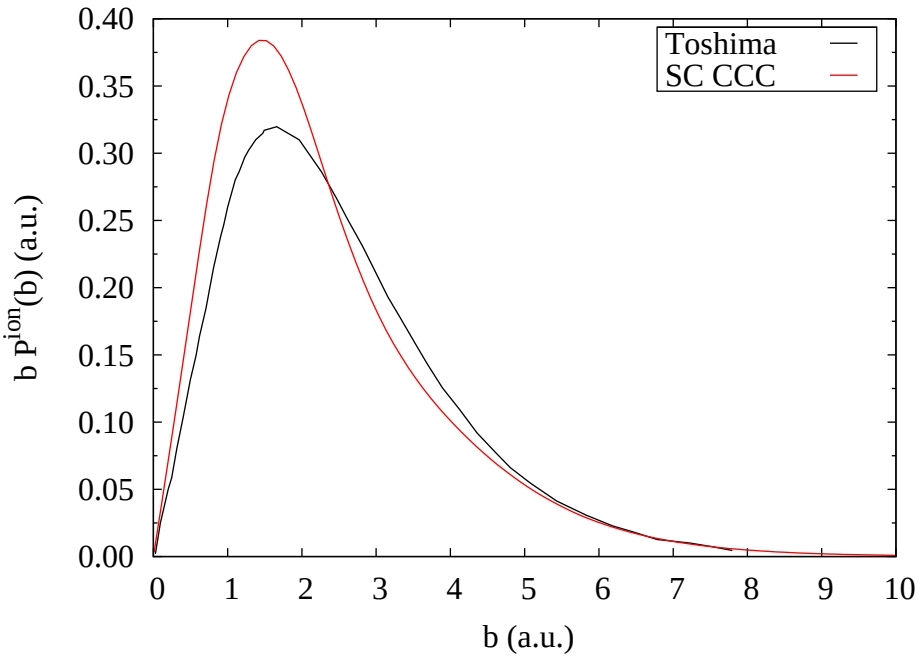

Figure 6.11: Weighted total ionisation probability as a function of the impact-parameter at a collision energy of 50 keV. For comparison the digitalised data of Toshima [89] is also given.

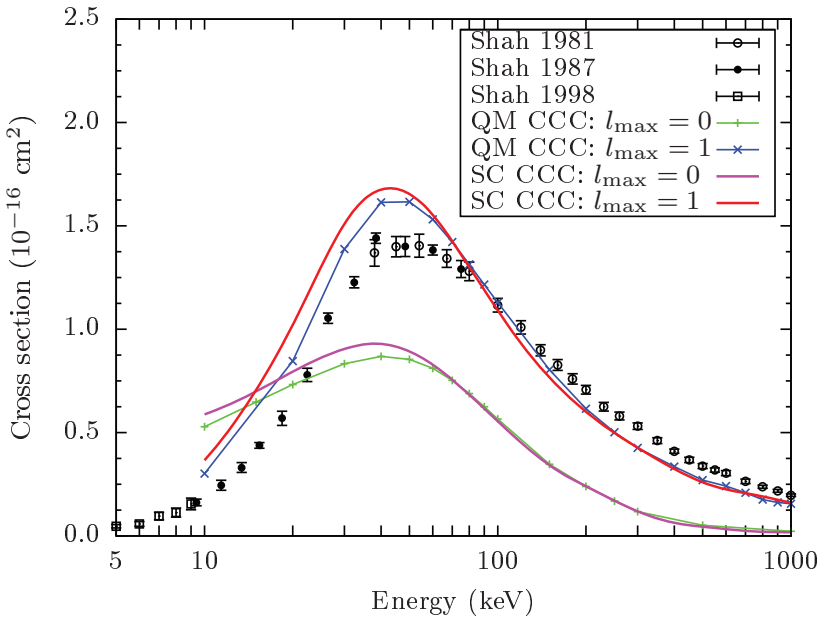

Figure 6.12: The total ionisation cross section for the p-H($1s$) collisions from the symmetric calculations. QM CCC denotes fully quantum-mechanical method.

systematically larger than the corresponding quantum-mechanical ones at lower impact energies. At higher energies the results from the two methods merge.

6.5 Chapter summary

Summarising, in this Chapter the semi-classical close-coupling method, described in detail in Chapter 5, has been applied to the benchmark collision system p+H($1s$). We have started with the verification of the proposed numerical technique for the calculation of the charge exchange matrix elements. Comparison of the effective potentials computed by this technique with those from Avakov *et al.* [198] justifies that the approach works well. Further Born and few eigenstate calculations support this statement.

An asymmetric type of calculations with a large number of Laguerre-based pseudostates have been performed. Good agreement with available experiments and various theoretical calculations is obtained for the $2s$, $2p$ excitation and electron capture as well as the total capture cross sections.

However, there are issues with the reported calculations. The first, probably the most serious, one is related to the convergence of the total ionisation cross sections with respect to the angular momentum. Calculations with $l_{\max} = 5$ have been performed, but no convergence has been reached.

In addition to the asymmetric two-centre expansion calculations, the results from the fully symmetric ones including pseudostates with $l_{\max} = 1$ have been given. These calculations are more difficult. Some numerical instabilities in this type of calculations are known [50, 88]. Also, it is known that it is possible to overcome these instabilities by improving the accuracy of the matrix elements. For example, we can state (without going into details) that at least 12 digit

accuracy has been reached working in double precision arithmetic. This accuracy is increased to at least 16 digits if quadruple precision arithmetic is used. Nevertheless, severe numerical instabilities (in the semi-classical approach) encountered at low energies and very small impact parameters, prevented from getting fully convergent results. For the moment the sources of these issues are unknown. Further studies are needed to clarify the origin of these issues.

Chapter 7

Conclusions

This thesis was devoted to theoretical investigation of ion-atom collisions. Based on the state of the art theoretical developments for antiproton and proton collisions with atomic and molecular systems, as well as inspired by wide-range applications, five goals were specified:

(i) Implementation of the single-centre convergent close-coupling (CCC) method.

(ii) Extension of the method to treat the collisions of antiproton with multi-electron targets.

(iii) Generalisation of the CCC approach to deal with molecular targets.

(iv) Extension of the CCC method to two-centre problems.

(v) Testing the two-centre method on the $p-\mathrm{H}(1s)$ system including electron transfer.

We have developed a new method based on the semi-classical impact-parameter formalism, where the projectile moves along a straight-line trajectory. The electrons of the target are treated fully quantum-mechanically. For the expansion of the total wave function we follow the quantum-mechanical CCC method, which has been quite successful in studying collisions of electrons and positrons with

atoms and molecules. The idea of the CCC formalism is to expand the total scattering wave function in a large orthogonal set of Laguerre-based functions. The increase of the basis size leads to the convergence of all possible cross sections. The developed method has been tested using the $\bar{p}$-H($1s$) system by calculating excitation as well as ionisation cross sections and comparing them with previously reported fully quantum mechanical and semi-classical calculations.

The single-centre CCC approach has been applied to investigate the single-ionisation of Ne, Ar, Kr and Xe by antiproton impact. The wave functions of Ne, Ar, Kr and Xe atoms have been described using a model of six p-shell electrons above an inert Hartree-Fock core with only one-electron excitations from the outer p shell allowed. Single-ionisation cross sections for Ne, Ar, Kr and Xe have been calculated in the energy interval from 5 keV to 2 MeV. It is found that as the target atoms get more complex, the inclusion of states with higher orbital angular momentum is necessary to obtain converged results. Ionisation energies, calculated within the frozen-core approximation, are found to be in reasonably good agreement with experimentally observed values. This also shows the accuracy of the used structure model. Calculated single-ionisation cross sections for Ne, Ar, Kr and Xe are in good accord with the experimental measurements. However, the comparison revealed a common feature of the CCC cross sections for the noble gas targets. That is the method underestimates the experimental data below 100 keV and slightly overestimates above this energy. Since frozen-core approximation is used for the target structure calculation this feature is not unexpected.

The time-dependent CCC approach has been generalised to treat antiproton collisions with molecular targets. This involves a particularly useful development which allows analytic averaging over all molecular orientations. The interaction matrix elements and time-dependent expansion coefficients are expressed in such

a way that the molecular orientation dependence is separated. This allows to derive a new set of scattering equations that are independent of the molecular orientation.

Being valid at all collision energies, the approach significantly improves the agreement between theory and experiment for $\bar{p}-H_2$ single ionisation cross sections. It has been shown that the strong suppression of the single ionisation cross section at low energies is due to the structure of the molecular target. Based on the studies of the time evolution of the electron cloud distribution during the antiproton collisions with atomic and molecular hydrogen, it is shown that the electron, which would have gone into the continuum in the atomic hydrogen case, gets captured by one of the target protons in the molecular hydrogen case. In order to have a complete picture of the full target breakup, the cross sections for ionisation with excitation, double ionisation and proton production in antiproton-molecular hydrogen collisions have been calculated employing a sequential two-step approximation. Reasonably good agreement with experiment for proton production was found above 40 keV.

The approach developed for multi-electron targets has been applied to treat antiproton scattering on H_2O. The water molecule was modelled as dressed atoms in a pseudo-spherical potential. It is worthwhile to mention that previous theoretical calculations are based on Born and continuum-distorted-wave approximations. Therefore, we believe that the close-coupling approach to $\bar{p}-H_2O$ provides more reliable results at the intermediate collision energies.

The time-dependent single-centre CCC method has been extended to the two-centre case. There are two distinctive features in this formulation. The first one is related to the plane-wave electron translational factors (PWETF). In the standard semi-classical close-coupling methods it is common to start with

the time-dependent Schrödinger equation, where the electronic wave function is expanded in terms of target and projectile centred atomic orbitals augmented with the relevant PWETF. These factors were introduced by Bates [68, 69]. In contrast to that scheme, we have started with the full Schrödinger equation, and the total wave function is expanded as combinations of the asymptotic scattering functions. Inserting this expansion into the Schrödinger equation, we have obtained the coupled channel equations for the expansion coefficients. In this formulation PWETF appear in the exchange matrix elements in systematic and mathematically rigorous way.

Apart from the fundamental significance discussed above, a different numerical technique for evaluating exchange matrix elements was given. In this technique the matrix elements are expressed in such a way that the angular and radial parts are separated. This allows to save the radial parts as a function of the internuclear distance, R. While solving the system of coupled equations the required values of the matrix elements are found by interpolation. This result can be considered as an advantage over the most commonly used way of evaluating exchange matrix elements in the prolate spheroidal coordinates in which the impact parameter (b) and the integration variable (Z) are not separable, and it is necessary to evaluate a two-dimensional integral on a (b, Z) grid. From the first glance, evaluation of the two-centre matrix elements according to this technique may seem to require large memory resources. However, with effective coding strategies, this is not a major problem. Detailed comparison of the effective potentials with those from Avakov *et al.* [198] demonstrated that the method works well. Furthermore, performed Born and eigenstate calculations also confirm this conclusion.

As a first essential testing step of the two-centre method asymmetric calculations with large number of Laguerre pseudostates have been performed.

Excitation and electron capture to $2s$ and $2p$ states as well as the total capture cross sections are found to be in good accord with available experiments. As far as the comparison with theoretical calculations is concerned, the agreement is remarkably good with the latest calculations of Winter [90].

Limited number of symmetric two-centre calculations including pseudostates with $l_{\max} = 1$ have also been performed. These calculations are more difficult. The existence of numerical instabilities in this type of calculations has been reported by Kuang and Lin [50] and Toshima [88]. These numerical difficulties have been observed in our symmetric calculations. In order to overcome them we had to do the calculations in quadruple-precision arithmetic. The results from the symmetric calculations have been compared with the corresponding ones from the fully quantum-mechanical approach. This comparison shows that the semi-classical results are slightly larger than the quantum-mechanical ones.

A number of directions can be specified for future investigations. Firstly, it would be interesting to investigate multiple ionisation processes of noble gas atoms by antiproton impact using the method outlined in Chapter 3. This application represents a much stricter test for the theory enabling better understanding of the role of electron correlations in the collision. Secondly, considering the numerical difficulties and the convergence issues in the two- centre calculations, it is desirable to establish the sources of these problems and resolve them. Are these issues of only numerical origin? Or may there be some physics hidden behind them and the formulation needs to be revisited? These open questions serve as motivation for further studies.

List of Figures

List of Tables

Bibliography

[1] *Facility for Antiproton and Ion Research*, www.gsi.de/FAIR.

[2] *Low-energy antiproton and ion research*, www.oeaw.ac.at/smi/FLAIR.

[3] https://espace.cern.ch/elena-project/sitepages/home.aspx.

[4] *ALPHA experiment*, http://alpha.web.cern.ch/.

[5] D. Belkić, *Theory of Heavy Ion Collision Physics in Hadron Therapy* (Elsevier, Amsterdam, 2013).

[6] D. Kramer, Physics Today **68**, 24 (2015).

[7] *Particle Therapy Statistics in 2013*, http://theijpt.org/doi/pdf/10.14338/IJPT.14-editorial-2.1.

[8] T. Kirchner and H. Knudsen, J. Phys. B **44**, 122001 (2011).

[9] M. Hori and J. Walz, Progress in Particle and Nuclear Physics **72**, 206 (2013).

[10] http://www.flairatfair.eu/typo3/physics.html.

[11] http://users-phys.au.dk/hknudsen/introduction.html.

[12] M. R. C. McDowell and J. P. Coleman, *Introduction to the theory of ion-atom collisions* (North-Holland, Amsterdam, 1970).

[13] B. H. Bransden and M. R. C. McDowell, *Charge exchange and the Theory of Ion-atom Collisions* (Clarendon, Oxford, 1992).

[14] R. Abrines and I. C. Percival, Proc. Phys. Soc. (London) **88**, 873 (1966).

[15] R. E. Olson and A. Salop, Phys. Rev. A **16**, 531 (1977).

[16] D. R. Schultz, Phys. Rev. A **40**, 2330 (1989).

[17] G. B. Crooks and M. E. Rudd, Phys. Rev. Lett. **25**, 1599 (1970).

[18] C. Illescas, B. Pons, and A. Riera, Phys. Rev. A **65**, 030703 (2002).

[19] M. B. Shah, C. McGrath, C. Illescas, B. Pons, A. Riera, H. Luna, D. S. F. Crothers, S. F. C. O'Rourke, and H. B. Gilbody, Phys. Rev. A **67**, 010704 (2003).

[20] L. Sarkadi and R. O. Barrachina, Phys. Rev. A **71**, 062712 (2005).

[21] N. D. Cariatore and S. Otranto, Phys. Rev. A **88**, 012714 (2013).

[22] N. D. Cariatore, S. Otranto, and R. E. Olson, Phys. Rev. A **91**, 042709 (2015).

[23] D. S. F. Crothers and J. F. McCann, J. Phys. B **16**, 3229 (1983).

[24] P. D. Fainstein, L. Gulyas, and A. Salin, J. Phys. B **27**, L259 (1994).

[25] L. Gulyas, P. D. Fainstein, and A. Salin, J. Phys. B **28**, 245 (1995).

[26] R. Moshammer, J. Ullrich, M. Unverzagt, W. Schmidt, P. Jardin, R. E. Olson, R. Mann, R. Dörner, V. Mergel, U. Buck, et al., Phys. Rev. Lett. **73**, 3371 (1994).

[27] J. Ullrich, R. Moshammer, A. Dorn, R. Drner, L. P. H. Schmidt, and H. Schmidt-Bcking, Rep. Prog. Phys. **66**, 1463 (2003).

[28] R. Drner, V. Mergel, O. Jagutzki, L. Spielberger, J. Ullrich, R. Moshammer, and H. Schmidt-Bcking, Phys. Rep. **330**, 95 (2000).

[29] P. D. Fainstein, V. H. Ponce, and R. D. Rivarola, J. Phys. B **24**, 3091 (1991).

[30] V. D. Rodríguez and R. O. Barrachina, Phys. Rev. A **57**, 215 (1998).

[31] M. D. Sanchez, W. R. Cravero, and C. R. Garibotti, Phys. Rev. A **61**, 062709 (2000).

[32] A. B. Voitkiv and J. Ullrich, Phys. Rev. A **67**, 062703 (2003).

[33] A. B. Voitkiv, B. Najjari, and J. Ullrich, J. Phys. B **36**, 2591 (2003).

[34] A. B. Voitkiv, B. Najjari, R. Moshammer, M. Schulz, and J. Ullrich, J. Phys. B **37**, L365 (2004).

[35] A. B. Voitkiv and B. Najjari, Phys. Rev. A **79**, 022709 (2009).

[36] M. F. Ciappina and L. B. Madsen, J. Phys. B **39**, 5037 (2006).

[37] D. Fischer, A. B. Voitkiv, R. Moshammer, and J. Ullrich, Phys. Rev. A **68**, 032709 (2003).

[38] K. A. Kouzakov, S. A. Zaytsev, Y. V. Popov, and M. Takahashi, Phys. Rev. A **86**, 032710 (2012).

[39] M. F. Ciappina, T.-G. Lee, M. S. Pindzola, and J. Colgan, Phys. Rev. A **88**, 042714 (2013).

[40] U. Chowdhury, M. Schulz, and D. H. Madison, Phys. Rev. A **83**, 032712 (2011).

[41] D. H. Madison, D. Fischer, M. Foster, M. Schulz, R. Moshammer, S. Jones, and J. Ullrich, Phys. Rev. Lett. **91**, 253201 (2003).

[42] L. Gulyás, S. Egri, and T. Kirchner, Phys. Rev. A **90**, 062710 (2014).

[43] R. Hubele, A. LaForge, M. Schulz, J. Goullon, X. Wang, B. Najjari, N. Ferreira, M. Grieser, V. L. B. de Jesus, R. Moshammer, et al., Phys. Rev. Lett. **110**, 133201 (2013).

[44] M. E. Galassi, C. Champion, P. F. Weck, R. D. Rivarola, O. Fojn, and J. Hanssen, Physics in Medicine and Biology **57**, 2081 (2012).

[45] J. C. Wells, D. R. Schultz, P. Gavras, and M. S. Pindzola, Phys. Rev. A **54**, 593 (1996).

[46] D. R. Schultz, J. C. Wells, P. S. Krstić, and C. O. Reinhold, Phys. Rev. A **56**, 3710 (1997).

[47] A. Kołakowska, M. S. Pindzola, F. Robicheaux, D. R. Schultz, and J. C. Wells, Phys. Rev. A **58**, 2872 (1998).

[48] K.-H. Schartner, D. Detleffsen, and B. Sommer, Phys. Lett. A **136**, 55 (1989).

[49] D. P. Higgins, J. Geddes, and H. B. Gilbody, J. Phys. B **29**, 1219 (1996).

[50] J. Kuang and C. D. Lin, J. Phys. B **29**, 1207 (1996).

[51] D. Belki, R. Gayet, and A. Salin, Atomic Data and Nuclear Data Tables **51**, 59 (1992).

[52] D. R. Schultz, M. R. Strayer, and J. C. Wells, Phys. Rev. Lett. **82**, 3976 (1999).

[53] M. S. Pindzola, T. G. Lee, T. Minami, and D. R. Schultz, Phys. Rev. A **72**, 062703 (2005).

[54] M. S. Pindzola and D. R. Schultz, Phys. Rev. A **77**, 014701 (2008).

[55] E. Y. Sidky and C. D. Lin, J. Phys. B **31**, 2949 (1998).

[56] W. Fritsch and C. Lin, Phys. Rep. **202**, 1 (1991).

[57] M. Kimura and N. F. Lane, Adv. At., Mol., Opt. Phys. **26**, 79 (1989).

[58] S. Ovchinnikov, G. Ogurtsov, J. Macek, and Y. Gordeev, Phys. Rep. **389**, 119 (2004).

[59] T. G. Lee, H. C. Tseng, and C. D. Lin, Phys. Rev. A **61**, 062713 (2000).

[60] M. McGovern, D. Assafrão, J. R. Mohallem, C. T. Whelan, and H. R. J. Walters, Phys. Rev. A **79**, 042707 (2009).

[61] M. McGovern, D. Assafrão, J. R. Mohallem, C. T. Whelan, and H. R. J. Walters, Phys. Rev. A **81**, 032708 (2010).

[62] A. Lühr and A. Saenz, Phys. Rev. A **77**, 052713 (2008).

[63] M. S. Pindzola, T. G. Lee, and J. Colgan, J. Phys. B **44**, 205204 (2011).

[64] A. Lühr and A. Saenz, Phys. Rev. A **78**, 032708 (2008).

[65] A. Lühr and A. Saenz, Phys. Rev. A **80**, 022705 (2009).

[66] A. Lühr and A. Saenz, Phys. Rev. A **81**, 010701 (2010).

[67] A. L. Ford, J. F. Reading, and K. A. Hall, J. Phys. B **26**, 4537 (1993).

[68] D. R. Bates and R. McCarroll, Proc. R. Soc. A **245**, 175 (1958).

[69] D. R. Bates, Proc. R. Soc. A **247**, 294 (1958).

[70] R. McCarroll, Proc. R. Soc. A **264**, 547 (1961).

[71] L. Wilets and D. F. Gallaher, Phys. Rev. **147**, 13 (1966).

[72] I. M. Cheshire, D. F. Gallaher, and A. J. Taylor, J. Phys. B **3**, 813 (1970).

[73] D. Rapp, D. Dinwiddie, D. Storm, and T. E. Sharp, Phys. Rev. A **5**, 1290 (1972).

[74] I. M. Cheshire, Proc. Phys. Soc. (London) **92**, 862 (1967).

[75] J. Fennema, Physica **44**, 90 (1969).

[76] D. Rapp and D. Dinwiddie, J. Chem. Phys. **57**, 4919 (1972).

[77] D. F. Gallaher and L. Wilets, Phys. Rev. **169**, 139 (1968).

[78] R. Shakeshaft, Phys. Rev. A **18**, 1930 (1978).

[79] H. F. Helbig and E. Everhart, Phys. Rev. **140**, A715 (1965).

[80] R. Shakeshaft, J. Macek, and E. Gerjuoy, J. Phys. B **6**, 794 (1973).

[81] R. Shakeshaft, J. Phys. B **8**, 1114 (1975).

[82] R. Shakeshaft, Phys. Rev. A **14**, 1626 (1976).

[83] H. A. Slim and A. M. Ermolaev, J. Phys. B **27**, L203 (1994).

[84] J. T. Park, J. E. Aldag, J. M. George, and J. L. Peacher, Phys. Rev. A **14**, 608 (1976).

[85] D. Detleffsen, M. Anton, A. Werner, and K. H. Schartner, J. Phys. B **27**, 4195 (1994).

[86] A. Werner and K.-H. Schartner, J. Phys. B **29**, 125 (1996).

[87] N. Toshima, J. Phys. B **25**, L635 (1992).

[88] N. Toshima, J. Phys. B **30**, L131 (1997).

[89] N. Toshima, Phys. Rev. A **59**, 1981 (1999).

[90] T. G. Winter, Phys. Rev. A **80**, 032701 (2009).

[91] D. G. M. Anderson, M. J. Antal, and M. B. McElroy, J. Phys. B **7**, L118 (1974).

[92] M. J. Antal, M. B. McElroy, and D. G. M. Anderson, J. Phys. B **8**, 1513 (1975).

[93] C. D. Lin, T. G. Winter, and W. Fritsch, Phys. Rev. A **25**, 2395 (1982).

[94] T. G. Winter and C. D. Lin, Phys. Rev. A **29**, 567 (1984).

[95] T. G. Winter and C. D. Lin, Phys. Rev. A **29**, 3071 (1984).

[96] B. M. McLaughlin, T. G. Winter, and J. F. McCann, J. Phys. B **30**, 1043 (1997).

[97] T. G. Winter, Phys. Rev. A **37**, 4656 (1988).

[98] O. J. Kroneisen, H. J. Ldde, T. Kirchner, and R. M. Dreizler, Journal of Physics A: Mathematical and General **32**, 2141 (1999).

[99] T. Kirchner, H. Ldde, O. Kroneisen, and R. Dreizler, Nucl. Instr. and Meth. B **154**, 46 (1999).

[100] B. H. Bransden, *Atomic collision theory*, Lecture notes and supplements in physics (Benjamin/Cummings, Reading, Massachusetts, 1983), 2nd ed.

[101] Y. N. Demkov, *Variational Principles in the Theory of Collisions* (Pergamon, Oxford, 1963).

[102] M. Zapukhlyak, T. Kirchner, H. J. Ldde, S. Knoop, R. Morgenstern, and R. Hoekstra, J. Phys. B **38**, 2353 (2005).

[103] H. J. Lüdde, T. Spranger, M. Horbatsch, and T. Kirchner, Phys. Rev. A **80**, 060702 (2009).

[104] M. B. Shah, D. S. Elliott, and H. B. Gilbody, J. Phys. B **20**, 2481 (1987).

[105] M. B. Shah, J. Geddes, B. M. McLaughlin, and H. B. Gilbody, J. Phys. B **31**, L757 (1998).

[106] I. Bray and A. T. Stelbovics, Phys. Rev. A **46**, 6995 (1992).

[107] I. Bray and D. V. Fursa, J. Phys. B **44**, 061001 (2011).

[108] X. Ren, I. Bray, D. Fursa, J. Colgan, M. Pindzola, T. Pflüger, A. Senftleben, S. Xu, A. Dorn, and J. Ullrich, Phys. Rev. A **83**, 052711 (2011).

[109] M. C. Zammit, D. V. Fursa, and I. Bray, Phys. Rev. A **82**, 052705 (2010).

[110] K. Bartschat, A. S. Kheifets, D. V. Fursa, and I. Bray, J. Phys. B **43**, 165205 (2010).

[111] I. Bray, D. V. Fursa, A. S. Kadyrov, and A. T. Stelbovics, Phys. Rev. A **81**, 062704 (2010).

[112] C. J. Bostock, M. J. Berrington, D. V. Fursa, and I. Bray, Phys. Rev. Lett. **107**, 093202 (2011).

[113] A. V. Lugovskoy, A. S. Kadyrov, I. Bray, and A. T. Stelbovics, Phys. Rev. A **82**, 062708 (2010).

[114] R. Utamuratov, A. S. Kadyrov, D. V. Fursa, I. Bray, and A. T. Stelbovics, Phys. Rev. A **82**, 042705 (2010).

[115] R. Utamuratov, A. S. Kadyrov, D. V. Fursa, I. Bray, and A. T. Stelbovics, J. Phys. B **43**, 125203 (2010).

[116] J. S. Savage, D. V. Fursa, and I. Bray, Phys. Rev. A **83**, 062709 (2011).

[117] A. S. Kadyrov, I. B. Abdurakhmanov, R. Utamuratov, A. V. Lugovskoy, D. V. Fursa, I. Bray, and A. T. Stelbovics, J. Phys.: Conf. Series **262**, 012028 (2011).

[118] A. C. L. Jones, C. Makochekanwa, P. Caradonna, D. S. Slaughter, J. R. Machacek, R. P. McEachran, J. P. Sullivan, S. J. Buckman, A. D. Stauffer, I. Bray, et al., Phys. Rev. A **83**, 032701 (2011).

[119] I. B. Abdurakhmanov, A. S. Kadyrov, I. Bray, and A. T. Stelbovics, J. Phys. B **44**, 075204 (2011).

[120] I. B. Abdurakhmanov, A. S. Kadyrov, I. Bray, and A. T. Stelbovics, J. Phys. B **44**, 165203 (2011).

[121] K. A. Hall, J. F. Reading, and A. L. Ford, J. Phys. B **29**, 6123 (1996).

[122] A. Igarashi, S. Nakazaki, and A. Ohsaki, Phys. Rev. A **61**, 062712 (2000).

[123] N. Toshima, Phys. Rev. A **64**, 024701 (2001).

[124] T. G. Winter, Phys. Rev. A **83**, 022709 (2011).

[125] S. Sahoo, S. C. Mukherjee, and H. R. J. Walters, J. Phys. B **37**, 3227 (2004).

[126] A. Lühr and A. Saenz, Phys. Rev. A **80**, 022705 (2009).

[127] D. R. Bates, Proc. Roy. Soc. A **247**, 294 (1958).

[128] M. H. Mittleman, Phys. Rev. **122**, 499 (1961).

[129] L. Wilets and S. J. Wallace, Phys. Rev. **169**, 84 (1968).

[130] R. McCarroll and A. Salin, J. Phys. B **1**, 163 (1968).

[131] M. McGovern, D. Assafrão, J. R. Mohallem, C. T. Whelan, and H. R. J. Walters, Phys. Rev. A **79**, 042707 (2009).

[132] M. McGovern, D. Assafrão, J. R. Mohallem, C. T. Whelan, and H. R. J. Walters, Phys. Rev. A **81**, 032708 (2010).

[133] I. Bray and A. T. Stelbovics, Phys. Rev. A **46**, 6995 (1992).

[134] A. S. Kadyrov and I. Bray, Phys. Rev. A **66**, 012710 (2002).

[135] R. Utamuratov, A. S. Kadyrov, D. V. Fursa, and I. Bray, J. Phys. B **43**, 031001 (2010).

[136] I. B. Abdurakhmanov, A. S. Kadyrov, D. V. Fursa, I. Bray, and A. T. Stelbovics, Phys. Rev. A **84**, 062708 (2011).

[137] D. A. Varshalovich, A. N. Moskalev, and V. K. Khersonskii, *Quantum theory of angular momentum* (World Scientific Pub., Philadelphia, 1988), 1st ed.

[138] H. Knudsen, U. Mikkelsen, K. Paludan, K. Kirsebom, S. P. Møller, E. Uggerhøj, J. Slevin, M. Charlton, and E. Morenzoni, Phys. Rev. Lett. **74**, 4627 (1995).

[139] D. R. Bates and G. W. Griffing, Proc. Phys. Soc. (London) **67**, 663 (1954).

[140] L. H. Andersen, P. Hvelplund, H. Knudsen, S. P. Moller, A. H. Sorensen, K. Elsener, K.-G. Rensfelt, and E. Uggerhoj, Phys. Rev. A **36**, 3612 (1987).

[141] K. Paludan, H. Bluhme, H. Knudsen, U. Mikkelsen, S. P. Mller, E. Uggerhj, and E. Morenzoni, J. Phys. B **30**, 3951 (1997).

[142] H. Knudsen, H.-P. E. Kristiansen, H. D. Thomsen, U. I. Uggerhøj, T. Ichioka, S. P. Møller, C. A. Hunniford, R. W. McCullough, M. Charlton, N. Kuroda, et al., Phys. Rev. Lett. **101**, 043201 (2008).

[143] *The Antiproton Decelerator*, home.web.cern.ch/about/accelerators/antiproton-decelerator.

[144] T. Kirchner, H. J. Lüdde, and R. M. Dreizler, Phys. Rev. A **61**, 012705 (1999).

[145] T. Kirchner, M. Horbatsch, and H. J. Lüdde, Phys. Rev. A **66**, 052719 (2002).

[146] C. Montanari and J. Miraglia, J. Phys. B **45**, 105201 (2012).

[147] D. Fursa and I. Bray, New J. Phys. **14**, 035002 (2012).

[148] D. V. Fursa and I. Bray, Phys. Rev. A **52**, 1279 (1995).

[149] The ALPHA Collaboration, Nature **483**, 439 (2012).

[150] The ALPHA Collaboration and A. E. Charman, Nature Communications **4**, 1785 (2013).

[151] Nuclear Instruments and Methods in Physics Research Section B: Beam Interactions with Materials and Atoms **266**, 351 (2008).

[152] P. Debu for the GBAR Collaboration, Hyperfine Interactions **212**, 51 (2012).

[153] N. Bassler, J. Alsner, G. Beyer, J. J. DeMarco, M. Doser, D. Hajdukovic, O. Hartley, K. S. Iwamoto, O. Jkel, H. V. Knudsen, et al., Radiotherapy and Oncology **86**, 14 (2008).

[154] A. Guyton, *Textbook of Medical Physiology* (W.B. Saunders, Philadelphia, 1976), 5th ed.

[155] H. Knudsen, H. A. Torii, M. Charlton, Y. Enomoto, I. Georgescu, C. A. Hunniford, C. H. Kim, Y. Kanai, H.-P. E. Kristiansen, N. Kuroda, et al., Phys. Rev. Lett. **105**, 213201 (2010).

[156] L. H. Andersen, P. Hvelplund, H. Knudsen, S. P. Moller, J. O. P. Pedersen, S. Tang-Petersen, E. Uggerhoj, K. Elsener, and E. Morenzoni, J. Phys. B **23**, L395 (1990).

[157] P. Hvelplund, H. Knudsen, U. Mikkelsen, E. Morenzoni, S. P. Moller, E. Uggerhoj, and T. Worm, J. Phys. B **27**, 925 (1994).

[158] D. R. Schultz, P. S. Krstic, C. O. Reinhold, and J. C. Wells, Phys. Rev. Lett. **76**, 2882 (1996).

[159] X. Guan and K. Bartschat, Phys. Rev. Lett. **103**, 213201 (2009).

[160] A. Ermolaev, Hyperfine Interactions **76**, 335 (1993).

[161] A. Lühr and A. Saenz, Phys. Rev. A **78**, 032708 (2008).

[162] A. Lühr and A. Saenz, Phys. Rev. A **81**, 010701 (2010).

[163] M. S. Pindzola, T.-G. Lee, and J. Colgan, J. Phys. B **43**, 235201 (2010).

[164] T. G. Lee, M. S. Pindzola, and J. Colgan, J. Phys. B **45**, 045203 (2012).

[165] B. Senger, E. Wittendorp-Rechenmann, and R. V. Rechenmann, Nuclear Instruments and Methods in Physics Research **194**, 437 (1982).

[166] B. Senger and R. V. Rechenmann, Nucl. Instr. and Meth. B **2**, 204 (1984).

[167] C. E. Kuyatt and T. Jorgensen, Phys. Rev. **130**, 1444 (1963).

[168] G. S. Khandelwal and E. Merzbacher, Phys. Rev. **151**, 12 (1966).

[169] G. S. Khandelwal and E. Merzbacher, Phys. Rev. **144**, 349 (1966).

[170] B.-H. Choi, E. Merzbacher, and G. Khandelwal, Atomic Data and Nuclear Data Tables **5**, 291 (1973).

[171] A. Salin, J. Phys. B **2**, 631 (1969).

[172] G. H. Olivera, P. D. Fainstein, and R. D. Rivarola, Physics in Medicine and Biology **41**, 1633 (1996).

[173] O. Boudrioua, C. Champion, C. Dal Cappello, and Y. V. Popov, Phys. Rev. A **75**, 022720 (2007).

[174] R. Moccia, J. Chem. Phys. **40**, 2186 (1964).

[175] C. C. Montanari and J. E. Miraglia, J. Phys. B **47**, 015201 (2014).

[176] A. Lühr and A. Saenz, Phys. Rev. A **78**, 032708 (2008).

[177] W. Demtröder, *Atoms, Molecules and Photons: An Introduction to Atomic-, Molecular- and Quantum Physics*, Graduate Texts in Physics (Springer, 2010).

[178] K. Sakimoto, Phys. Rev. A **71**, 062704 (2005).

[179] A. Lühr and A. Saenz, Phys. Rev. A **80**, 022705 (2009).

[180] M. C. Zammit, D. V. Fursa, and I. Bray, Phys. Rev. A **87**, 020701 (2013).

[181] D. Wünderlich and U. Fantz, Atomic Data and Nuclear Data Tables **97**, 152 (2011).

[182] G. Hunter, A. W. Yau, and H. O. Pritchard, Atomic Data and Nuclear Data Tables **14**, 11 (1974).

[183] P. Hvelplund, H. Knudsen, U. Mikkelsen, E. Morenzoni, S. P. Møller, E. Uggerhøj, and T. Worm, Journal of Physics B: Atomic, Molecular and Optical Physics **27**, 925 (1994).

[184] L. A. Wehrman, A. L. Ford, and J. F. Reading, J. Phys. B **29**, 5831 (1996).

[185] L. A. Wehrman, A. L. Ford, and J. F. Reading, J. Phys. B **29**, 5831 (1996).

[186] T. E. Sharp, Atomic Data and Nuclear Data Tables **2**, 119 (1970).

[187] I. B. Abdurakhmanov, A. S. Kadyrov, D. V. Fursa, and I. Bray, Phys. Rev. Lett. **111**, 173201 (2013).

[188] M. Bernal and J. Liendo, Nuclear Instruments and Methods in Physics Research Section B: Beam Interactions with Materials and Atoms **262**, 1 (2007).

[189] C. Champion, M. E. Galassi, P. F. Weck, O. Fojón, J. Hanssen, and R. D. Rivarola, *Radiation Damage in Biomolecular Systems (Biological and Medical Physics, Biomedical Engineering)* (Springer, Berlin, 2012).

[190] M. B. Shah and H. B. Gilbody, J. Phys. B **14**, 2361 (1981).

[191] G. W. Kerby, M. W. Gealy, Y.-Y. Hsu, M. E. Rudd, D. R. Schultz, and C. O. Reinhold, Phys. Rev. A **51**, 2256 (1995).

[192] J. Fu, M. J. Fitzpatrick, J. F. Reading, and R. Gayet, J. Phys. B **34**, 15 (2001).

[193] L. F. Errea, C. Harel, H. Jouini, L. Mendez, B. Pons, and A. Riera, J. Phys. B **27**, 3603 (1994).

[194] T. G. Winter, Phys. Rev. A **25**, 697 (1982).

[195] https://en.wikipedia.org/wiki/Tanh-sinh_quadrature.

[196] A. Ralston, *Mathematical methods for digital computers* (New York: John Wiley and Sons, 1960).

[197] J. Butcher, *Numerical methods for ordinary differential equations* (New York: John Wiley and Sons, 2003).

[198] G. V. Avakov, A. R. Ashurov, L. D. Blokhintsev, A. S. Kadyrov, A. M. Mukhamedzhanov, and M. V. Poletayeva, J. Phys. B **23**, 4151 (1990).

[199] D. Belkić, S. Saini, and H. S. Taylor, Phys. Rev. A **36**, 1601 (1987).

[200] S. E. Lovell and M. B. McElroy, Proc. R. Soc. A **283**, pp. 100 (1965).

[201] T. G. Winter and C. C. Lin, Phys. Rev. A **10**, 2141 (1974).

[202] T. J. Morgan, J. Geddes, and H. B. Gilbody, J. Phys. B **6**, 2118 (1973).

[203] E. Y. Sidky and C. D. Lin, Phys. Rev. A **65**, 012711 (2001).

[204] T. Kondow, R. J. Girnius, Y. P. Chong, and W. L. Fite, Phys. Rev. A **10**, 1167 (1974).

[205] T. G. Winter and C. D. Lin, Phys. Rev. A **29**, 567 (1984).

[206] J. E. Bayfield, Phys. Rev. **185**, 105 (1969).

[207] Y. P. Chong and W. L. Fite, Phys. Rev. A **16**, 933 (1977).

[208] J. Hill, J. Geddes, and H. B. Gilbody, J. Phys. B **12**, L341 (1979).

[209] G. Ryding, A. B. Wittkower, and H. B. Gilbody, Proc. Phys. Soc. (London) **89**, 547 (1966).

[210] R. F. Stebbings, R. A. Young, C. L. Oxley, and H. Ehrhardt, Phys. Rev. **138**, A1312 (1965).

[211] G. W. McClure, Phys. Rev. **148**, 47 (1966).

[212] A. B. Wittkower, G. Ryding, and H. B. Gilbody, Proc. Phys. Soc. (London) **89**, 541 (1966).

[213] M. B. Shah and H. B. Gilbody, J. Phys. B **14**, 2361 (1981).